

**Seismic Attribute Analysis of the Mississippian Chert at the Wellington Field,
south-central Kansas**

by

Copyright 2012

Ayrat Sirazhiev

Specialist degree in Geophysics, Kazan State University (Russia), 2009

Submitted to the graduate degree program in Geology and the Graduate Faculty of the University
of Kansas in partial fulfillment of the requirements for the degree of Master of Science

Chairperson Dr. George Tsoflias

Dr. Ross Black

Dr. W. Lynn Watney

Date Defended: 10/31/2012

The Thesis Committee for Ayrat Sirazhiev certifies
that this is the approved version of the following thesis:

**Seismic Attribute Analysis of the Mississippian Chert at the Wellington Field,
south-central Kansas**

Chairperson Dr. George Tsoflias

Dr. Ross Black

Dr. W. Lynn Watney

Date approved: 10/31/2012

ABSTRACT

Mississippian chert reservoirs, important hydrocarbon resources in North America, are highly heterogeneous, typically below seismic resolution and, therefore, present a challenging task for predicting reservoir properties from seismic data. In this study, I conducted a seismic attribute analysis of the Mississippian chert reservoir at the Wellington Field, south-central Kansas using well and 3D PSTM seismic data. The microporous cherty dolomite reservoir exhibits a characteristic vertical gradational porosity reduction and associated increase in acoustic velocity, known as a ramp-transition velocity function. I investigated possible relationships of the Mississippian reservoir thickness and porosity with post-stack seismic attributes, including inverted acoustic impedance.

The analysis of well-log and seismic data revealed that fault #1 divides the Wellington Field diagonally from the southwestern corner to the northeastern corner. The reservoir in the southeastern part of the field is characterized by a vertical gradational porosity decrease (from 25-30 to 4-6%), variable thickness (6-20 m), lower seismic amplitude and frequency content, locally developed double reflector, and high correlation between seismic amplitude and reservoir thickness conformable with the theoretical amplitude response of a ramp-transition velocity function. Amplitude envelope was used to predict the reservoir thickness in this part of the field. The Mississippian reservoir in the northwestern part of the field has more heterogeneous porosity distribution within the reservoir interval, thins in the north-north-west direction, while no clear relationship was found between reservoir thickness and instantaneous seismic attributes. The model-based inversion and porosity model predicted from inverted impedance supported the well-log and seismic attribute interpretation. The reliability of the predicted porosity model is tested by cross-validation. Resolution limits were determined using wedge modeling as $1/16\lambda$ for

the amplitude envelope attribute and $1/8\lambda$ for the model-based inversion within the Mississippian reservoir characterized by a vertical gradational porosity reduction.

The seismic response of a ramp-transition velocity function, well established in theory, but poorly studied using field seismic data, could benefit the characterization of similar chert as well as clastic and carbonate reservoirs characterized by downward porosity reduction as shown in this study. In addition, it might improve an understanding of depositional and diagenetic histories of such reservoirs.

ACKNOWLEDGMENTS

I would like to express my gratitude to all the people who have been around me during these 2 years of completing MS program at the University of Kansas. First of all, I would like to thank ExxonMobil and the Institute of International Education (IIE) for selecting me as a recipient of the ExxonMobil Russian Scholarship and sponsoring my MS program in Geology at the University of Kansas. I am grateful to Enam Haddad, my scholarship coordinator, for the great support and friendship throughout the program.

I truly enjoyed working with my academic adviser Dr. George Tsoflias. The most important for me things that Dr. Tsoflias taught me include how to conduct an independent research under minor supervision, properly manage my time, and maintain high standards of professional ethics. I am thankful to my MS thesis committee, Dr. Ross Black and Dr. Lynn Watney, for their interest in my research project, fruitful discussions and helpful comments. Data for this research were collected and processed by different companies within the South-central Kansas CO₂ project of the Kansas Geological Survey (KGS) funded by the Department of Energy (DOE). I am grateful to the KGS, all the companies and people involved in this big project for providing me a wonderful set of data, for useful multidisciplinary discussions, feedback, support and interest in my work. I would like to say special thanks to Dr. Lynn Watney, the principal investigator of this project and my MS committee member, Jason Rush, co-principal investigator, and Mina Fazelalavi, engineering research assistant. My work greatly benefited from the formation porosity logs processed by Mina, discussions of the geological implications of my geophysical research with Jason Rush and Dr. Lynn Watney. Besides that, I would like to thank the faculty, staff and the students of the Geology Department, especially Dr.

Anthony W. Walton and geophysics students, including Matt Baker, Chris Perrl, Jose Velez, Anthony Hoch, and Blair Benson.

Last but not least, I am grateful to my wonderful fiancée Victoria Romanova who have been patiently waiting for me and supporting me, my parents, Anvar and Sariya, older brother Aydar and younger brother Azat and sister Elza, all my relatives and friends. Especially, I would like to say thank you to my grandma Iliza, uncle Ramil and aunt Tamara; my fiancée's mom Irina and grandparents; the Persian brotherhood, including Hadi, Ehsan, Ali, Morteza, Saman, my best non-Persian friend Omer Malik, Misha Tsy-pin, Pavel Panko and many others.

TABLE OF CONTENTS

ABSTRACT.....iii

ACKNOWLEDGMENTS.....v

TABLE OF CONTENTS.....vii

LIST OF FIGURES AND TABLES.....ix

CHAPTER 1: INTRODUCTION.....1

CHAPTER 2: FIELD SITE AND GEOLOGICAL SETTING.....6

2.1: Field Site.....6

2.2: Geological Setting.....6

2.3: Reservoir Architecture at the Wellington Field.....7

**CHAPTER 3: MODELING THE SEISMIC RESPONSE OF A
RAMP-TRANSITION VELOCITY FUNCTION.....13**

3.1: Methodology.....13

3.2: Modeling the Seismic Response of a Ramp-Transition Velocity Function.....14

CHAPTER 4: METHODOLOGY.....21

4.1: Well Log Interpretation.....21

4.1.1: Well Log Data.....21

4.1.2: Well Log Correlation.....22

4.2: Pseudo-sonic Well Logs.....25

4.3: Seismic Data Interpretation.....31

4.3.1: Seismic Data.....31

4.3.2: Conventional Seismic Interpretation.....32

4.3.3: Instantaneous seismic attributes.....34

4.3.4: <i>Seismic Wedge Modeling Using Original Sonic Logs</i>	35
4.4: <i>Post-stack Model-based Inversion</i>	52
4.4.1: <i>Initial Impedance Model</i>	53
4.4.2: <i>Model-based Inversion Analysis and Application</i>	53
4.4.3: <i>Model-based Inversion of the Synthetic Wedge Models</i>	55
4.5: <i>Multiattribute porosity prediction</i>	71
4.5.1: <i>Multilinear regression analysis</i>	71
4.5.2: <i>Porosity prediction</i>	75
CHAPTER 5: RESULTS AND DISCUSSION	85
5.1: <i>Well Log Interpretation</i>	85
5.2: <i>Pseudo-sonic Well Logs</i>	90
5.3: <i>Seismic Data Interpretation</i>	90
5.3.1: <i>Conventional Seismic Interpretation and Analysis of Instantaneous Seismic Attributes</i>	90
5.3.2: <i>Seismic Wedge Modeling Using Original Sonic Logs</i>	97
5.4: <i>Post-stack Model-based Inversion</i>	110
5.4.1: <i>Model-based Inversion of PSTM Seismic Data</i>	110
5.4.2: <i>Model-based Inversion of the Synthetic Wedge Models</i>	112
5.5: <i>Porosity prediction</i>	114
CHAPTER 6: CONCLUSIONS	121
REFERENCES	126

LIST OF FIGURES AND TABLES

FIGURES

Figure 2.1 - Wellington Field location

Figure 2.2 - Generalized stratigraphic section for central KS and well-to-seismic tie

Figure 2.3 - Paleogeographic and depositional conditions map for Kansas

Figure 2.4 - Reservoir architecture of the Mississippian chert at the Wellington Field

Figure 3.1 - Wedge model of the layer with a ramp-transition velocity function

Figure 3.2 - Seismic amplitude response of a ramp-transition velocity function

Figure 3.3 - Seismic frequency response of a ramp-transition velocity function

Figure 3.4 - Crossplot of seismic amplitude versus downward porosity gradient

Figure 4.1 - Mississippian depth map based on well data

Figure 4.2 - Interpretation of gamma ray and neutron porosity logs at well #15-191-22591

Figure 4.3 - Sonic, neutron porosity and gamma ray logs at wells #15-191-20789 and 15-191-22591

Figure 4.4 - Linear regression analysis at wells #15-191-20789 and 15-191-22591

Figure 4.5 - Predicted vs actual sonic measurements at wells #15-191-20789 and 15-191-22591

Figure 4.6 - Comparison of pseudo-sonic and original sonic logs at wells #15-191-20789 and 15-191-22591

Figure 4.7 - Basemap of the seismic survey at the Wellington Field

Figure 4.8 - Well-to-seismic tie at well #15-191-22591

Figure 4.9 - Null-phase wavelet statistically estimated from the seismic data

Figure 4.10 - Constant-phase wavelet estimated from well and seismic data

Figure 4.11 – Seismic section along inline #152

Figure 4.12 – Seismic section along crossline #158

Figure 4.13 – Seismic section along arbitrary line #1

Figure 4.14 – Location of arbitrary line #1

Figure 4.15 - Amplitude envelope map of the Mississippian reflection

Figure 4.16 - Instantaneous frequency map of the Mississippian reflection

Figure 4.17 - Synthetic seismic section of the reservoir wedge model at well #15-191-20789

Figure 4.18 - Synthetic seismic section of the reservoir wedge model at well #15-191-22591

Figure 4.19 - Amplitude envelope vs reservoir thickness for wedge at well #15-191-20789

Figure 4.20 – Instantaneous frequency vs reservoir thickness for wedge at well #15-191-20789

Figure 4.21 - Amplitude envelope vs reservoir thickness for wedge at well #15-191-22591

Figure 4.22 – Instantaneous frequency vs reservoir thickness for wedge at well #15-191-22591

Figure 4.23 – Two-way travel time thickness vs reservoir thickness for wedge at well #15-191-20789

Figure 4.24 – Two-way travel time thickness vs reservoir thickness for wedge at well #15-191-22591

Figure 4.25 - General workflow for post-stack seismic inversion

Figure 4.26 - High-frequency impedance model along inline #152

Figure 4.27 - High-frequency impedance model along crossline #158

Figure 4.28 - Low-frequency impedance model along inline #152

Figure 4.29 - Low-frequency impedance model along crossline #158

Figure 4.30 - Analysis of model-based inversion at wells #15-191-20789 and 15-191-22591

Figure 4.31 - Inverted impedance vs original impedance within the interval between the Lecompton Limestone and the Arbuckle Group

Figure 4.32 - Model-based inverted impedance section along inline #152

Figure 4.33 - Model-based inverted impedance section along crossline #158

Figure 4.34 - Analysis of model-based inversion result within the Mississippian chert reservoir

Figure 4.35 - Inverted impedance vs original impedance within the Mississippian chert reservoir

Figure 4.36 - Analysis of model-based inversion of synthetic wedge model at well #15-191-20789

Figure 4.37 - Analysis of model-based inversion of synthetic wedge model at well #15-191-20789

Figure 4.38 - RMS inversion error vs wedge thickness

Figure 4.39 - RMS validation error vs number of seismic attributes for different lengths of convolutional operator

Figure 4.40 - RMS prediction and validation errors vs number of seismic attributes for convolutional operator length of 1

Figure 4.41 - Inverted acoustic impedance vs integrate attribute within the Mississippian chert

Figure 4.42 - Inverted acoustic impedance vs formation porosity within the Mississippian chert

Figure 4.43 - Analysis of porosity predictions from inverted impedance in the Mississippian chert

Figure 4.44 - Result of formation porosity prediction along inline #152

Figure 4.45 - Result of formation porosity prediction along crossline #158

Figure 5.1 - Mississippian chert reservoir delineated on porosity logs of well group #1

Figure 5.2 - Mississippian chert reservoir delineated on porosity logs of well group #2

Figure 5.3 - Two-way travel time thickness between MissTop and Mbase reflections

Figure 5.4 - Raw seismic amplitude of MissTop horizon vs reservoir thickness at well group #1

Figure 5.5 – Amplitude envelope of MissTop horizon vs reservoir thickness at well group #1

Figure 5.6 – Instantaneous frequency of MissTop horizon vs reservoir thickness at well group #1

Figure 5.7 – Amplitude envelope averaged within 9 traces of MissTop horizon vs reservoir thickness at well group #1

Figure 5.8 – Instantaneous frequency averaged within 9 traces of MissTop horizon vs reservoir thickness at well group #1

Figure 5.9 – Amplitude envelope of MissTop horizon vs porosity gradient at well group #1

Figure 5.10 – Instantaneous frequency of MissTop horizon vs porosity gradient at well group #1

Figure 5.11 – Thickness map of the Mississippian reservoir predicted from amplitude envelope

Figure 5.12 - Raw seismic amplitude of MissTop horizon vs reservoir thickness at well group #2

Figure 5.13 – Amplitude envelope of MissTop horizon vs reservoir thickness at well group #2

Figure 5.14 – Instantaneous frequency of MissTop horizon vs reservoir thickness at well group #2

Figure 5.15 - Inverted impedance section of synthetic seismic section at well #15-191-20789

Figure 5.16 - Inverted impedance section of synthetic seismic section at well #15-191-22591

Figure 5.17 - RMS porosity prediction and validation errors vs well number

TABLES

Table 4.1 Overview of the 3D PSTM seismic data at the Wellington Field

Table 4.2. Summary of the well-to-seismic tie at the Wellington Field

Table 4.3. Seismic attributes used in the multilinear regression analysis

Table 4.4. Result of multilinear regression analysis using one-point convolutional operator

CHAPTER 1: INTRODUCTION

Geologically complex Mississippian chert reservoirs are important hydrocarbon resources in North America (Montgomery et al., 1998; Rogers and Longman, 2001; Watney et al., 2001). Even though commonly grouped as cherts, these reservoirs can be formed under various depositional and diagenetic conditions (Mazzullo et al., 2009; Rogers, 2001; Saller et al., 2001; Watney et al., 2001; Young, 2010). Numerous petroleum fields in south-central Kansas produce from cherts which replaced previously precipitated carbonates through silicification and calcite dissolution during the post-Mississippian subaerial exposure (Montgomery et al., 1998; Watney et al., 2001). Rogers (2001) reported both in-situ weathered chert-rich carbonates and those that were transported by debris flow in north-central Oklahoma. Core studies in northwest Cherokee County, southeast Kansas, revealed the importance of hydrothermal fluids for porosity enhancement in addition to the diagenetic processes associated with the subaerial exposure (Young, 2010). Several studies also described chert formation from predominantly spiculitic sediments with minor carbonates in west-central Texas, southern Kansas and northern Oklahoma (Mazzullo et al., 2009; Saller et al., 2001). Even though significant differences occurred in the depositional and diagenetic histories, all these studies reported highly heterogeneous microporous vuggy cherts with high porosity (25-50%) and permeability (5-500 md) values. Fractures in chert reservoirs can locally enhance permeability or serve as flow barriers (Montgomery, 1998; Montgomery et al., 1998; Montgomery et al., 2000; Ruppel and Barnaby, 2001; Ruppel and Hovorka, 1995; Saller et al., 1991).

Well and seismic data have been used to map these heterogeneous reservoirs in the subsurface. Well data, such as logs and cores, provide high-resolution information along the borehole but are one-dimensional (1D) resulting in laterally sparse geological information. 3D

seismic data calibrated to geological information at well locations allow reservoir mapping and predictions of reservoir properties throughout the area of interest. Conventional interpretation of 3D seismic data has been used to understand the structural control on chert reservoirs in highly faulted Permian basin fields, Texas (Montgomery, 1998; Reblin et al., 1991; Saller et al., 2001). Recent studies used geometrical seismic attributes, coherence and curvature, to delineate possible fracture zones and link them to high-quality reservoirs or flow barriers (Elebiju et al., 2011; Fu et al., 2006; Nissen et al., 2009; Padgett and Nester, 1991). However, porosity plays a more important role than fractures for many chert fields (Rogers and Longman, 2001). Several studies have predicted porosity in cherts from seismic data (Fu et al., 2006; Phan and Sen, 2010; Thomasson et al., 1989; Sarg and Schuelke, 2003; Schuelke et al., 1997), and limited work has been published on the acoustic properties of cherts measured in the laboratory (Fu et al., 2006). Early study by Thomasson et al. (1989) exploited synthetic seismic modeling using original sonic logs and modified thickness and P-wave velocity of chert reservoirs to match 2D seismic data collected at two fields in south-central Kansas and northern Oklahoma. Their synthetic models reasonably matched seismic data, but the accuracy of the interpretation is questionable due to the insufficient well control at both fields and non-uniqueness of the problem. Fu et al. (2006) reported a linear relationship between porosity and both compressional (P) and shear (S) wave velocities of eleven core samples of Devonian cherts from Texas as well as barely distinguishable fluid effect on velocities. Acoustic impedance derived from seismic data also showed a good correlation with well-log porosity values (Fu et al., 2006). In addition, the multiattribute transform of seismic data to porosity values can incorporate other post- and pre-stack attributes using multilinear regression analysis or neural networks (Hampson et al., 2001).

This technique improves porosity predictions in chert reservoirs in comparison to the use of acoustic impedance alone (Phan and Sen, 2010; Sarg and Schuelke, 2003; Schuelke et al., 1997).

A characteristic porosity reduction with increasing depth was observed on the well-log data within the Mississippian chert reservoir at the Wellington Field, south-central Kansas. This downward porosity decrease might be caused by a combined effect of depositional lithology and limited in depth diagenetic alteration associated with the post-Mississippian subaerial exposure (Watney et al., 2001; W. L. Watney, 2012, personal communication). A similar downward porosity reduction trend was observed on the well logs of the burrowed chert reservoir at the Dollarhide Field, west Texas (Montgomery, 1998; Saller et al., 2001). Such vertical porosity reduction might be very common in chert as well as carbonate reservoirs associated with unconformities. The observed decrease in porosity with depth at the Wellington Field causes a gradational downward increase in P-wave velocity on sonic logs, or a ramp-transition velocity function. Seismic response of the layer characterized by a ramp-transition velocity function exhibits characteristic decreases in signal amplitude and frequency as the layer thickness increases (Sengbush et al., 1961). The reflection from transitional layers has been extensively studied in theory (Berryman et al., 1958; Gupta, 1966; Sengbush et al., 1961; Wolf, 1937). A ramp-transition velocity function was also used to test the algorithms of synthetic seismogram calculation (Sherwood, 1962; Wuenschel, 1960). Few recent studies attempted to use the seismic response of a ramp-transition function to characterize transitional layers (Gomez and Ravazzoli, 2012; Liner and Bodmann, 2010; Sloan et al., 2007). Sloan et al. (2007) studied the amplitude variation with offset (AVO) response of a partially saturated zone with varying thickness induced by pumping using near-surface seismic data. Gomez and Ravazzoli (2012) analyzed the amplitude variations with angle (AVA) and frequency (AVF) of the reflection from a modeled

layer characterized by linearly increasing CO₂ saturation. Liner and Bodmann (2010) analyzed the frequency-dependence of the reflection from a transitional layer using spectral decomposition of both synthetic and 2D field seismic data. The transitional layer in their field example corresponded to the change from seafloor mud to lithified sediments. According to all these recent studies, AVO, AVA, AVF and spectral decomposition can be potentially used to detect the layers characterized by a ramp-transition velocity function and predict their properties. Overall, limited studies have reported the use of the seismic response of a ramp-transition velocity function in reservoir characterization. Thomasson et al. (1989) mentioned a ramp-transition velocity function as one of the possible factors affecting seismic amplitude at one of the chert fields in south-central Kansas. So, even though the theoretical seismic response of a ramp-transition velocity function has been recognized for a long time in exploration geophysics, its utility as a potential reservoir characterization tool has not been fully explored using field seismic data.

In this study I conduct a seismic attribute analysis of the Mississippian chert reservoir at the Wellington Field, south-central Kansas, using 3D pre-stack time migrated (PSTM) seismic data. According to the well logs, this field is characterized by a gradational downward porosity decrease and corresponding increase in velocity within the reservoir interval. I examine post-stack seismic attributes on both real and synthetic seismic data in order to find possible relationships with reservoir properties. This study investigates if thickness of the reservoir with gradational downward porosity decrease can be predicted using the theoretical seismic signature of a ramp-transition velocity function. Particularly, I explore if decreases in signal amplitude and frequency with increasing reservoir thickness can be observed in field seismic data and used for thickness prediction. In addition, I perform post-stack model-based inversion of the seismic data

and estimate the resolving power of this inversion approach in case of the Mississippian reservoir characterized by a downward increase in acoustic impedance. Finally, I use multilinear regression analysis to determine potential seismic attributes for porosity prediction in the Mississippian reservoir at the Wellington Field using the approach described by Hampson et al. (2001). Based on the results of the multilinear regression analysis, I use inverted acoustic impedance alone to predict the porosity distribution within the Mississippian reservoir. The reliability of predictions is tested by blind wells excluded from the analysis.

This research evaluates the use of the seismic response of a ramp-transition velocity function, well established in theory, but poorly studied using real seismic data, for prediction of the thickness of the Mississippian chert reservoir at the Wellington Field. Additionally, the resolution of the model-based inversion, poorly defined in the literature and commonly referred as enhancing the resolution of seismic data, is evaluated for the case of the gradational impedance increase within the reservoir interval. Finally, I discuss the porosity distribution within the Mississippian chert reservoir based on the porosity model predicted from inverted acoustic impedance and the reservoir thickness predicted from amplitude envelope. Results of this study can be useful for the investigations of similar chert fields in south-central Kansas and elsewhere in the world. In addition to predicting the reservoir thickness, the seismic response of a ramp-transition velocity function related to downward porosity reduction might be useful in understanding depositional and diagenetic histories of such reservoirs. This research could also benefit the characterization of clastic and carbonate reservoirs as downward porosity reduction might be also found in these reservoirs.

CHAPTER 2: FIELD SITE AND GEOLOGICAL SETTING

2.1: Field Site

The Wellington Field, Sumner County, south-central KS, is located in the mature Midcontinent US petroleum province (Figure 2.1). Since its discovery in 1929, more than 250 wells have been drilled in the field area of 22.6 km². As of July 2011, the cumulative oil production from the Mississippian chert exceeded 20 millions barrels of oil. Currently, the Wellington Field is experiencing a decrease in secondary production with 47 producing and 15 water-injecting wells (KGS, 2012).

2.2: Geological Setting

The local geology is comprised of interbedding clastics and carbonates with distinct changes in acoustic impedance that favor subsurface imaging with the reflection seismic method as shown by the good agreement between synthetic and field seismic data at well #15-191-22591 (Figure 2.2).

The reservoir rocks of the middle Mississippian age (Osagean-Meramecian) were deposited on the carbonate shelf that covered a greater part of the central US including south Kansas (Figure 2.3; Montgomery et al., 1998). Sponge-rich shelf and shelf margin environments were characterized by transgressive-regressive cycles (T-R) of silica- and carbonate-rich sediments (Watney et al., 2001; Franseen, 2006). Oval or irregular in shape biohermal buildups, rich in sponge spicules, developed on the shelf margin reaching up to 48 meters in thickness (Montgomery et al., 1998). Deposited sediments underwent a series of diagenetic events associated with the post-Mississippian subaerial exposure (Montgomery et al., 1998; Watney et al., 2001). Early silicification, carbonate dissolution and dolomitization formed microporous and vuggy cherts and cherty dolomites (Watney et al., 2001). Diagenesis was limited in depth as well

as decreased in the downdip direction due to topographic influence and facies change (Montgomery et al., 1998; Watney et al., 2001). Chert conglomerates, up to 3 meters thick, overlie chert reservoirs and often exhibit less porosity and permeability values due to clay-filled fractures (Montgomery et al., 1998; Watney et al., 2001). Lower Pennsylvanian shales, tens of meters thick, present a regional cap rock for the Mississippian chert reservoirs.

2.3: Reservoir Architecture at the Wellington Field

According to the core analysis at well #15-191-22591 at the Wellington Field, the Mississippian strata shallows upward changing from dark shales and shaly carbonates to pale yellowish brown cherts and cherty dolomites (W. L. Watney, 2012, personal communication). The reservoir at the Wellington Field consists of microporous and vuggy cherty dolomites having less cherty, more dolomitic content and less vuggy pore space comparing to the tripolitic chert reservoirs at the adjacent fields (W. L. Watney, 2012, personal communication). A thick shale package of the Cherokee Group (Lower Pennsylvanian), up to 50 m thick, forms a cap rock.

Characteristic reservoir architecture can be observed on the well logs (Figure 2.4). The Mississippian chert at the Wellington Field is characterized by high porosity values (25%) at the reservoir top and gradational porosity decrease to 4-6% at the reservoir base. This characteristic downward porosity reduction is caused by the combined effect of the shallowing upward depositional lithology and diagenetic alteration caused by the water infiltration limited in depth (W. L. Watney, 2012, personal communication). Gradational density (from 2.31 to 2.67 g/cc) and velocity (from 3800 to 5300 m/s) increases correspond to this downward decrease in porosity (Figure 2.4). The gradational velocity increase, or a ramp-transition velocity function, is expected to result in waveform integration and characteristic decreases in signal amplitude and frequency as the layer thickness increases (Sengbush et al., 1961). Therefore, seismic amplitude

and frequency responses can be potentially used for mapping thickness and porosity of the Mississippian chert reservoir at the Wellington Field.

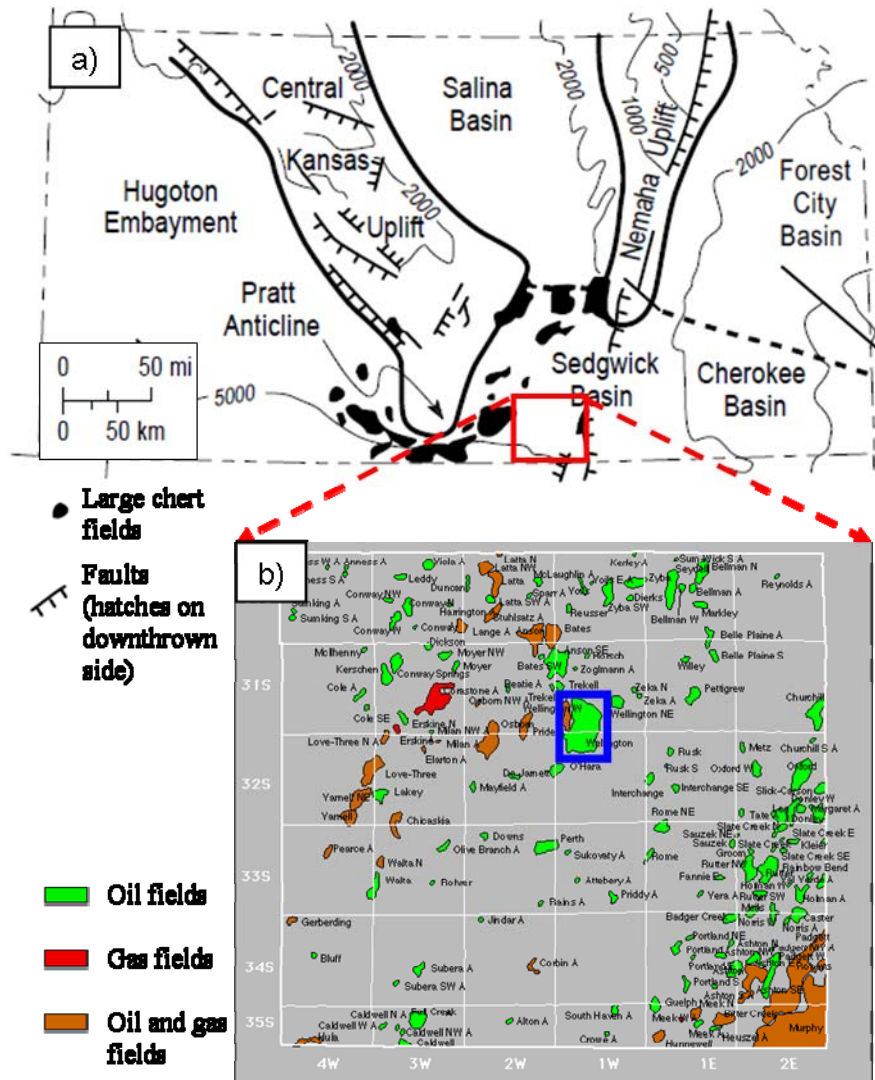


Figure 2.1. Wellington Field location: a) Location of the Sumner County (red box) within the major tectonic elements during the late Mississippian-early Pennsylvanian time in Kansas. Modified from Montgomery et al. (1998); b) Oil and gas fields located within the Sumner County. The Wellington Field is outlined with the blue box. Modified from KGS (2012).

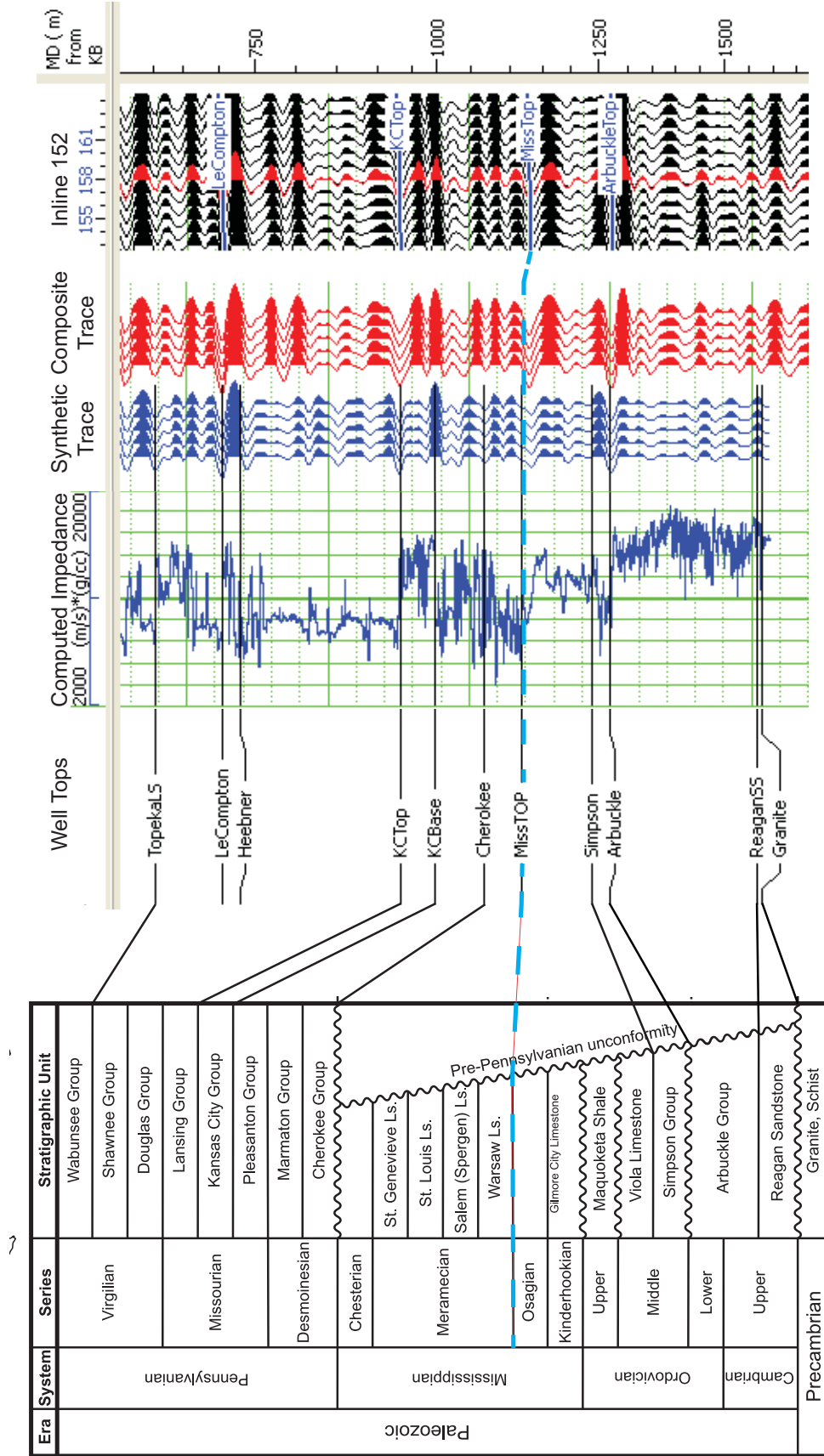


Figure 2.2. From left to right: generalized stratigraphic section for central Kansas (Modified from Nissen et al. (2009), originally from Cansler (2000)); well tops, computed impedance log, synthetic (blue) and seismic (red) traces (both repeated 5 times; SEG reversed polarity) at well #15-191-22591; part of inline #152. The Mississippian reservoir top is identified by the blue dashed line.

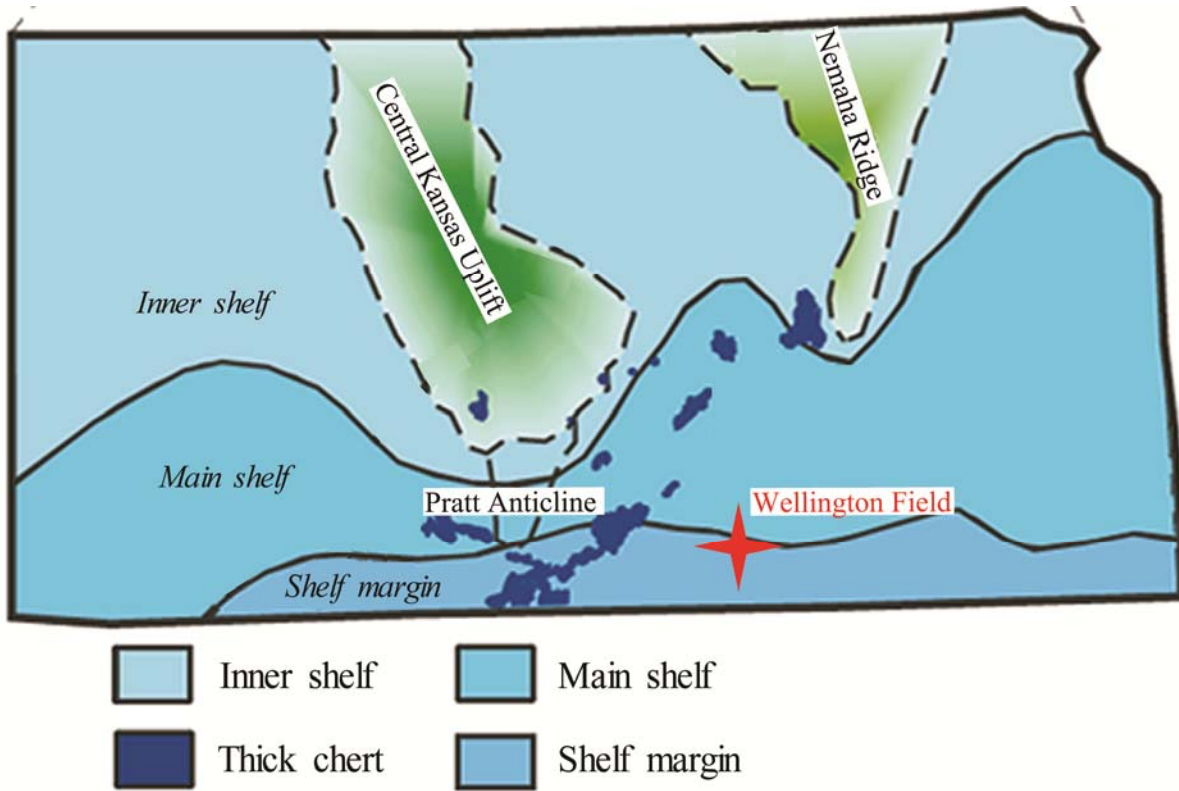


Figure 2.3. Paleogeographic and depositional conditions in Kansas during the Mississippian time. Red star shows the location of the Wellington Field. Modified from Franseen (2006).

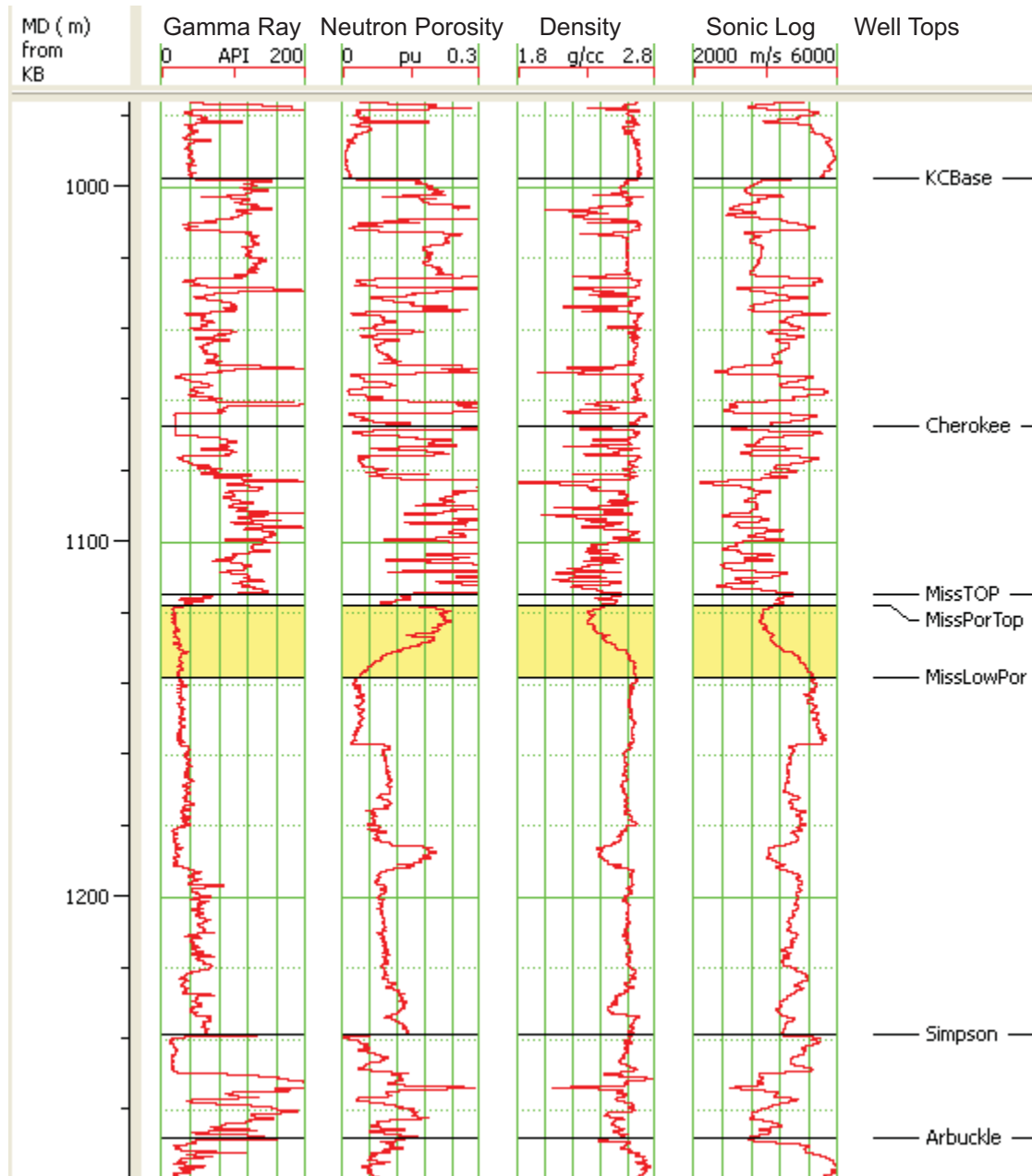


Figure 2.4. Characteristic architecture of the Mississippian chert reservoir at the Wellington Field according to the well logs at well #15-191-22591. Note the interval (highlighted in yellow) with downward porosity reduction (from 25 to 4%) and corresponding gradational velocity (from 3800 to 5300 m/s) and density (from 2.31 to 2.67 g/cc) increases.

CHAPTER 3: MODELING THE SEISMIC RESPONSE OF A RAMP-TRANSITION VELOCITY FUNCTION

In order to demonstrate the theoretical seismic response of a ramp-transition velocity function, one-dimensional (1D) normal incidence seismic modeling was conducted in MATLAB using a synthetic depth-velocity model.

3.1: Methodology

The interval of a sonic log in which velocity increases (or decreases) linearly with depth from the velocity of the overlying layer to the velocity of the underlying layer is defined as a ramp-transition velocity function (Sengbush et al., 1961). A ramp-transition velocity function has the effect of integration on the seismic wavelet which results in lower amplitude and frequency responses (Sengbush et al. 1961; Costain and Çoruh, 2004). The theoretical seismic response of a ramp-transition velocity function was examined for the Mississippian chert reservoir by creating a synthetic three-layer velocity model and calculating the corresponding synthetic seismic traces in MATLAB.

I built a three-layer synthetic velocity model by taking approximate sonic log values from wells #15-191-20789 and 15-191-22591. The velocity model consists of: 1) an upper thick layer with constant velocity of 3600 m/s, 2) a middle ramp-transition layer with velocity linearly increasing with depth from 3600 to 5300 m/s, and 3) a lower thick layer with constant velocity of 5300 m/s (Figure 3.1a). The middle layer represents a wedge with thickness increasing from 1.1125 to 66.75 m. A synthetic seismic section was calculated by convolving the velocity model with a 55 Hz Ricker wavelet (Figure 3.1b). The frequency of the seismic wavelet was chosen based on the frequency content of the PSTM seismic data at the Wellington Field described later in section 4.3. The synthetic seismic section consisted of 60 traces with 1.1125 m increase of

wedge thickness between adjacent traces. Amplitude envelope and instantaneous frequency sections were calculated from the seismic section using the Hilbert transform (Taner et al., 1979; Figures 3.2-3.3). Amplitude envelope ($A(t)$) and instantaneous frequency ($f(t)$) were calculated according to Taner et al. (1979) as following:

$$A(t) = \sqrt{[x^2(t) + x^{*2}(t)]} \text{ and}$$

$$f(t) = d[\arctan(x^*(t)/x(t))]/dt$$

where $x(t)$ – real part of the complex seismic trace,
 $x^*(t)$ - imaginary part of the complex seismic trace.

The wavelength (λ) within the ramp-transition interval was calculated using the following equation:

$$\lambda = V_{average} / f,$$

where $V_{average}$ – average velocity within the ramp-transition interval: $V_{average} = (V_1 + V_2)/2$,
 $V_1 = 3600 \text{ m/s}$ - velocity at the top of the ramp,
 $V_2 = 5300 \text{ m/s}$ - velocity at the base of the ramp,
 $f = 55 \text{ Hz}$ - peak frequency of the Ricker wavelet.

3.2: Modeling the Seismic Response of a Ramp-Transition Velocity Function

The synthetic seismic and attribute sections illustrate the theoretical seismic response of a ramp-transition velocity function which represents a simplified model of the Mississippian chert reservoir at the Wellington Field (Fig. 3.1-3.3). The seismic response is discussed with respect to the ramp thickness (1.1125-66.75 m) and the seismic signal wavelength ($\lambda = 80.9 \text{ m}$).

When the ramp thickness is greater than $1/2\lambda$ (40 m), two distinct reflections are observed at the top and the bottom of the ramp (Fig. 3.1b). Both reflections represent an integrated source wavelet, which is a trough followed by a peak for a Ricker wavelet (Costain and Çoruh, 2004): a

positive reflection occurs at the ramp top and a negative reflection at the ramp bottom. As the ramp thickness decreases, the two reflections start merging into a single reflection, and a composite waveform is observed for thicknesses less than 30 m ($3/8\lambda$). Reflection amplitude asymptotically decreases from 0.05 to 0.025 within the range 30-67 m, whereas instantaneous frequency slightly increases from 41 to 43 Hz within the same range (Fig. 3.2c, 3.3c).

A single reflection is observed when the ramp thickness is less than 30 m (Figure 3.1b). Both raw seismic amplitude and amplitude envelope linearly decrease from 0.19 to 0.05, or 74%, with increasing thickness in the range 5-30 m ($1/16\lambda - 3/8\lambda$), while instantaneous frequency exhibits a linear decrease from 53 to 44 Hz, or 17%, within the range 10-20 m ($1/8\lambda - 1/4\lambda$) and a smoother decrease within the ranges 0-10 and 20-30 m (Figures 3.2c, 3.3c).

The observed decrease in signal amplitude relates to a gradient of velocity increase and, therefore, to a gradient of porosity decrease within the reservoir. The reflection amplitude linearly increases from 0 to 0.17 as the porosity gradient increases from 0 to 2 %/m (Figure 3.4). In case of the Mississippian reservoir with downward porosity decrease from 25 to 4%, this porosity gradient range corresponds to the thickness range from an infinitely thick reservoir to 10 m ($1/8\lambda$). As the porosity gradient increases further, the reflection amplitude approaches the amplitude of a reflection from a step velocity function due to a sharp impedance contrast between Pennsylvanian shales and tight Mississippian limestone. Porosity gradient might benefit understanding depositional and diagenetic histories of the reservoir.

Modeling of the seismic response of the ramp-transition velocity function demonstrate that signal amplitude and frequency can be potentially used to predict the thickness of a reservoir characterized by a gradational downward velocity increase, such as the Mississippian at the Wellington Field. An overall reflection amplitude and frequency decrease would result from

increasing thickness of the reservoir. For a dominant frequency of 55 Hz, raw seismic amplitude and amplitude envelope attributes exhibit linear decreases of 74% over the interval 5-30 m, whereas instantaneous frequency shows a smaller linear decrease of 17% within the shorter interval 10-20 m.

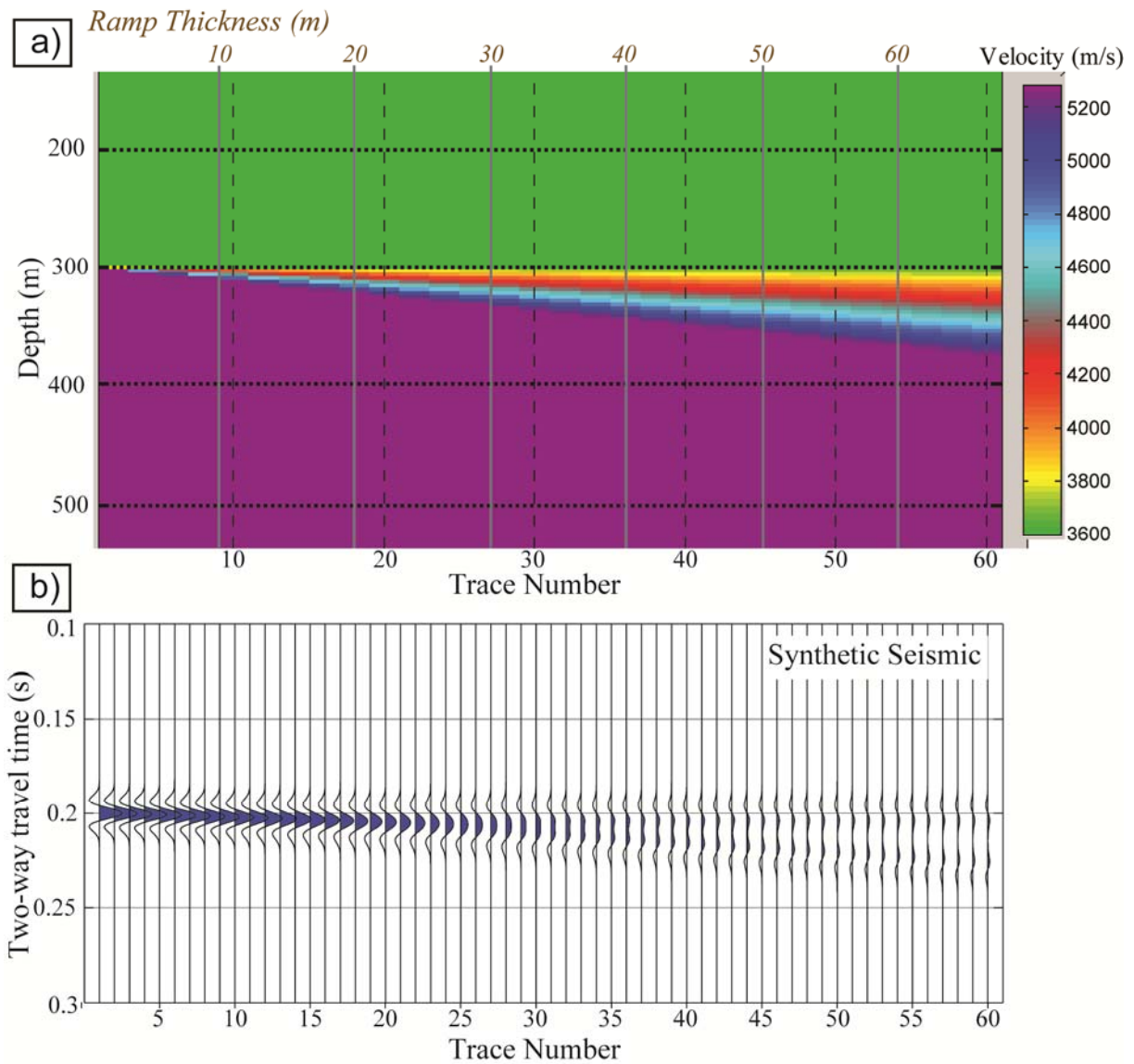


Figure 3.1. Wedge model of the layer characterized by a ramp-transition velocity function: a) depth-velocity model; b) corresponding synthetic seismic section computed by the convolution of the depth-velocity model with a 55 Hz Ricker wavelet.

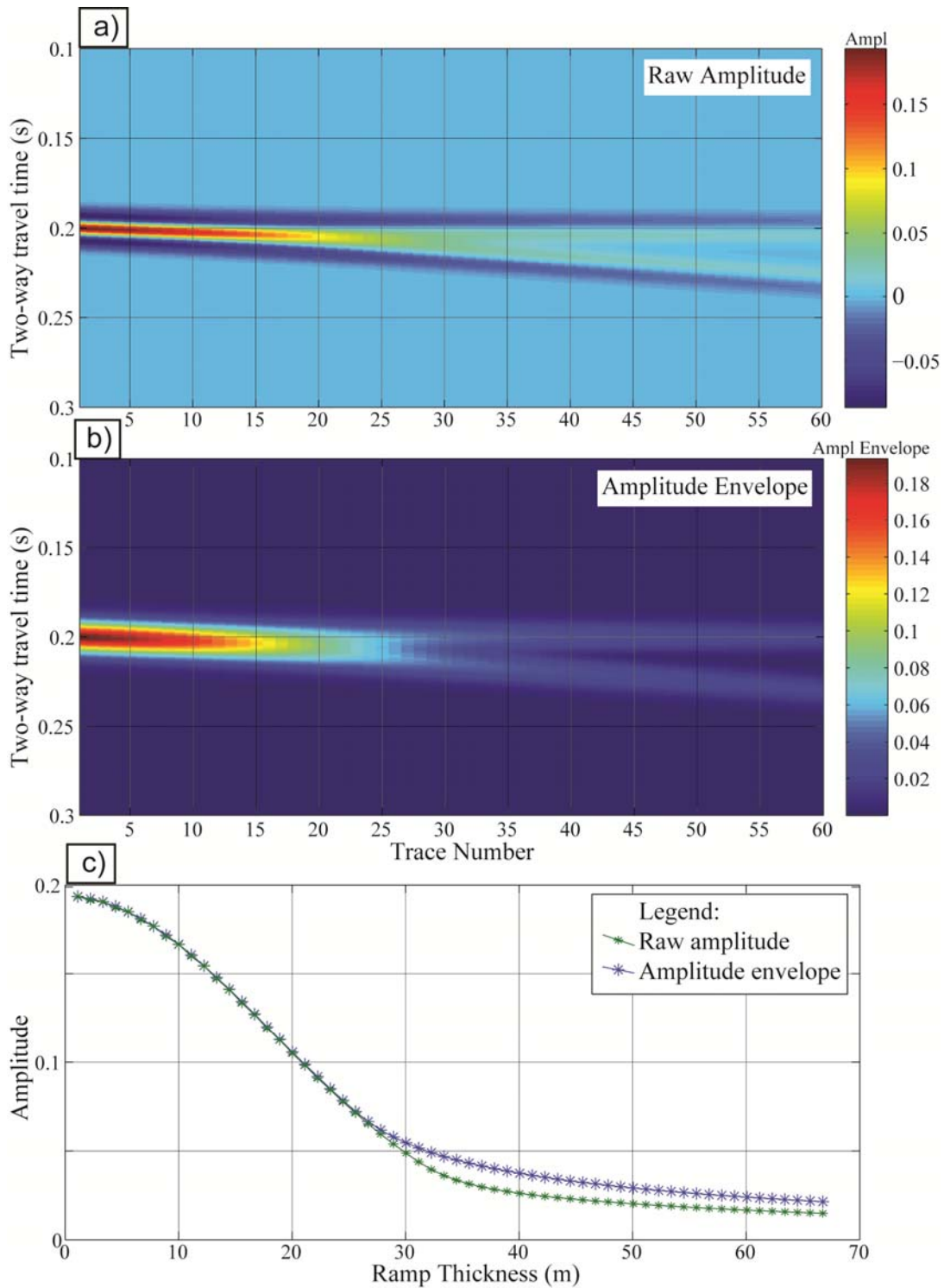


Figure 3.2. Seismic amplitude response of a wedge model of a ramp-transition velocity function: a) raw seismic amplitude section; b) amplitude envelope section; c) crossplots of raw seismic amplitude and amplitude envelope attributes taken at the peak of the top reflection versus ramp thickness. Note the decrease in waveform amplitude as the ramp thickness increases.

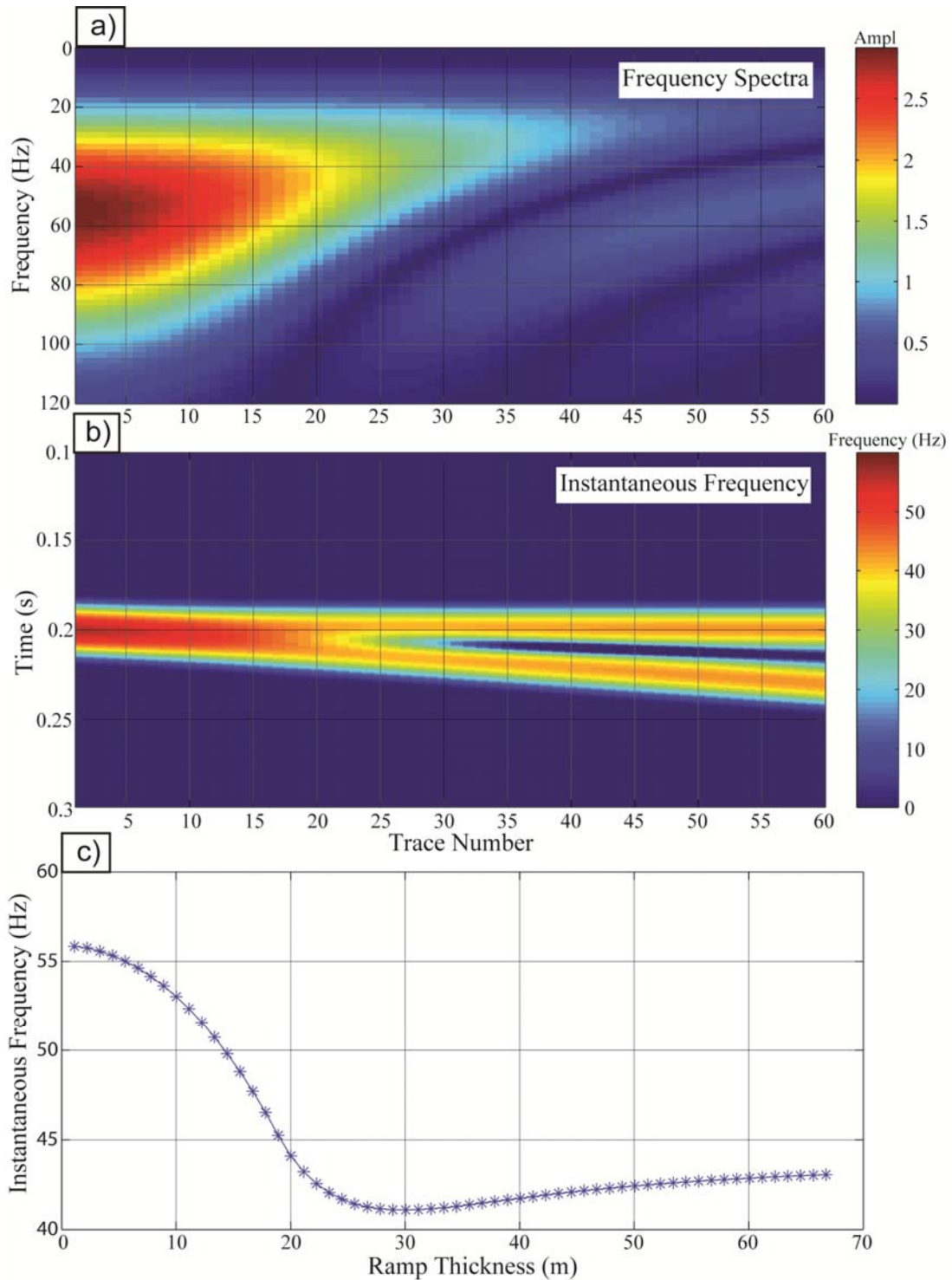


Figure 3.3. Seismic frequency response of a wedge model of a ramp-transition velocity function: a) frequency spectra; b) instantaneous frequency section; c) crossplot of the instantaneous frequency attribute taken at the peak of the top reflection versus ramp thickness. Note the decrease in waveform frequency as the ramp thickness increases.

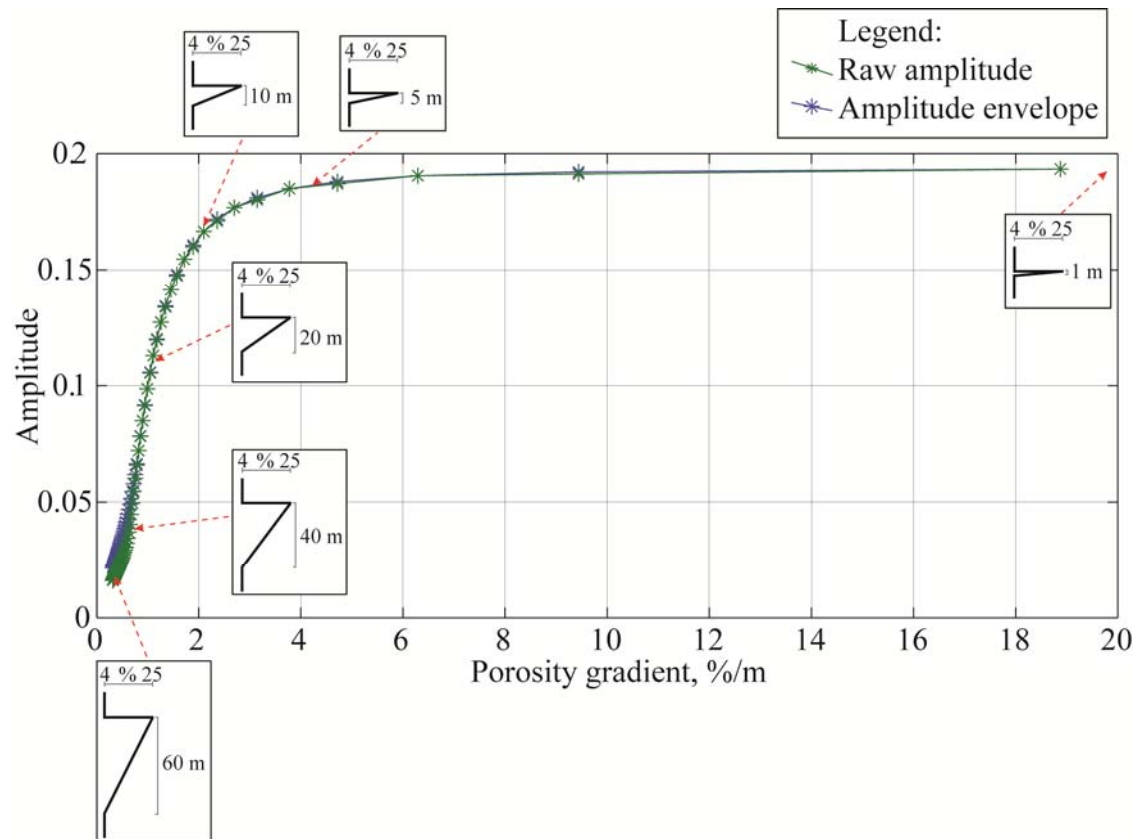


Figure 3.4. Crossplots of raw seismic amplitude and amplitude envelope versus the downward porosity gradient (%porosity/m) within the reservoir.

CHAPTER 4: METHODOLOGY

4.1: Well Log Interpretation

Well log data were used to correlate major stratigraphic horizons and delineate the Mississippian reservoir in order to establish a stratigraphic framework and determine the reservoir porosity and thickness. Pseudo-sonic logs were generated in order to tie wells with porosity logs to seismic data. Well-log porosity information tied to seismic data allowed the multilinear regression analysis for porosity prediction using multiple seismic attributes as described in section 4.5.

4.1.1: Well Log Data

Well log data, including geologic, gamma ray, density, sonic, neutron porosity and density porosity logs, were downloaded from the Digital Petroleum Atlas of the Wellington Field at the KGS website. Additionally, formation porosity logs computed by Mina Fazelalavi (KGS) from sonic, neutron porosity and density porosity logs in Schlumberger TechLog software were used in this project. For the purposes of this study, I chose twenty five wells penetrating the Mississippian reservoir: one well with a sonic log only, two wells with formation porosity and sonic logs, eleven wells with formation porosity logs, seven wells with density porosity logs, and four wells with density porosity and neutron porosity logs (Figure 4.1). The three wells containing sonic logs were used to tie seismic to well data as described in section 4.3.2. Formation porosity logs were considered to be the most reliable source of porosity information within the Mississippian reservoir as the effects of the lithology were removed by the combination of sonic, density and neutron porosity logs. Therefore, only those thirteen wells with formation porosity logs were used in the multiattribute porosity prediction as described in section 4.5. However, all the wells containing any kind of porosity logs were used to pick the

reservoir top and bottom in order to investigate if the theoretical seismic response of a ramp-transition velocity function can be potentially used to predict reservoir thickness at the Wellington Field as described in section 5.3.1. Interpretation of the well-log data was conducted in the Hampson-Russell software.

4.1.2: Well Log Correlation

Correlation of the well-log data was limited to picking major stratigraphic horizons and delineating the Mississippian chert reservoir using gamma ray and porosity logs (Figure 4.2). Well picks corresponding to the tops of the Topeka Limestone, the Lecompton Limestone and the Heebner shale of the Shawnee Group (Virgilian Stage, Upper Pennsylvanian Series), the top and the base of the Kansas City Group (Missourian Stage, Upper Pennsylvanian Series), the top of the Cherokee Group (Desmoinesian Stage, Middle Pennsylvanian Series), the top of the Mississippian Subsystem, the top of the Simpson Group (Middle Ordovician Series), the top of the Arbuckle Group (Lower Ordovician Series), and the Precambrian basement were downloaded from the KGS website. Gamma ray and geologic logs verify, and when needed, edit these well tops. Following the well-log top correlation across the Wellington Field, detailed analysis was conducted on the chert reservoir associated with the Mississippian unconformity (Figures 2.4, 4.2). The Mississippian top, labeled in figures as MissTOP, corresponded to the top of the in-situ weathered chert conglomerate of about 3-4 m thick and 10% average porosity. The top of the chert reservoir, also being the bottom of the chert conglomerate and labeled as MissPorTop, was picked on the formation porosity logs at the beginning of the high-porosity interval, 24-30%. Porosity gradationally decreases within the chert reservoir; and the reservoir bottom, labeled as MissLowPor was picked at 4-6% cut off porosity.

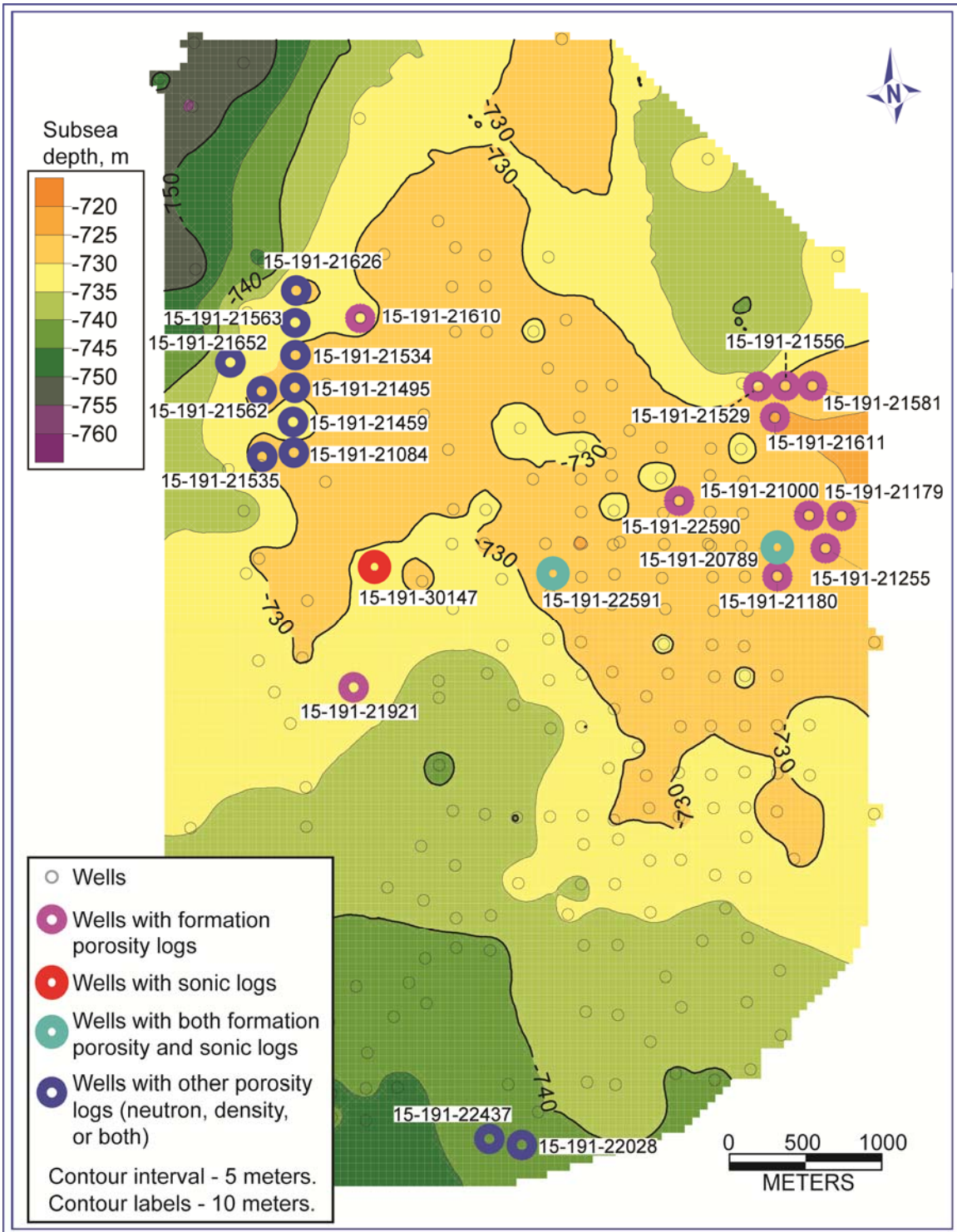


Figure 4.1. Mississippian depth map at the Wellington Field based on well data alone. Wells used in this project are highlighted.

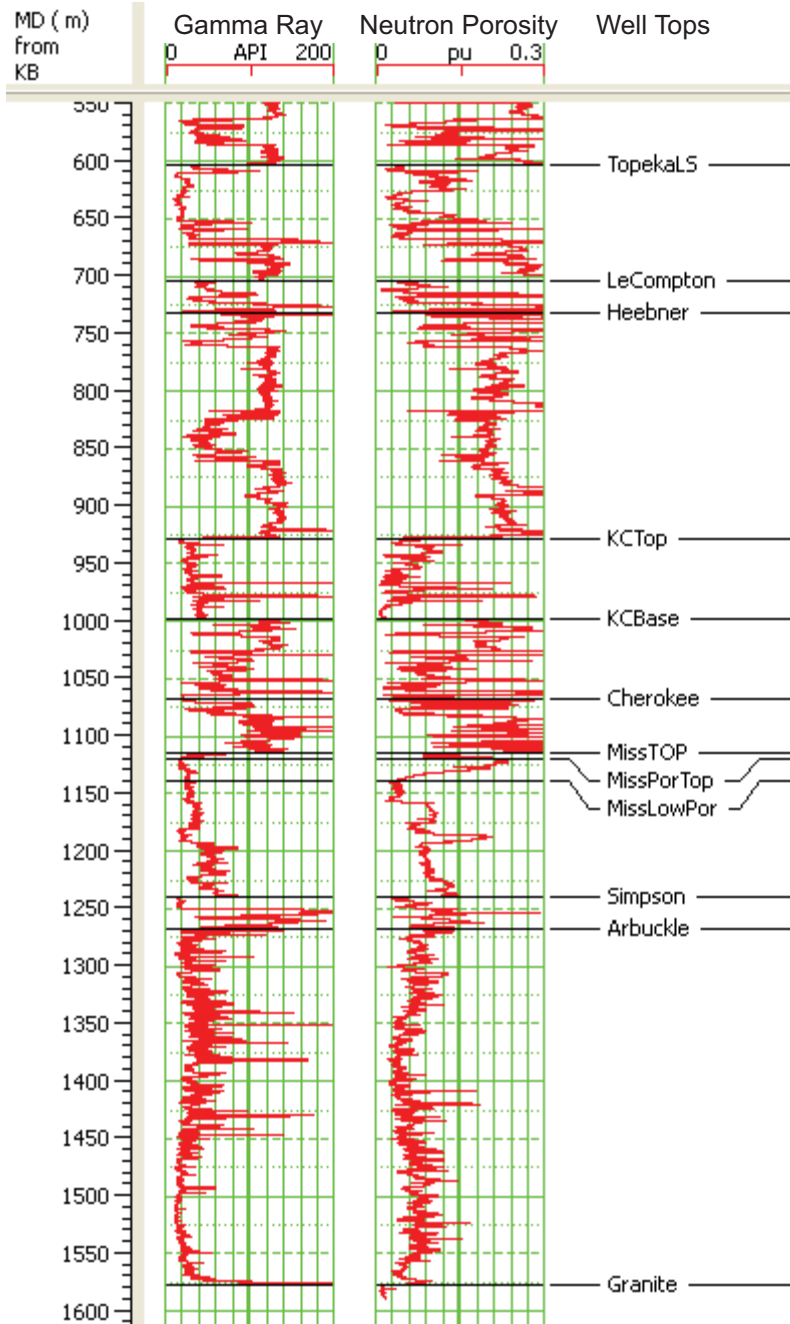


Figure 4.2. Interpretation of the gamma ray and neutron porosity logs at well #15-191-22591. Note the chert conglomerate, 3-4 m thick, between MissTop and MissPorTop, and the reservoir interval with the gradational downward porosity decrease from 25% at the reservoir top (MissPorTop) to 4% at the reservoir bottom (MissLowPor).

4.2: Pseudo-sonic Well Logs

The thirteen wells containing formation porosity logs were selected for the quantitative porosity prediction from multiple seismic attributes as described later in section 4.5. In order to predict porosity from seismic data, formation porosity logs at these thirteen wells should be converted to the two-way travel time domain. However, only two out of selected thirteen wells, #15-191-20789 and #15-191-22591, had sonic logs to perform the well-to-seismic tie. Therefore, pseudo-sonic logs were generated for the other 11 wells in order to tie well-log to seismic data.

I used the Hampson-Russell EMERGE software to predict pseudo-sonic logs from neutron porosity and gamma ray logs using a multiattribute transform. First, the relationship between sonic log and neutron porosity and gamma ray measurements was derived using the step-wise regression analysis of existing logs from the two wells, #15-191-20789 and #15-191-22591 (Figures 4.3-4.6; Hampson et al., 2001). Simple mathematical operations on well logs, such as square, square root, logarithm and inverse, were also considered. Figure 4.3 shows an overall negative linear correlation between sonic logs and both neutron porosity and gamma ray logs at two well locations, #15-191-20789 and #15-191-22591. The linear regression analysis showed high correlation, 0.89, and low prediction error, 22.14 $\mu\text{s/m}$, between sonic and neutron porosity measurements (Figures 4.4a). Gamma ray logs exhibited lower correlation with sonic logs, 0.78, and higher prediction error, 31.27 $\mu\text{s/m}$ (Figure 4.4b). Figure 4.5a shows the crossplot between actual sonic log and the pseudo-sonic log predicted from neutron porosity alone. Multilinear regression analysis exploited both neutron porosity and gamma ray measurements to predict sonic logs. The following relationship was solved for $weight_1$, $weight_2$ and $constant$ using the least-square minimization approach (Hampson et al., 2001):

$$\text{Operator}(\text{Sonic}) = \text{weight}_1 * \text{Operator}(\text{Neutron Porosity}) + \text{weight}_2 * \text{Operator}(\text{Gamma Ray}) + \text{constant}$$

The transform for predicting pseudo-sonic logs was found as:

$$(\text{Sonic})^2 = 160546.95 * (\text{Neutron Porosity}) + 2313.42 * \sqrt{(\text{Gamma Ray})} + 12080.87$$

The use of both neutron porosity and gamma ray logs improved the correlation between actual and predicted sonic log values to 0.916 and decreased prediction error to 19.94 $\mu\text{s}/\text{ft}$ (Figure 4.5b). Pseudo-sonic logs generated for the two test wells, #15-191-20789 and #15-191-22591, closely mimic the actual sonic logs at these wells (Figure 4.6). Finally, the relationship determined using the methodology described above was applied to 11 wells containing neutron porosity and gamma ray logs only in order to calculate pseudo-sonic logs.

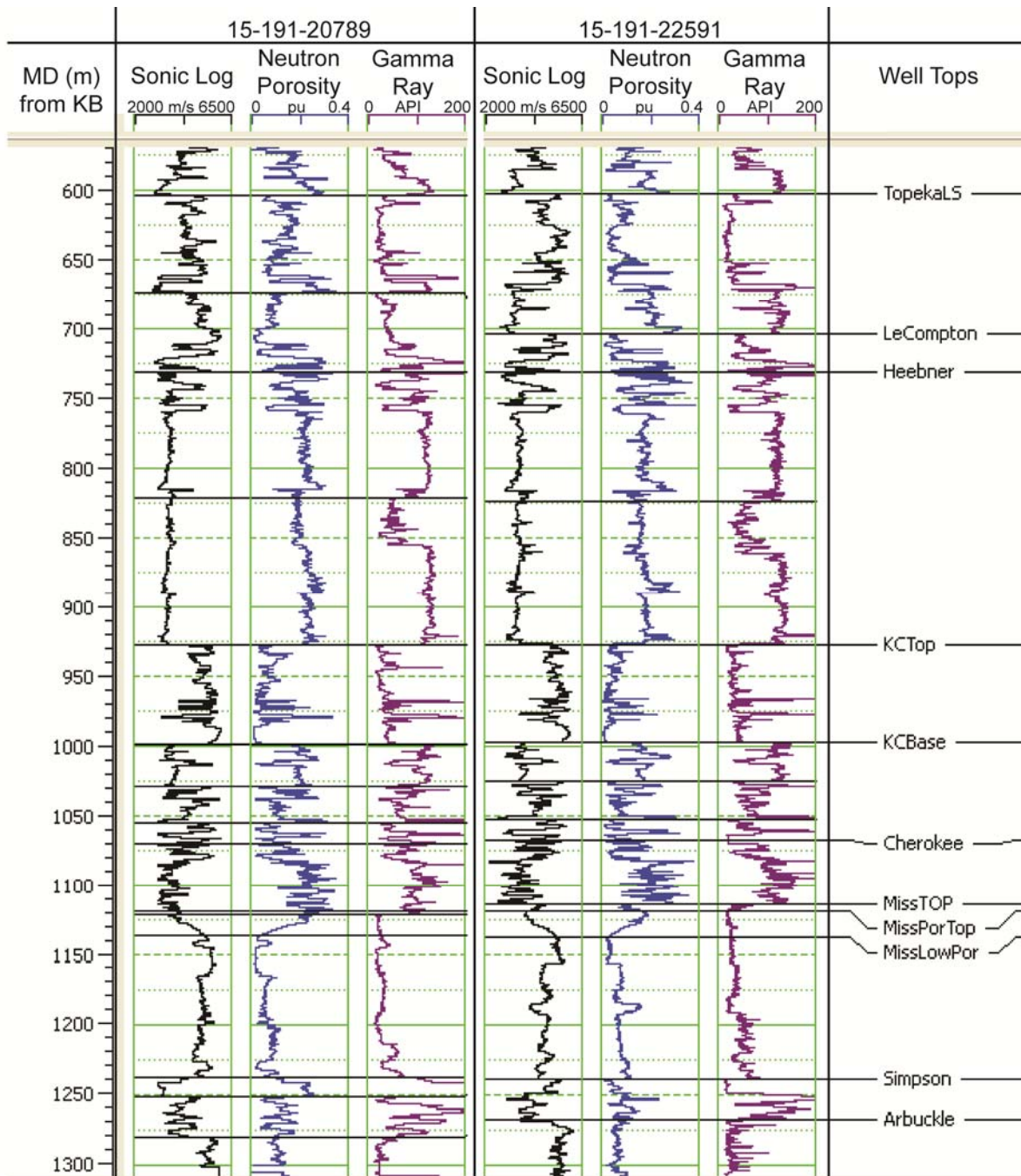


Figure 4.3. Sonic, neutron porosity and gamma ray logs at two wells, #15-191-20789 and #15-191-22591, used in the multilinear regression analysis.

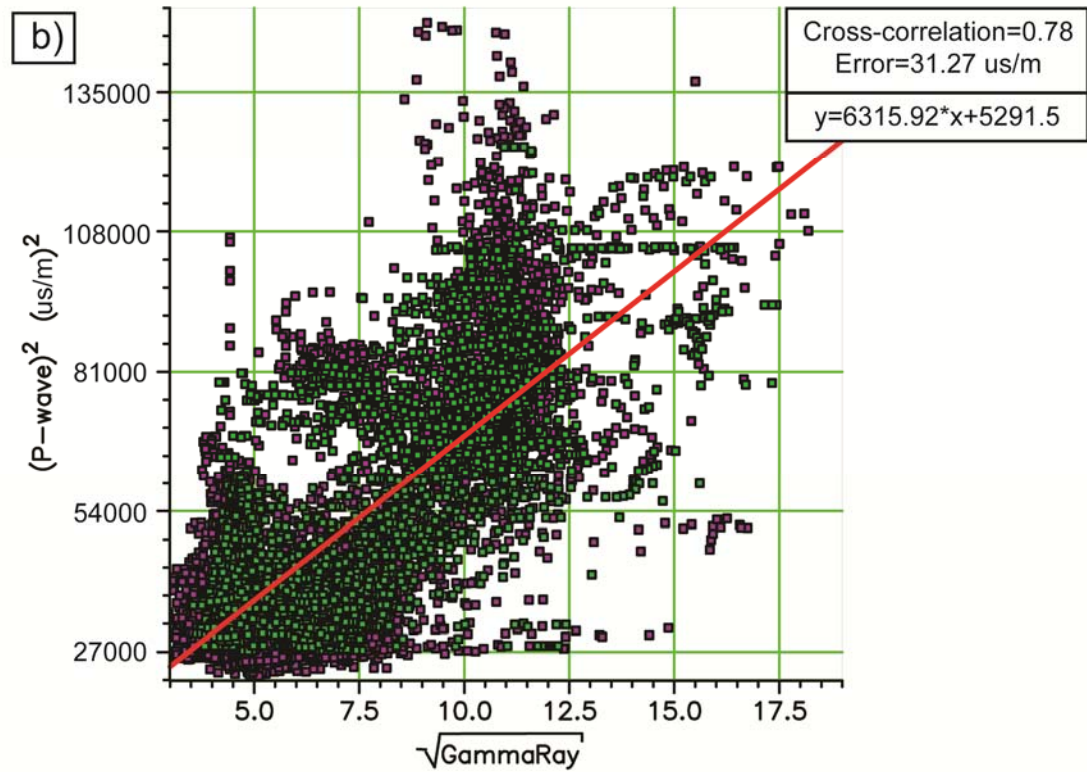
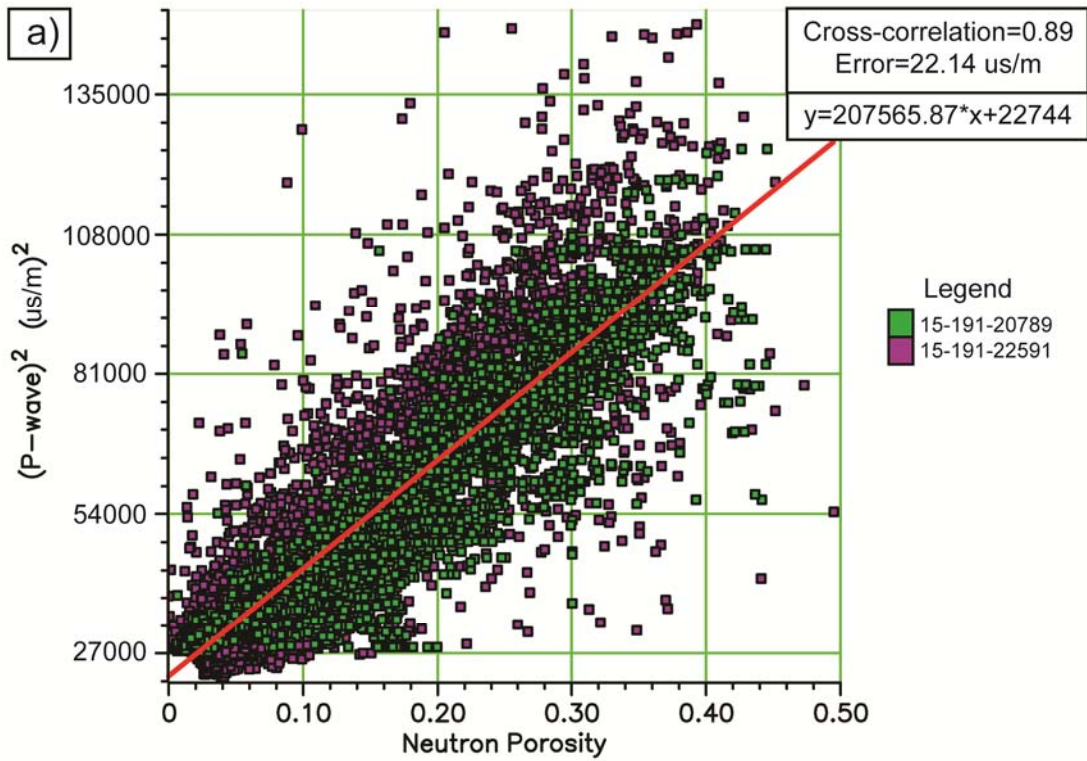


Figure 4.4. Linear regression analyses of a) sonic and neutron porosity; b) sonic and gamma ray measurements at wells #15-191-20789 and #15-191-22591.

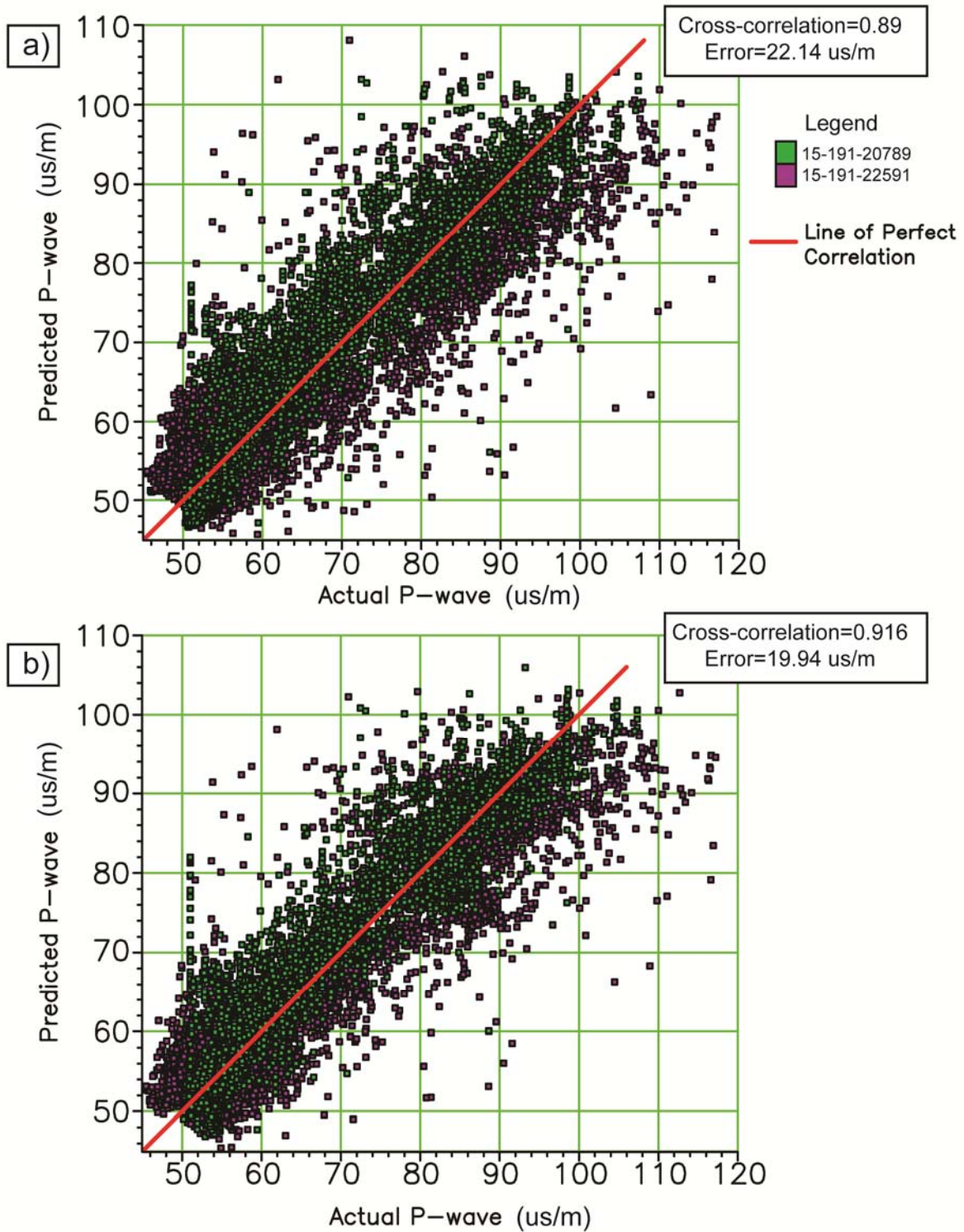


Figure 4.5. Predicted versus actual sonic measurements using a) neutron porosity alone; b) both neutron porosity and gamma ray logs at wells #15-191-20789 and #15-191-22591.

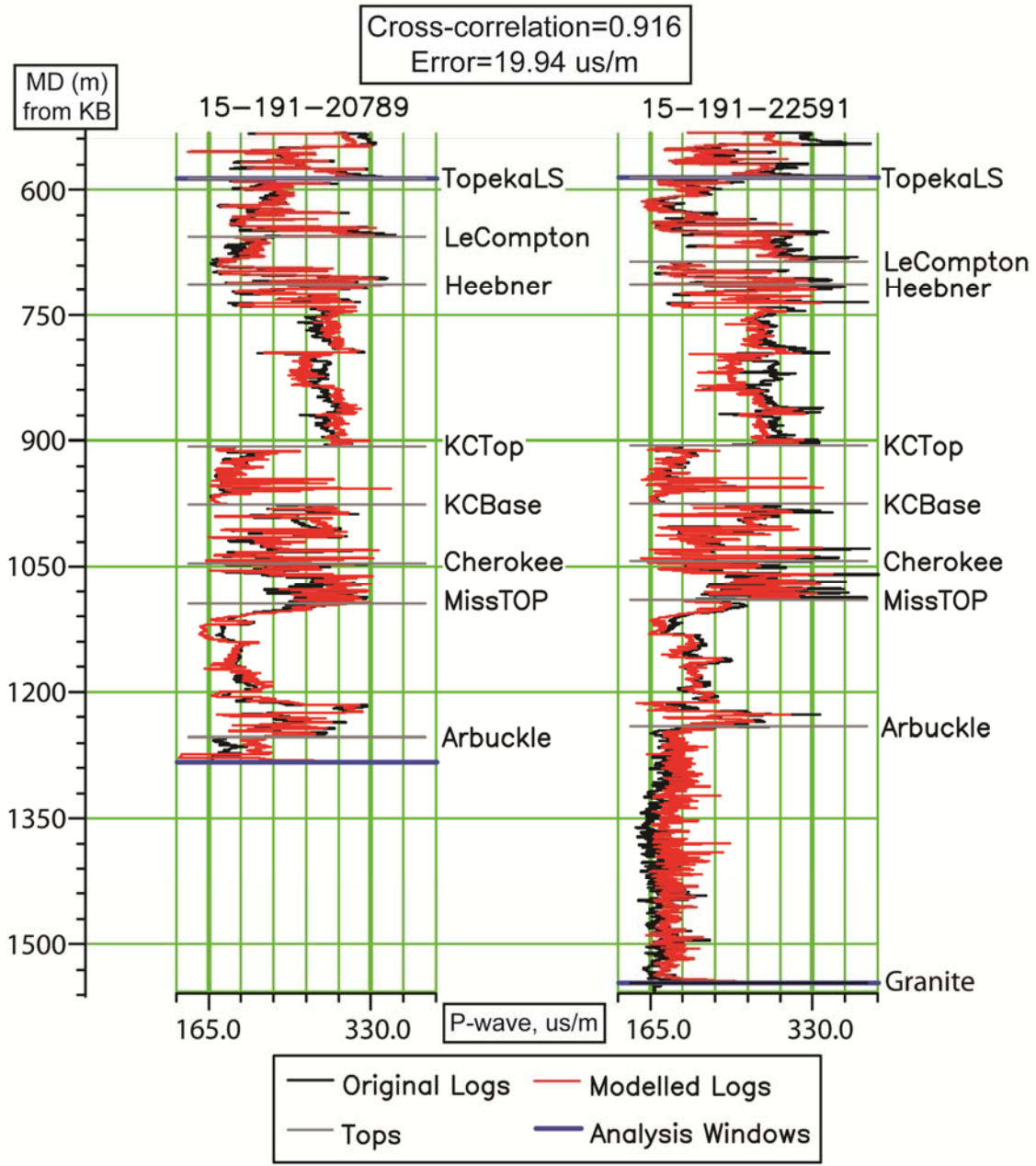


Figure 4.6. Pseudo-sonic logs predicted from neutron porosity and gamma ray logs using multilinear transform (red) versus actual sonic logs at two well locations, #15-191-20789 and #15-191-22591. Cross-correlation coefficient and prediction error was calculated within the analysis window (blue).

4.3: Seismic Data Interpretation

4.3.1: Seismic Data

In 2010, Paragon Geophysical Services Inc. conducted a 3D 3C (three component) seismic survey at the Wellington Field. P-wave data processing was performed by FairfieldNodal in 2010-2011. During the processing stage the Wellington Field data were merged with 3D seismic data from the adjacent Anson-Bates Field. 3D pre-stack time migrated (PSTM) stacked seismic data were received for further geophysical analysis and geological interpretation (Table 4.1). For the purposes of this study, I used the part of the merged seismic volume covering the Wellington Field only, inline range 1-289 and crossline range 73-251, over an approximate area of 28.5 km² (Figure 4.7). Seismic data analysis was implemented using the Hampson-Russell software.

Seismic data	3D pre-stack time migrated; stacked
Bandpass filter	10 – 128 Hz
Seismic datum	396.24 m (1300 ft)
Replacement velocity	3048 m/s (10000 ft/s)
Number of inlines	542 (used range 1-289)
Number of crosslines	251 (used range 73-251)
Bin size	25.146 m (82.5 ft)
Polarity	SEG reversed

Table 4.1. Overview of the 3D PSTM seismic data at the Wellington Field.

4.3.2: Conventional Seismic Interpretation

The 3D PSTM seismic data were conventionally interpreted by creating synthetic seismograms at three well locations in order to tie seismic to well data. Picking seismic horizons associated with the major seismic reflections, such as the tops of the Lecompton Limestone, the Kansas-City Group, the Mississippian System, and the Arbuckle Group, established the main structural framework for the seismic interpretation at the Wellington Field.

Reflection seismic data by its nature image the Earth's subsurface as a set of interfaces corresponding to changes in acoustic impedance. The vertical scale of such observations is two-way travel time. In order to perform a geological interpretation of seismic data, seismic reflections should be correlated to key stratigraphic horizons at well locations. Well-to-seismic tie was achieved by forward modeling, also known as creating synthetic seismograms (Figure 4.8). A statistical null-phase wavelet was derived from the seismic data within the time window 300-800 ms (Figure 4.9). This wavelet has negative polarity as shown in the wavelet time response and by the -180° phase. Therefore the seismic data is SEG reversed polarity. However, I use mostly SEG normal polarity for display purposes, and the polarity used for data display is always specified in the figure captions. Vertical impedance profiles were calculated from the sonic and density logs available at 2 wells, #15-191-20789 and #15-191-22591. The impedance log at well #15-191-30147 was calculated from the sonic log only due to the absence of the density log. These impedance logs were converted to reflectivity functions. Synthetic seismograms were generated by convolving the reflectivity functions with the statistical wavelet. These synthetic traces were shifted, stretched and squeezed to improve the cross-correlation with the seismic trace. Then I extracted an average constant-phase wavelet for three wells using both well and seismic data: 9 seismic traces around each well were used to estimate the amplitude

spectrum within the time window 360-700 ms; and well data was used to find the wavelet phase that provides the lowest least-square error between synthetic and seismic traces (Figure 4.10; Hampson and Galbraith, 1981). Constant-phase wavelet (phase=-179°) confirmed the seismic data is null-phase SEG reversed polarity, and was further used to create synthetic seismograms and later during the acoustic impedance inversion process. High correlation between synthetic and seismic traces was achieved at all three wells (Table 4.2). An example of the well-to-seismic tie at well #15-191-22591 is shown in Figure 4.8. A good match between synthetic and seismic data allowed the correlation of the seismic horizons to the main stratigraphic markers.

Well API number	Correlation coefficient	Time window
15-191-20789	0.864	300-720 ms
15-191-22591	0.79	300-720 ms
15-191-30147	0.82	300-692 ms

Table 4.2. Summary of the well-to-seismic tie at the Wellington Field.

Following the well-to-seismic tie, I picked 4 reflections on seismic data that correspond to the tops of key stratigraphic units: the Lecompton Limestone, the Kansas-City Group, the Mississippian System, and the Arbuckle Group (Figures 4.11-4.12). Automatic horizon tracking worked well for the Lecompton Limestone (labeled as LeCompton) and the Kansas-City Group (labeled as KCTop) tops due to their coherent representation on the seismic data. Significant manual editing was required for the inconsistent reflectors associated with the tops of the Mississippian System (MissTop) and the Arbuckle Group (ArbuckleTop). All seismic horizons were smoothed with the mean average filter, 3 by 3 traces. Also, I saved the unsmoothed version

of the MissTop reflection with horizon picks placed exactly at the peak of the waveform for the instantaneous attribute analysis described in section 4.3.3.

Finally, I examined the interval around the Mississippian reflection. The reflection from the Mississippian top exhibited highly inconsistent and variable character with a locally developed double reflector. In order to honor the double reflector, I copied the MissTop seismic horizon, re-picked the areas with the double reflector only and saved it as a new horizon MBase. Figure 4.13 shows the unsmoothed versions of the MissTop and MBase seismic horizons. The seismic resolution within the Mississippian reservoir was determined in chapter 3 as $\lambda=80.9$ m.

4.3.3: Instantaneous seismic attributes

According to the theoretical seismic response of the ramp-transition velocity function, amplitude envelope and instantaneous frequency responses can be related to the thickness of the layer characterized by linear downward velocity increase. The Mississippian chert reservoir exhibits a gradational downward porosity decrease and corresponding increase in velocity according to the well logs at the Wellington Field as described in sections 2.3 and 4.1. I extracted amplitude envelope and instantaneous frequency maps of the Mississippian reflection in order to investigate if these attributes can be used to predict the reservoir thickness at the Wellington Field.

Amplitude envelope and instantaneous frequency maps of the unsmoothed Mississippian reflection, MissTop, were constructed in the Hampson-Russell software in order to extract the attribute values at the reflection peak (Figures 4.15-4.16). Relationships between these seismic attributes and the reservoir thickness were examined at the wells with available porosity logs.

4.3.4: Seismic Wedge Modeling Using Original Sonic Logs

In order to investigate the seismic response of the chert reservoir characterized by a gradational downward porosity decrease at the Wellington Field, one-dimensional (1D) wedge modeling was performed using original sonic logs at two wells. The first goal of this modeling was to investigate the cause of the double reflector at the top of the Mississippian System as described in Figure 4.13. The second goal was to examine relationships of amplitude envelope and instantaneous frequency attributes with the reservoir thickness using original well logs and to compare it with the theoretical seismic response of a ramp-transition velocity function described in section 3.2.

Two wells, #15-191-20789 and 15-191-22591, with both original sonic and formation porosity logs were selected for reservoir wedge modeling. Reservoir thicknesses were determined during the well-log interpretation as 15 m at well #15-191-20789 and 20 m at well #15-191-22591. The sonic logs were stretched and squeezed within the reservoir interval, between MissPorTop and MissLowPor, to produce synthetic depth-velocity models with reservoir thickness varying from 0 to 50 m. These depth-velocity models were convolved with the wavelet extracted during the well-to-seismic tie (Figure 4.10) to calculate synthetic seismic sections (Figures 4.17-4.18). Synthetic seismic sections consisted of 50 traces with 1 m increase of the wedge thickness between adjacent traces. The original sonic logs are overlain on the synthetic seismic sections in dark green, and synthetic sonic logs are shown in light green for every 5th trace in Figures 4.17-4.18.

The interpretation of the synthetic seismic sections included correlation of the reflections associated with the reservoir, and calculation of amplitude envelope and instantaneous frequency attributes. Two distinct reflections, from the reservoir top and base, were observed for ramp

thicknesses larger than $1/4\lambda$ (Figures 4.17-4.18). These reflections merged and produced a composite reflection as the reservoir thickness decreased. The reflection labeled as Reflection_1 was interpreted as the top reflection on both synthetic seismic sections. Trough and peak, labeled as Reflection_2_Trough and Reflection_2_Peak respectively, were interpreted as the composite reflection from the reservoir base and the thin layer just below the reservoir base on the seismic section built at well #15-191-20789 (Figure 4.17). The reflection, labeled as Reflection_2, was associated with the reservoir base on the seismic section built at well #15-191-22591 (Figure 4.18). Amplitude envelope was calculated at the peak of the Reflection_1 for both synthetic seismic sections and plotted versus the reservoir thickness (Figures 4.19 and 4.21). Instantaneous frequency was calculated as an RMS average within a 5 ms window centered at Reflection_1 (Figures 4.20 and 4.22). Two-way travel time thickness was calculated as the difference between Reflection_1 and Reflection_2_peak for the seismic section built at well #15-191-20789, and Reflection_1 and Reflection_2 for the seismic section built at well #15-191-22591 (Figures 4.23-4.24).

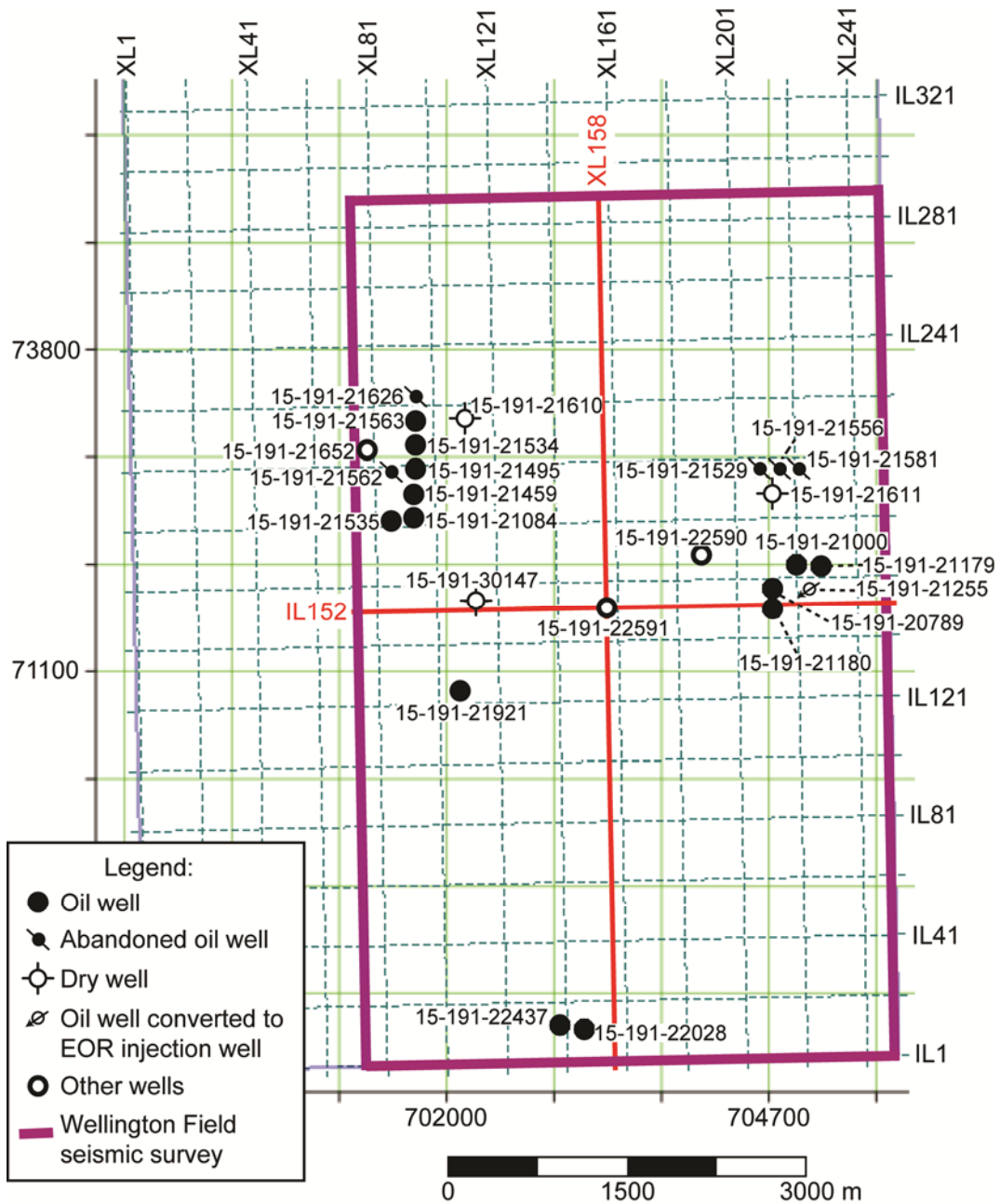


Figure 4.7. Basemap of the seismic survey at the Wellington Field with locations of the wells used in this research project.

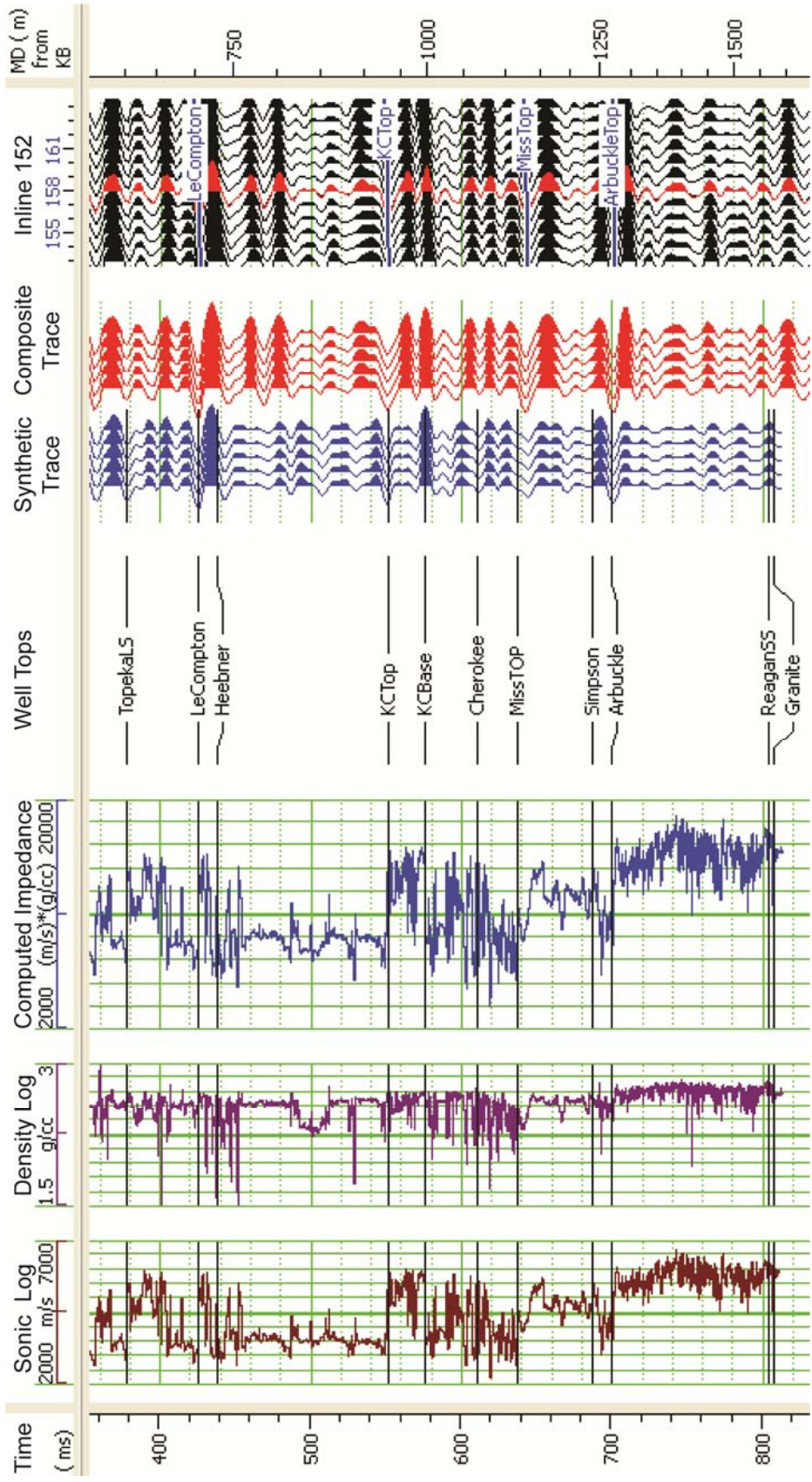


Figure 4.8. Well-to-seismic tie at well #15-191-22591 with 0.796 correlation between synthetic (blue) and seismic (red) traces (both repeated 5 times and displayed in SEG reversed polarity). Constant-phase wavelet shown in Figure 4.10 was used to create synthetic seismogram. Part of the inline #152 is shown in reversed SEG polarity.

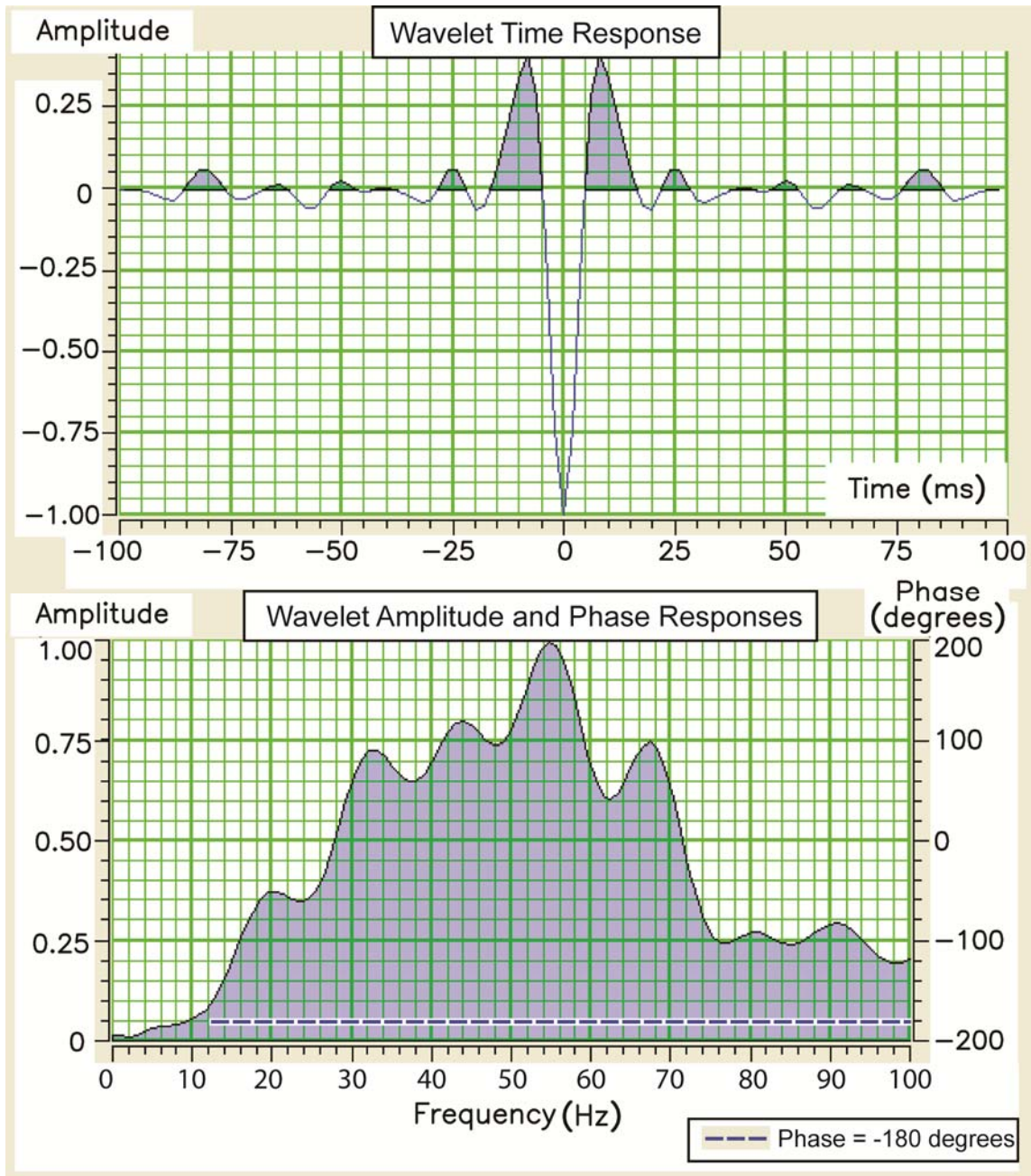


Figure 4.9. Null-phase wavelet statistically estimated from the seismic data within the time window 300-800 ms, and its amplitude and frequency spectra. Note that the wavelet has negative polarity as shown in the wavelet time response and by the -180° phase.

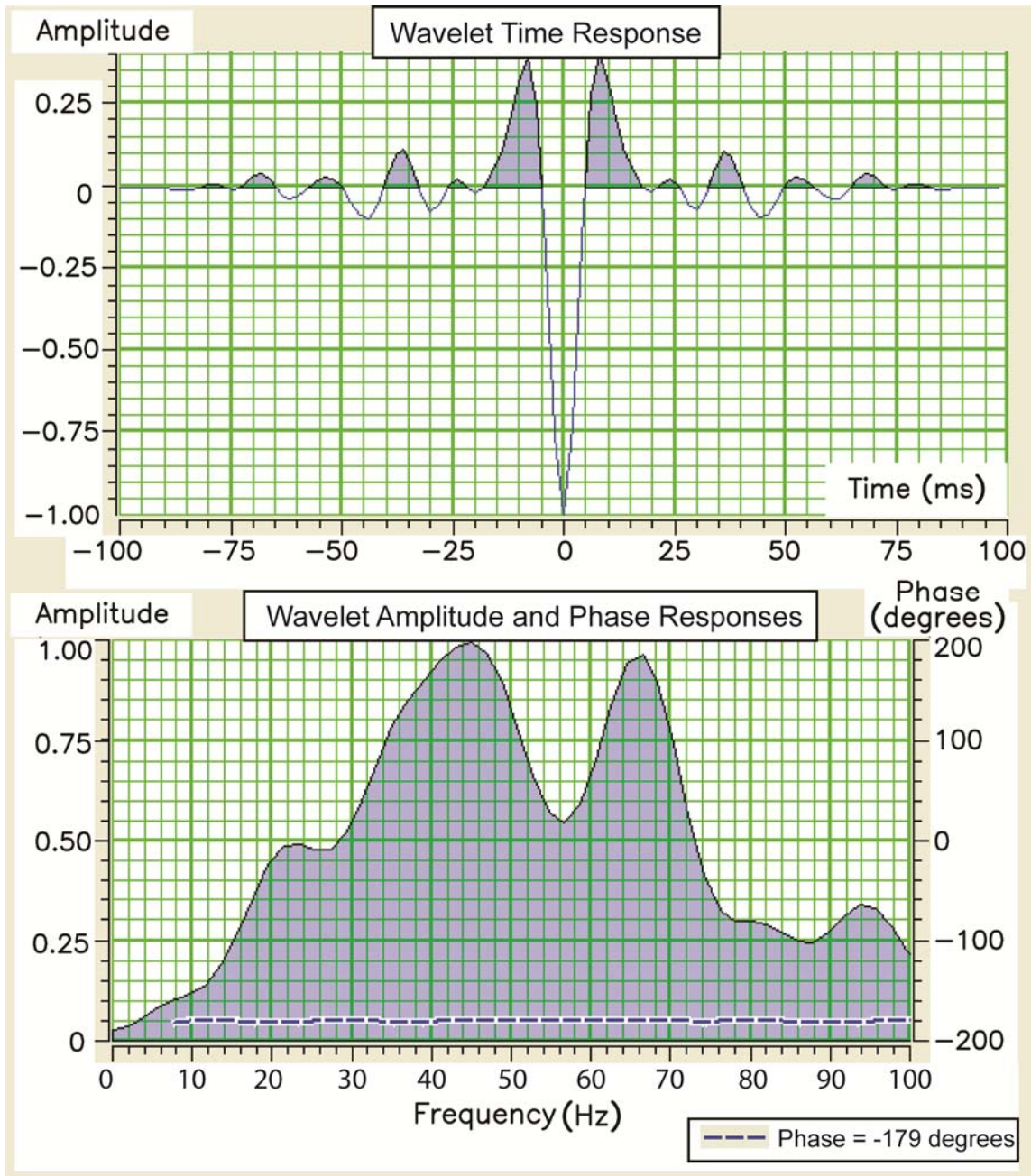


Figure 4.10. Constant-phase wavelet estimated from well and seismic data within the time window 360-700 ms, and its amplitude and frequency spectra. Note that the wavelet has negative polarity as shown in the wavelet time response and by the -179° phase.

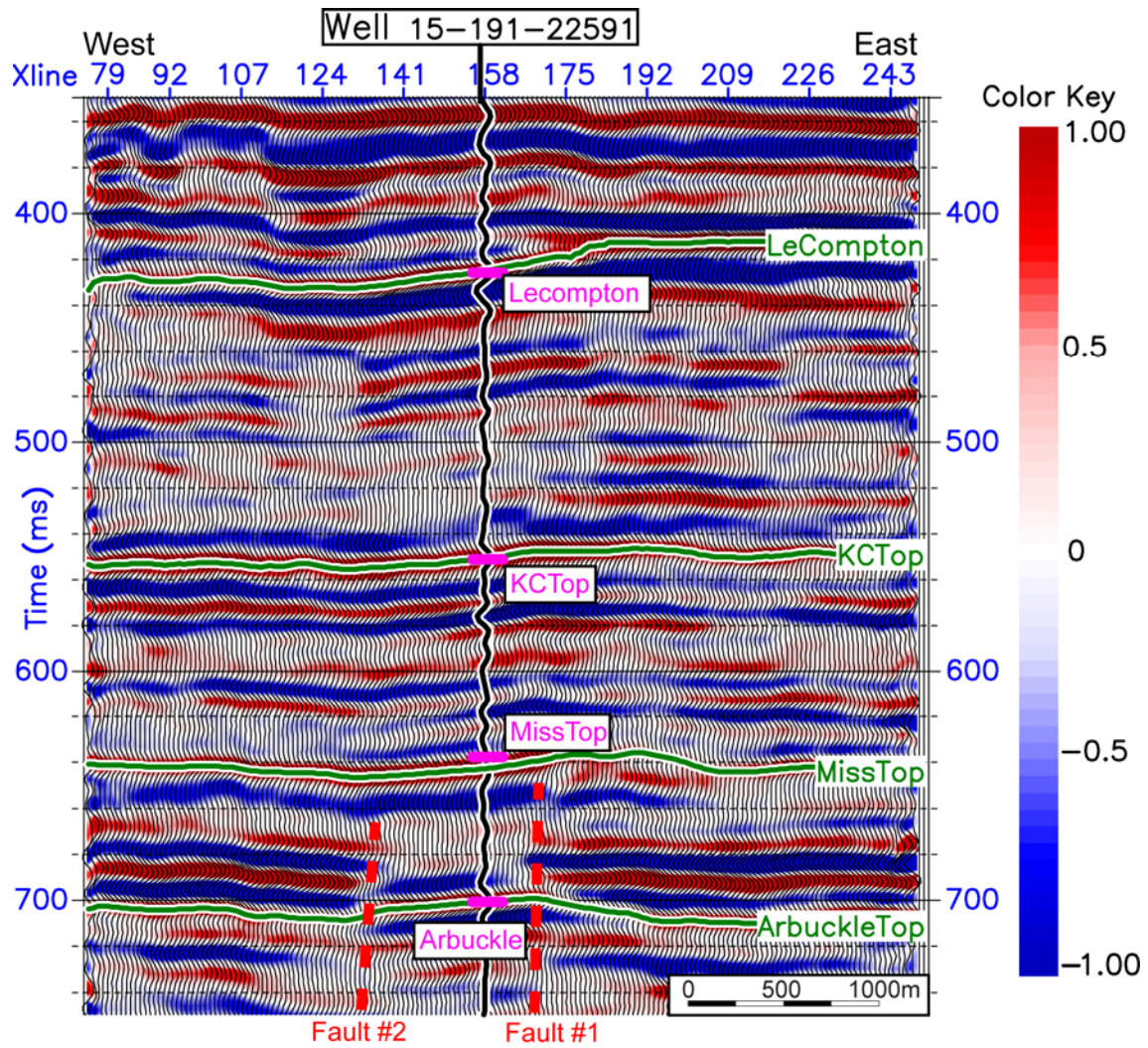


Figure 4.11. Inline #152 with the overlain synthetic seismic trace generated at well #15-191-22591 and interpreted seismic horizons corresponding to the tops of the LeCompton Limestone, the Kansas-City Group, the Mississippian System and the Arbuckle Group (SEG normal polarity). Line location is shown in Figure 4.7.

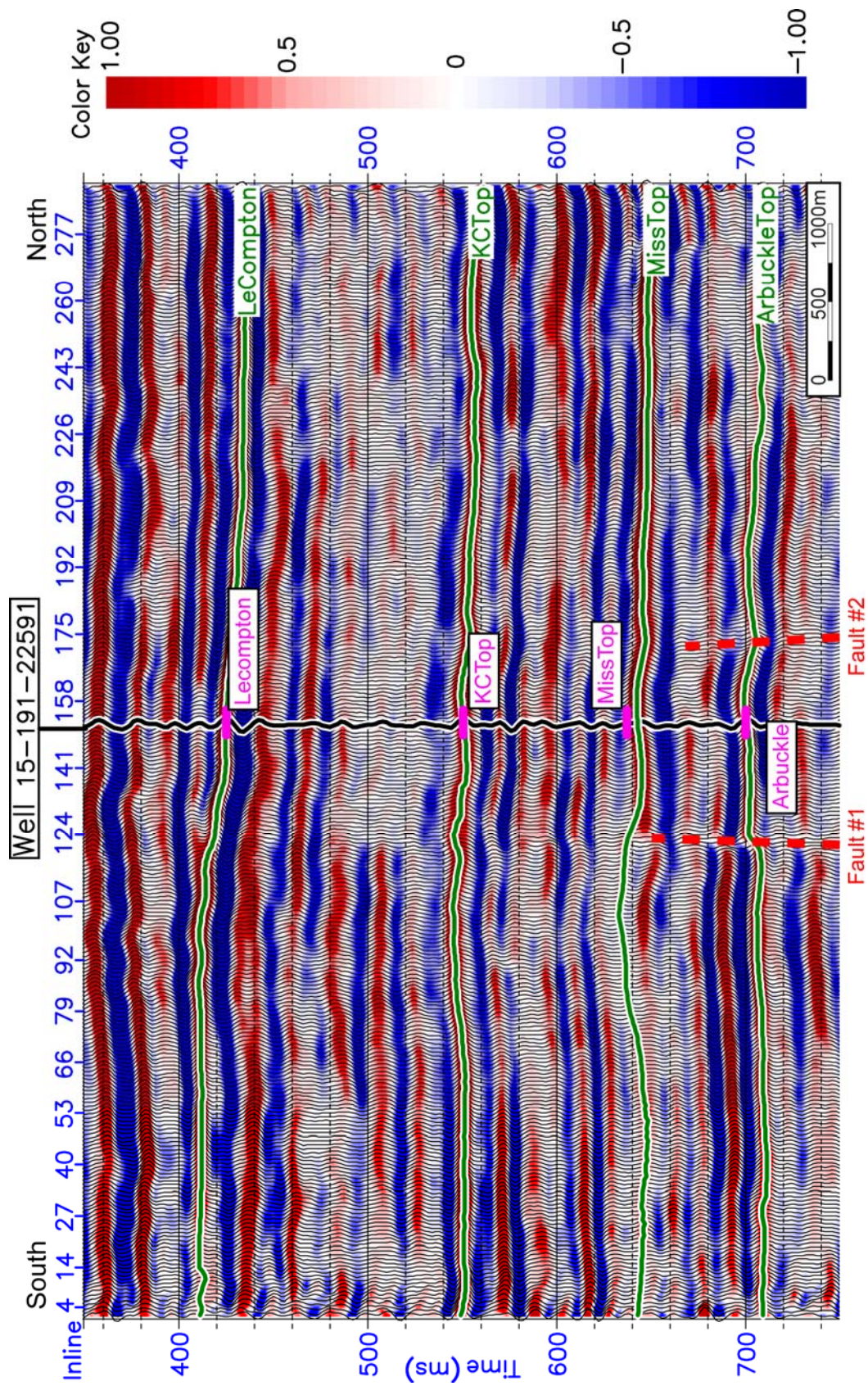


Figure 4.12. Crossline #158 with the overlain synthetic seismic trace generated at well #15-191-22591 and interpreted seismic horizons corresponding to the tops of the LeCompton Limestone, the Kansas-City Group, the Mississippian System and the Arbuckle Group (SEG normal polarity). Line location is shown in Figure 4.7.

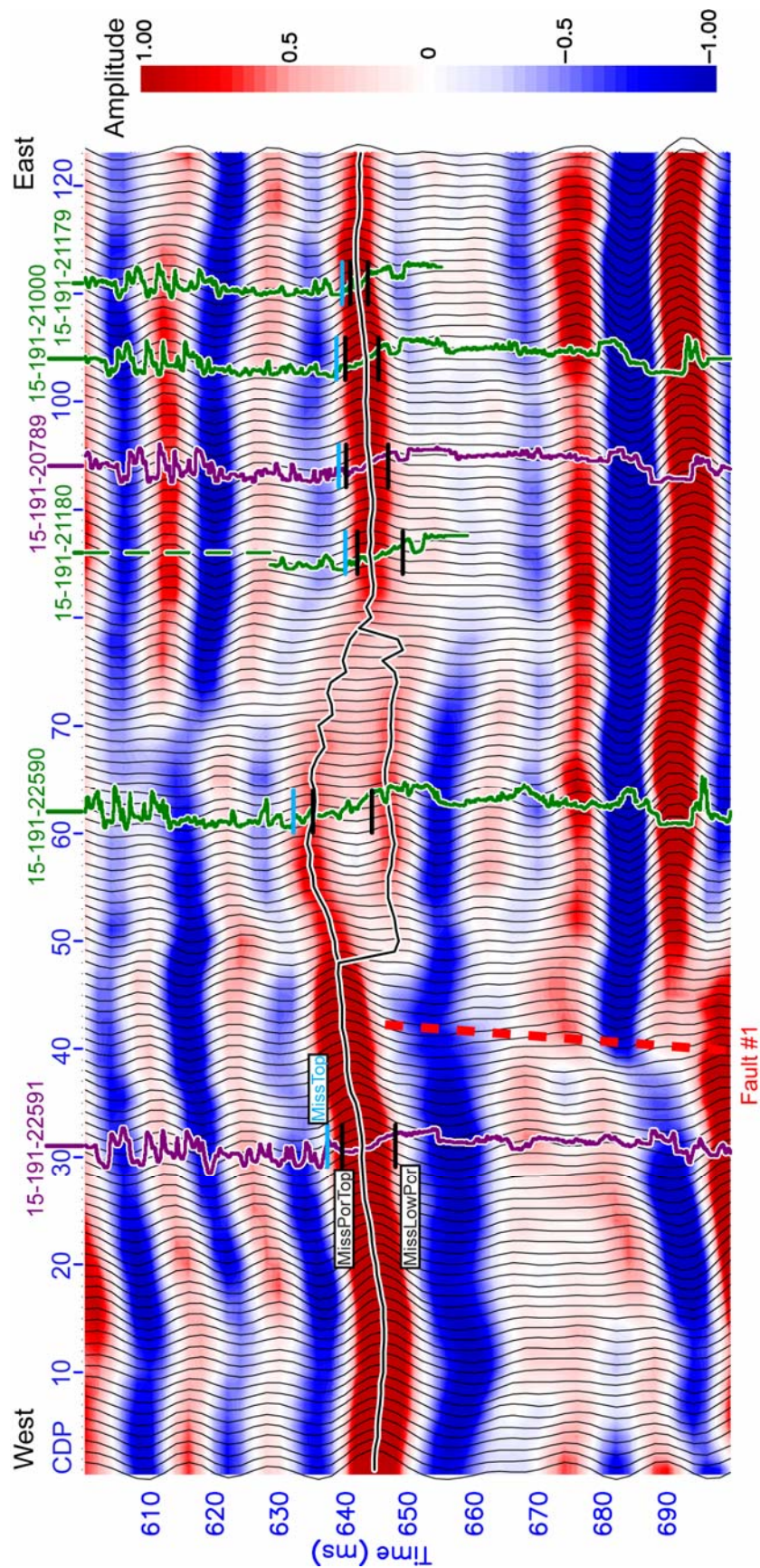


Figure 4.13. Arbitrary seismic line #1 (SEG normal polarity) with the overlain sonic (purple) and pseudo-sonic (green) log curves at the well locations. The interpreted seismic horizons represent the reflection from the Mississippian chert reservoir with double reflector developed in the middle of this arbitrary line. Well tops shown on the well curves are MissTop (light blue), MissPorTop and MissLowPor (black). Arbitrary line location is shown in Figure 4.14.

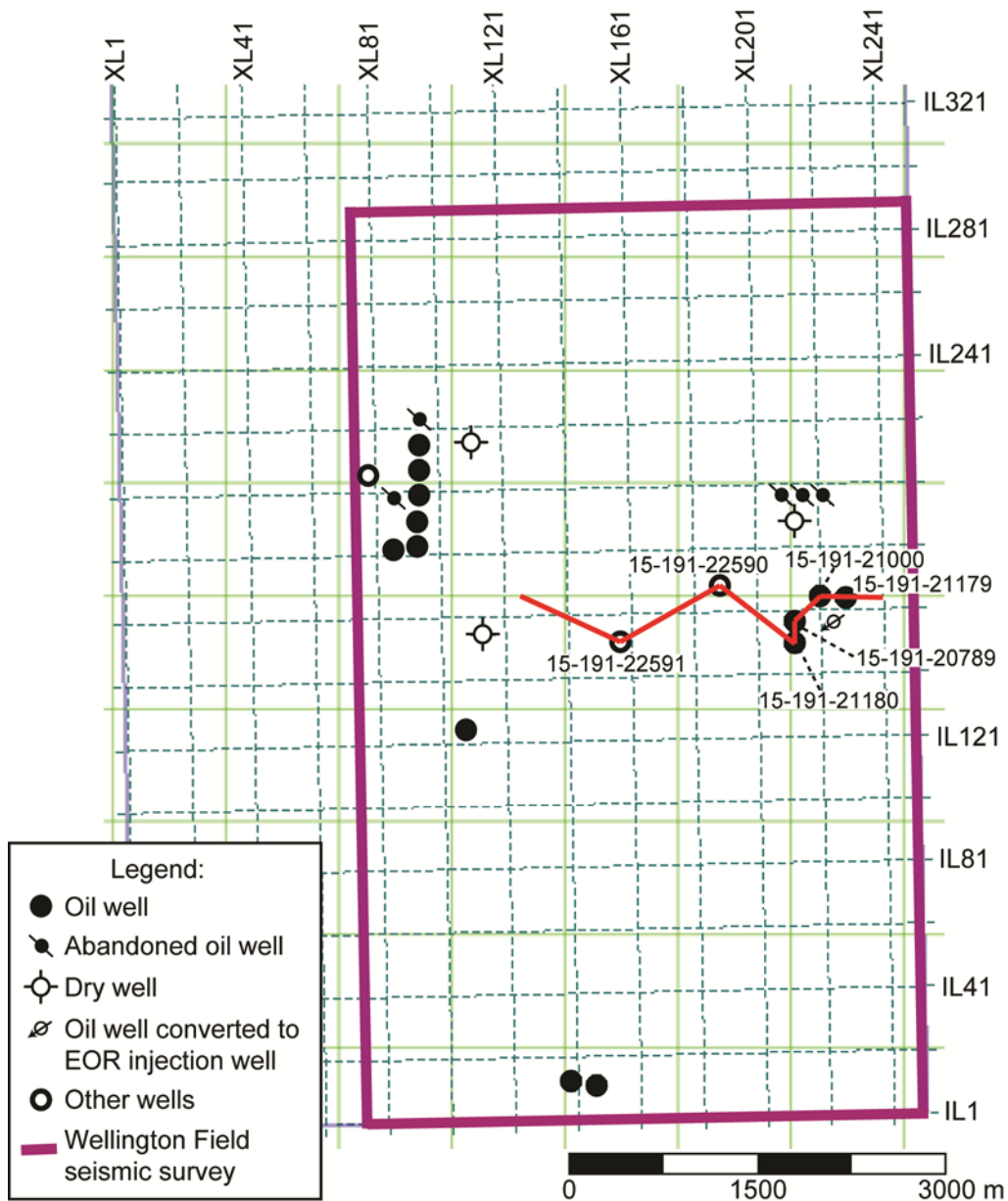


Figure 4.14. Seismic basemap with the arbitrary seismic line shown in Figure 4.13. Well names are shown only for those wells that are located along the arbitrary line path.

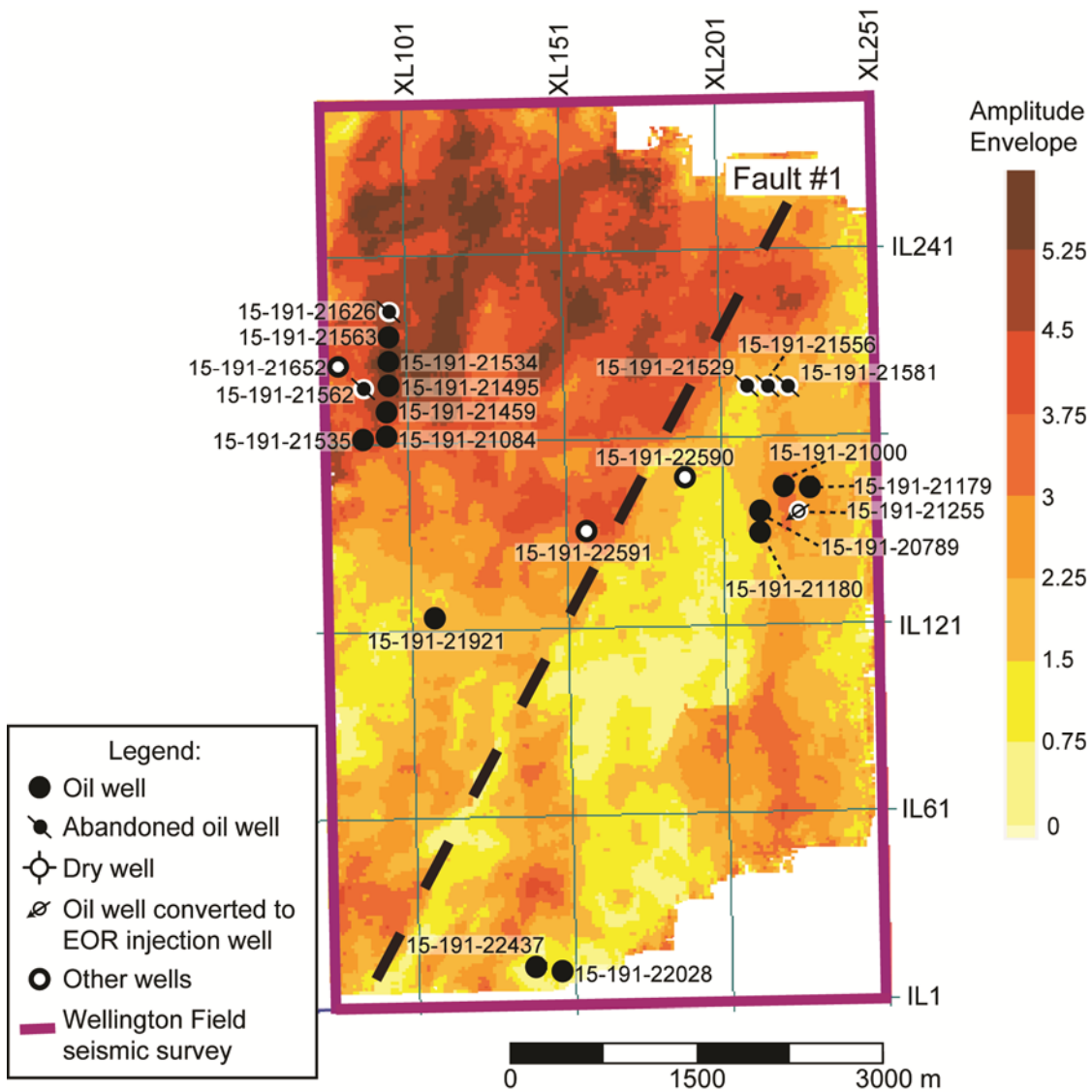


Figure 4.15. Amplitude envelope map of the Mississippian reflection, labeled as MissTop in Figures 4.11-4.13. Well locations are shown only for those wells which have any type of porosity logs and penetrate the reservoir base.

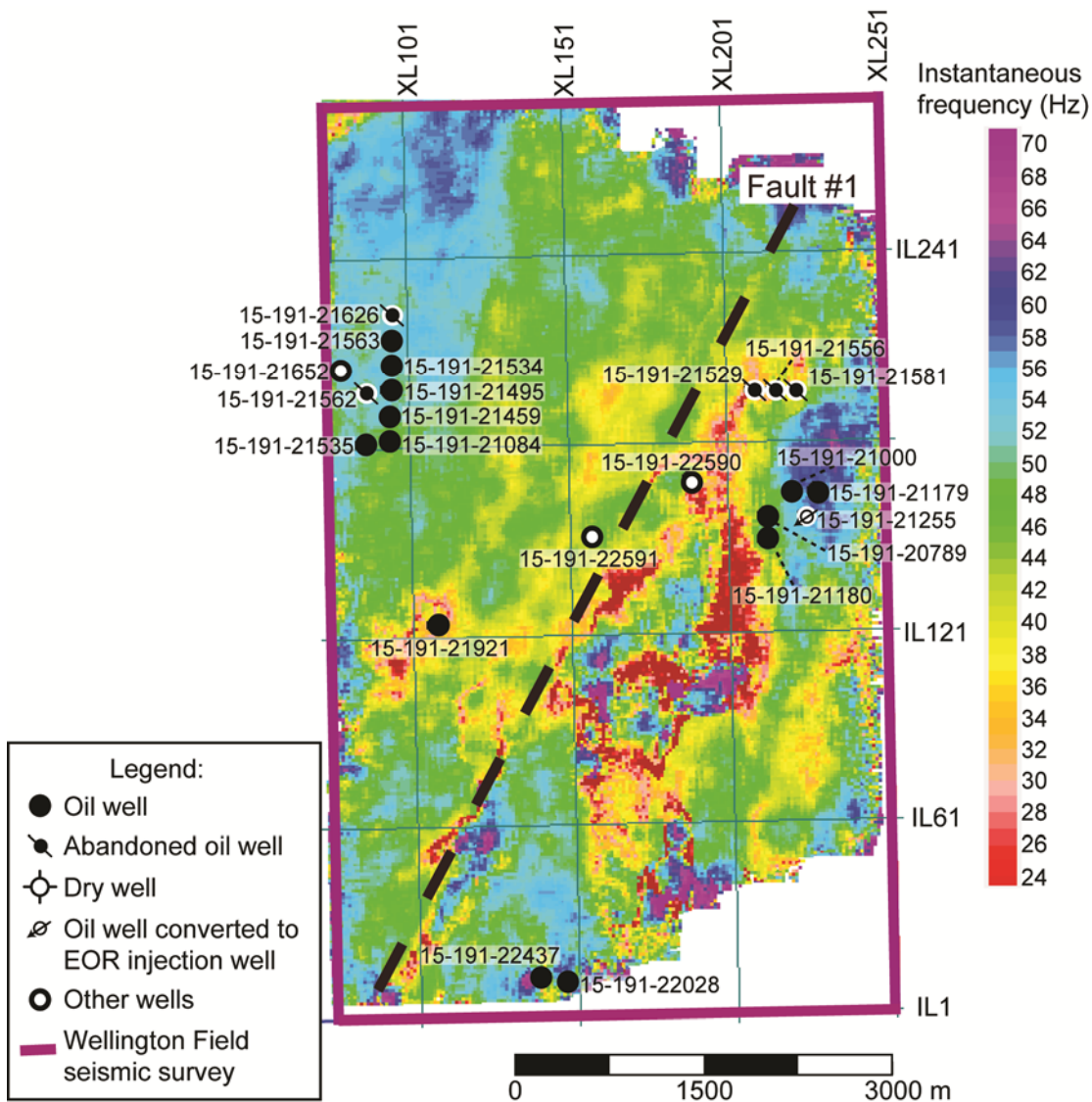


Figure 4.16. Instantaneous frequency map of the Mississippian reflection, labeled as MissTop in Figures 4.11-4.13. Well locations are shown only for those wells which have any type of porosity logs and penetrate the reservoir base.

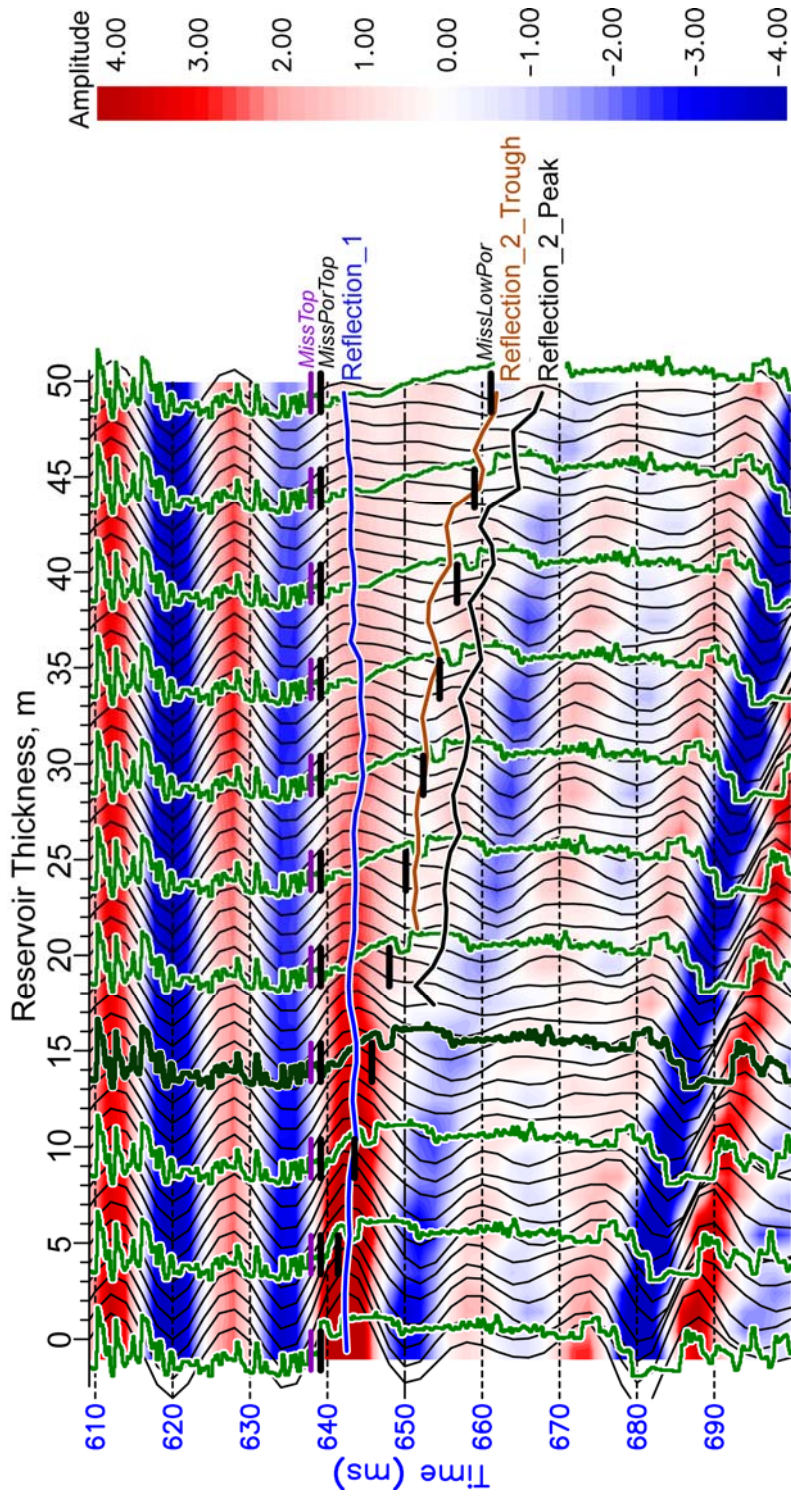


Figure 4.17. Synthetic seismic section of the reservoir wedge model constructed at well #15-191-20789. Original sonic log is shown in dark green (corresponds to reservoir thickness of 15 m). Synthetic sonic logs calculated by stretching and squeezing the original log within the Mississippian reservoir are shown in light green for every 5th trace. Well top shown in purple – MissTop, the top of the reworked Mississippian chert; well tops shown in black – MissPorTop and MissLowPor, the top and the base of the chert reservoir. The interpreted reflections are discussed in the text.

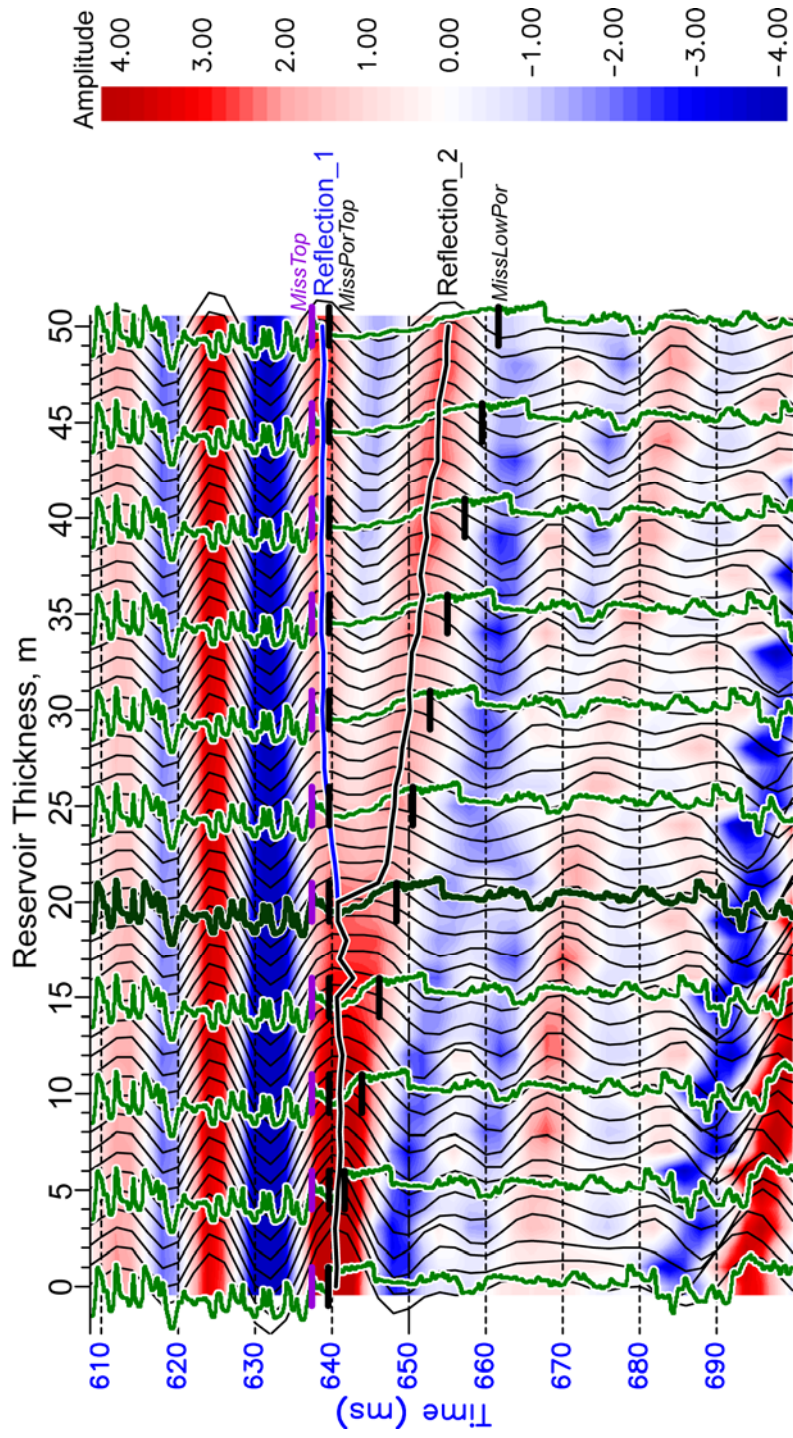


Figure 4.18. Synthetic seismic section of the reservoir wedge model constructed at well #15-191-22591. Original sonic log is shown in dark green (corresponds to reservoir thickness of 20 m). Synthetic sonic logs calculated by stretching and squeezing the original log within the Mississippian reservoir are shown in light green for every 5th trace. Well top shown in purple – MissTop, the top of the reworked Mississippian chert; well tops shown in black – MissPorTop and MissLowPor, the top and the base of the chert reservoir. The interpreted reflections are discussed in the text.

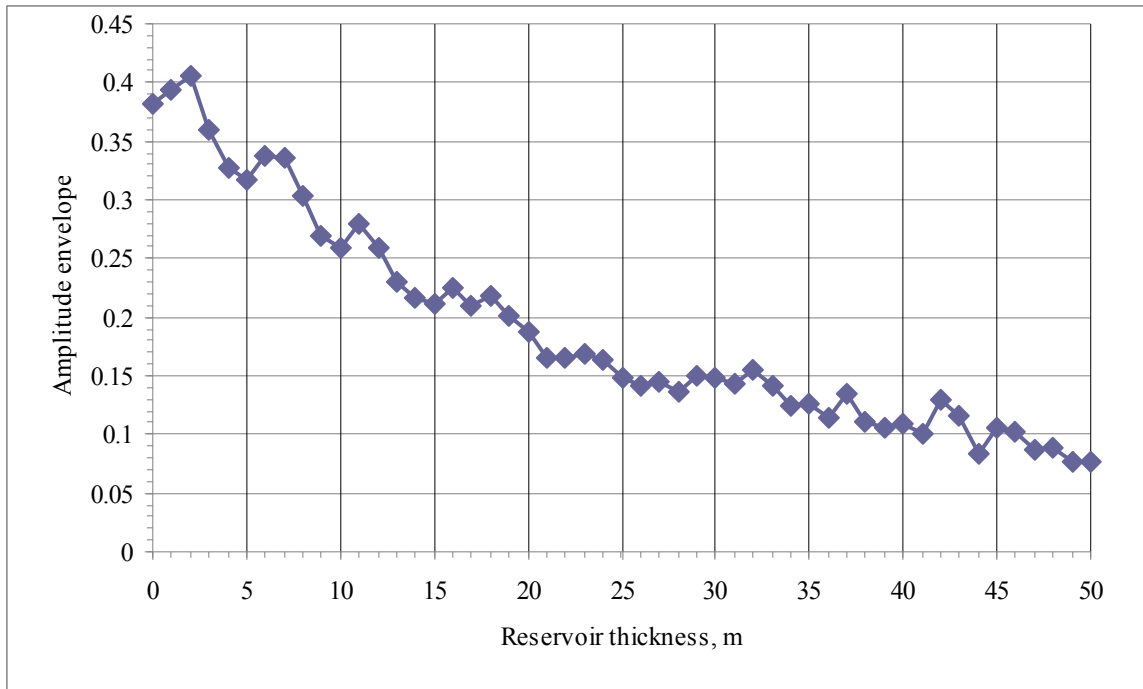


Figure 4.19. Crossplot of the amplitude envelope of Reflection_1 (interpreted on the synthetic seismic section built at well #15-191-20789, Figure 4.17) versus the reservoir thickness.

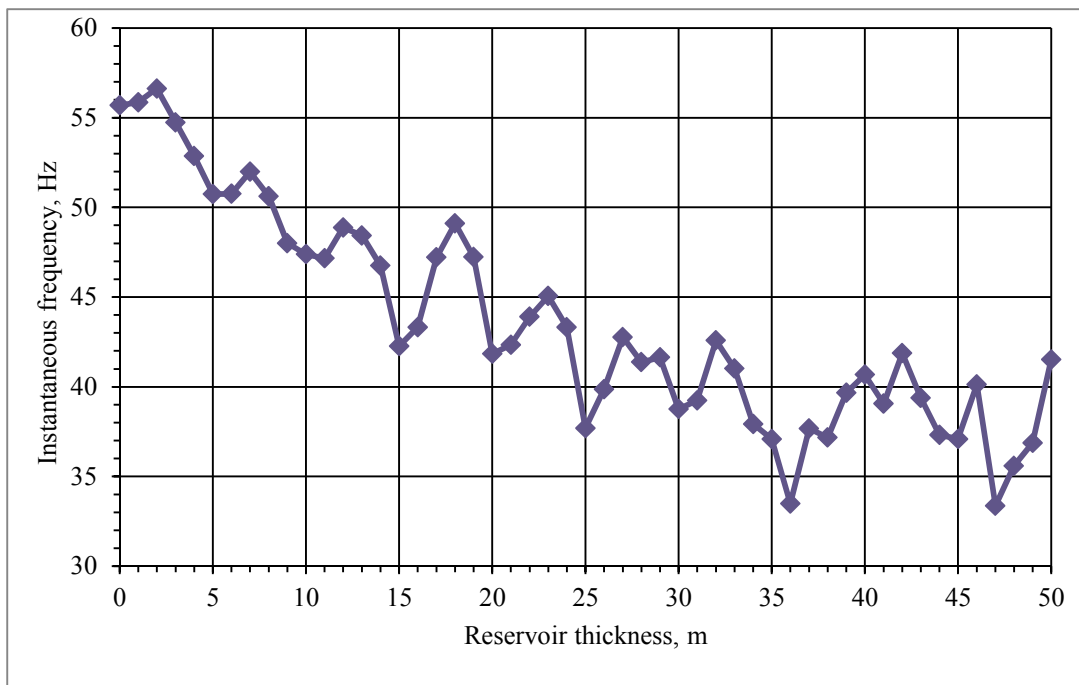


Figure 4.20. Crossplot of the RMS average instantaneous frequency within a 5ms window centered at Reflection_1 (interpreted on the synthetic seismic section built at well #15-191-20789, Figure 4.17) versus the reservoir thickness.

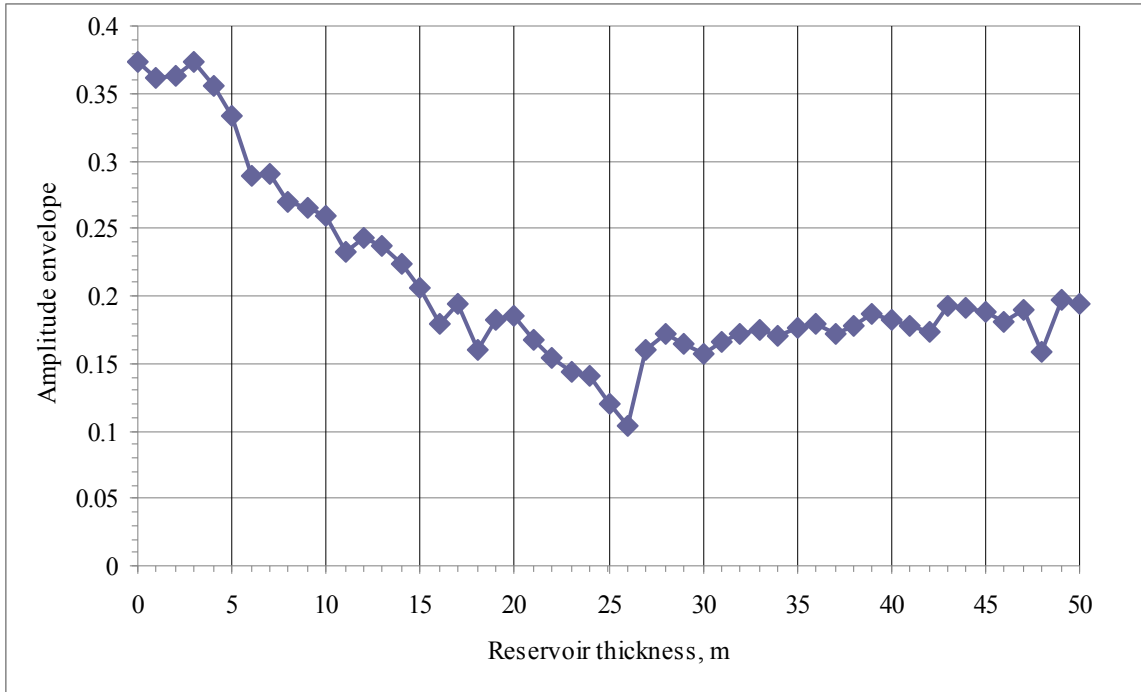


Figure 4.21. Crossplot of the amplitude envelope of Reflection_1 (interpreted on the synthetic seismic section built at well #15-191-22591, Figure 4.18) versus the reservoir thickness.



Figure 4.22. Crossplot of the RMS average instantaneous frequency within a 5ms window centered at Reflection_1 (interpreted on the synthetic seismic section built at well #15-191-22591, Figure 4.18) versus the reservoir thickness.

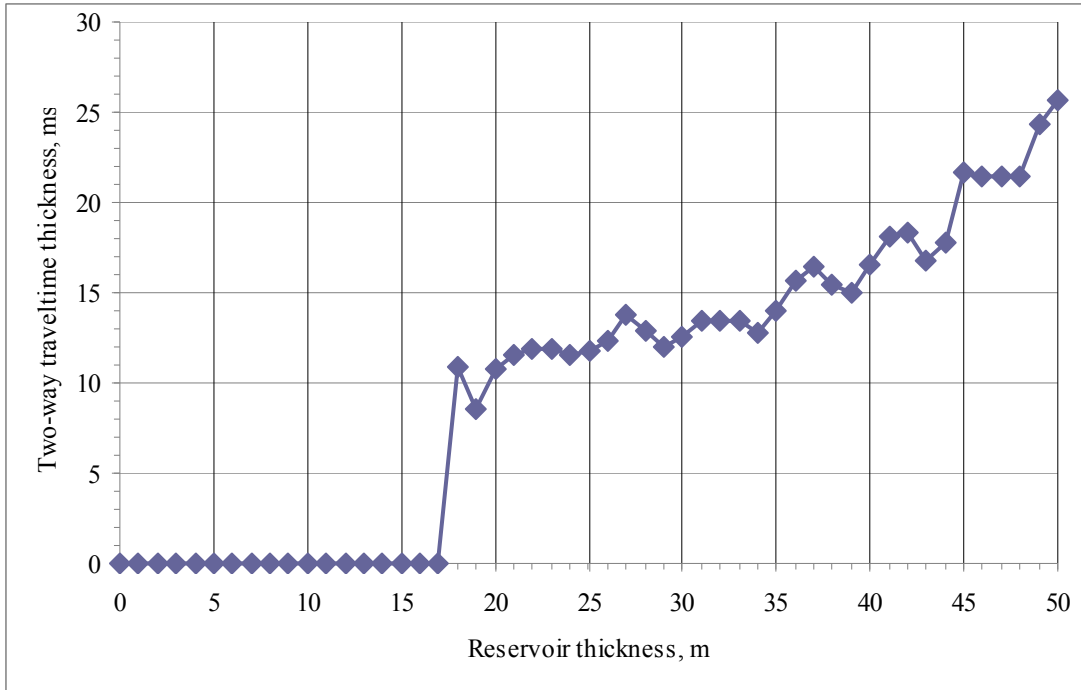


Figure 4.23. Crossplot of two-way travel time thickness between Reflection_1 and Reflection_2_peak (interpreted on the synthetic seismic section built at well #15-191-20789, Figure 4.17) versus the reservoir thickness. Below seismic resolution thickness is given the value of 0.

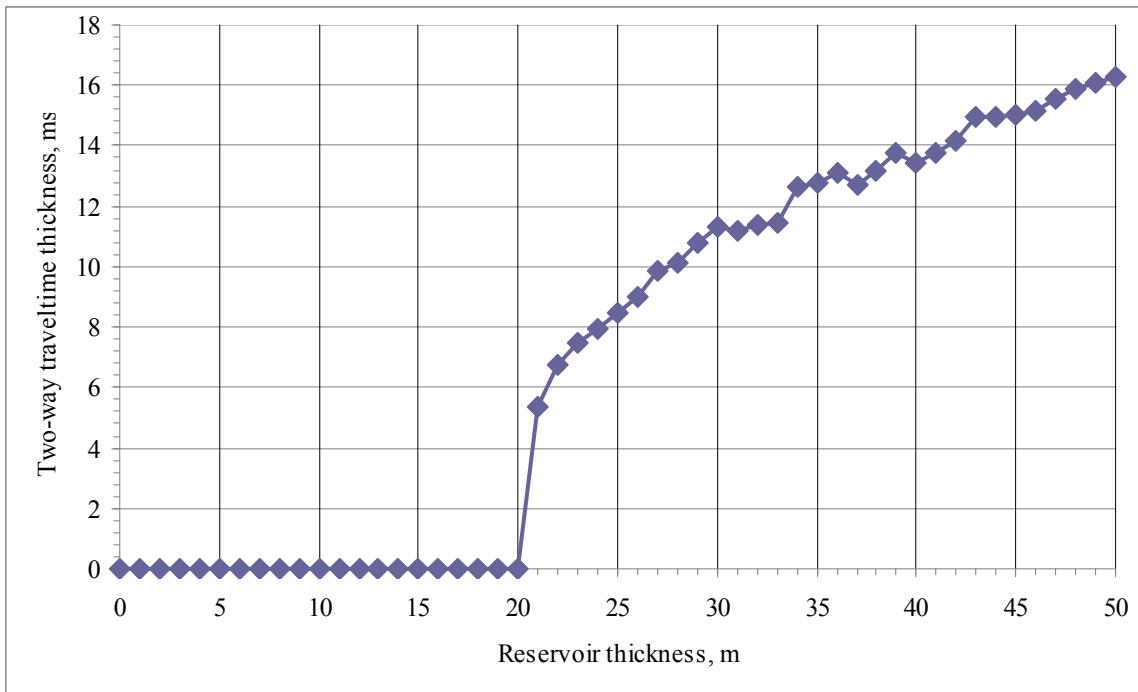


Figure 4.24. Crossplot of two-way travel time thickness between Reflection_1 and Reflection_2 (interpreted on the synthetic seismic section built at well #15-191-22591, Figure 4.18) versus the reservoir thickness. Below seismic resolution thickness is given the value of 0.

4.4: Post-stack Model-based Inversion

Acoustic impedance is one of the most useful and physically meaningful seismic attributes for porosity prediction (Russell, 1988). Most common approaches to calculate acoustic impedances of the subsurface from seismic data include bandlimited, sparse-spike, colored, and model-based inversion algorithms (Lindseth, 1979; Cooke and Schneider, 1983; Oldenburg et al., 1983; Lancaster and Whitcombe, 2000). The bandlimited inversion uses a simple recursive approach which treats a seismic trace as a true reflectivity sequence and totally ignores the wavelet (Lindseth, 1979). Therefore, the wavelet side lobes are taken as individual reflections by the bandlimited approach and the result has the same bandwidth as a seismic trace. The sparse-spike algorithm takes the wavelet into account, but looks only for the high-amplitude reflections and solves for the simplest possible impedance model that fits seismic data (Oldenburg et al., 1983). Therefore, the sparse-spike inversion does not recover thin layers, but works well for thick packages with high-impedance contrasts. The colored inversion represents a fast simple technique that calculates a single operator and convolves it with a seismic trace to calculate an inversion result (Lancaster and Whitcombe, 2000). The phase of this operator is -90° as it was noticed by the comparison of seismic data and inverted results. The amplitude spectrum of an operator is obtained by division of the amplitude spectrum of the earth's reflectivity, estimated from well log data, by the spectrum of seismic data. The colored inversion produces a result similar to the bandlimited and recursive approaches, but results in a higher frequency impedance model. The model-based inversion exploits the generalized linear inversion approach and when applied to real data commonly provides the most detailed impedance model of the subsurface (Cooke and Schneider, 1983; Russell and Hampson, 1991). In order to derive the impedance model and predict porosity distribution of the thin Mississippian reservoir at the Wellington

Field, I performed model-based inversion of the 3D PSTM seismic data using the Hampson-Russell STRATA software.

4.4.1: Initial Impedance Model

Due to the bandlimited nature of seismic data (10-128 Hz for the Wellington 3D PSTM data), the inversion process cannot estimate the low-frequency impedance trend (0-10 Hz) of large scale (long wavelength) subsurface features. The low-frequency impedance trend can be derived from well-log data and incorporated to the inversion process (Figure 4.25). Two wells, #15-191-20789 and 15-191-22591, had both density and sonic logs and were used to estimate the low-frequency impedance trend. First, the high-frequency model was constructed by interpolation and extrapolation of acoustic impedance values from the two well locations throughout the seismic volume (Figures 4.26-4.27). Model building was guided by 5 seismic horizons: 4 previously interpreted horizons (section 4.3.2, Figures 4.11-4.12) and an additional horizon, labeled as Horizon_1, specifically picked for the inversion process in order to honor the geometry of the pinching out Lecompton Limestone. The low-frequency impedance model was generated by low-pass filtering (0-10 Hz) the high-frequency model. The resulting low-frequency impedance model depicts the main geologic units, such as low-impedance Pennsylvanian shales (above the MissTop horizon) and high-impedance carbonates of Kansas-City Group, Mississippian System and Arbuckle Group (Figures 4.28-4.29). The low-frequency impedance model was used as the initial impedance model in the inversion process.

4.4.2: Model-based Inversion Analysis and Application

The model-based inversion exploits the generalized linear inversion approach as described by Cooke and Schneider (1983). The inversion process began with blocking the initial low-frequency impedance model into constant thicknesses intervals of 2 ms, which was the

temporal sampling interval of the seismic data. The blocky impedance model was convolved with the seismic wavelet shown in Figure 4.10 to create a synthetic seismic volume. The modeled and actual seismic traces were compared and their differences were used to update the initial impedance model at each point of the seismic grid in order to compensate for those differences. The updated impedance model was used as the initial model for the next iteration of generating synthetic seismic traces and compared to the actual data.

The results of the inversion are evaluated by comparing actual and estimated impedances as well as actual and modeled seismic traces at two well locations, #15-191-20789 and 15-191-22591 (Figures 4.30). The inversion process started with the low-frequency impedance model shown as black curves. In order to prevent the algorithm from deriving a potentially geologically incorrect answer, the solution was constrained to keep the inverted impedance values within the 100% range of the initial low-frequency impedance model. Ten iterations of generating synthetic seismic traces, their comparison to the actual seismic traces and updating the initial impedance model resulted in the predicted impedance traces shown as red curves. Additional iterations resulted in no significant improvement and increased the computation time. These inverted impedance curves (red) show a good match with the original impedance log curves (blue) within the interval between the tops of the Lecompton Limestone and the Arbuckle Group (yellow horizontal lines). Synthetic seismic traces (red; repeated 5 times) were generated by the convolution of the seismic wavelet with the inverted impedance logs and showed high correlation (greater than 0.90) with the actual seismic traces (black; repeated 5 times) at the well locations. Figure 4.31 presents the crossplot between the inverted and actual impedance values at both wells with the line of perfect correlation shown in red. Supported by the good agreement between modeled and actual data at the two well locations, the model-based inversion was

applied to the seismic data in order to calculate the acoustic impedance model of the subsurface (Figures 4.32-4.33). The inverted impedance depicts the main geologic units, such as pinching out of the Lecompton Limestone, low-impedance Pennsylvanian shales (above the MissTop horizon) and high-impedance carbonates of Kansas-City Group, Mississippian System and Arbuckle Group, and provides the information on lateral variability within the units.

Finally, I analyzed the inversion result within the Mississippian reservoir at twelve wells tied to the seismic data. Locations of those wells are shown in Figure 4.1: two of these wells, #15-191-20789 and 15-191-22591, had original sonic logs and the other ten wells had pseudo-sonic logs calculated as described in section 4.2. All wells had original density logs. The initial low-frequency impedance model, the inverted impedance traces and the original impedance well logs are shown as black, red and blue curves respectively (Figure 4.34). Well tops shown as black horizontal lines correspond to MissTop (upper line), MissPorTop (middle line) and MissLowPor (lower line). The inverted impedance curves (red) show an overall good agreement with the original impedance logs (blue) for the Mississippian reservoir within the analysis window shown with yellow horizontal lines. The good agreement is supported by the crossplot of the inverted and actual impedance values at these well locations (Figure 4.35). However, Figure 4.35 reveals several points shifted from the line of perfect correlation in the upper right part of the crossplot. These outliers represent underestimation of high impedances near the reservoir top as visually evident for wells #15-191-21556 and 15-191-22590 in Figure 4.34.

4.4.3: Model-based Inversion of the Synthetic Wedge Models

The synthetic seismic sections calculated in section 4.3.4 at wells #15-191-20789 and 15-191-22591 (Figures 4.17 and 4.18) were inverted using the model-based approach in order to test the ability of the inversion method to recover acoustic impedance in the reservoir characterized

by a gradational downward velocity and density increase. The original sonic and density logs were used to build the high-frequency impedance models of the wedges. Two seismic horizons, Reflection_1 and Reflection_2_peak shown in Figure 4.17, guided the extrapolation of the impedance values from the trace corresponding to 15 m wedge thickness through the synthetic seismic section at the well #15-191-20789. The low-pass filter, 0-10 Hz, was applied to the high-frequency impedance model to get the low-frequency one. This low-frequency impedance model served as the initial impedance model in the inversion process. The inversion result was analyzed at each trace location, because the synthetic wedge model had both density and sonic logs at each trace. Figures 4.36 and 4.37 show the comparison of the inverted impedance traces (red) and the original impedance logs (blue) for the wedge thickness ranges of 0-5, 10, 15-20, 25, 30, 35, 40, 45 and 50 m. Figure 4.38 shows the crossplot of the RMS inversion error calculated within the reservoir interval versus the wedge thickness.

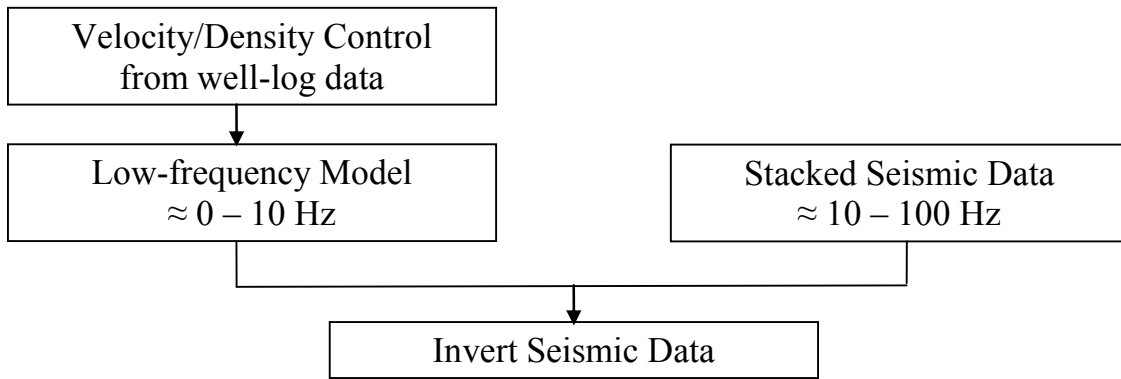


Figure 4.25. A general workflow for post-stack seismic inversion (Russell, 1988).

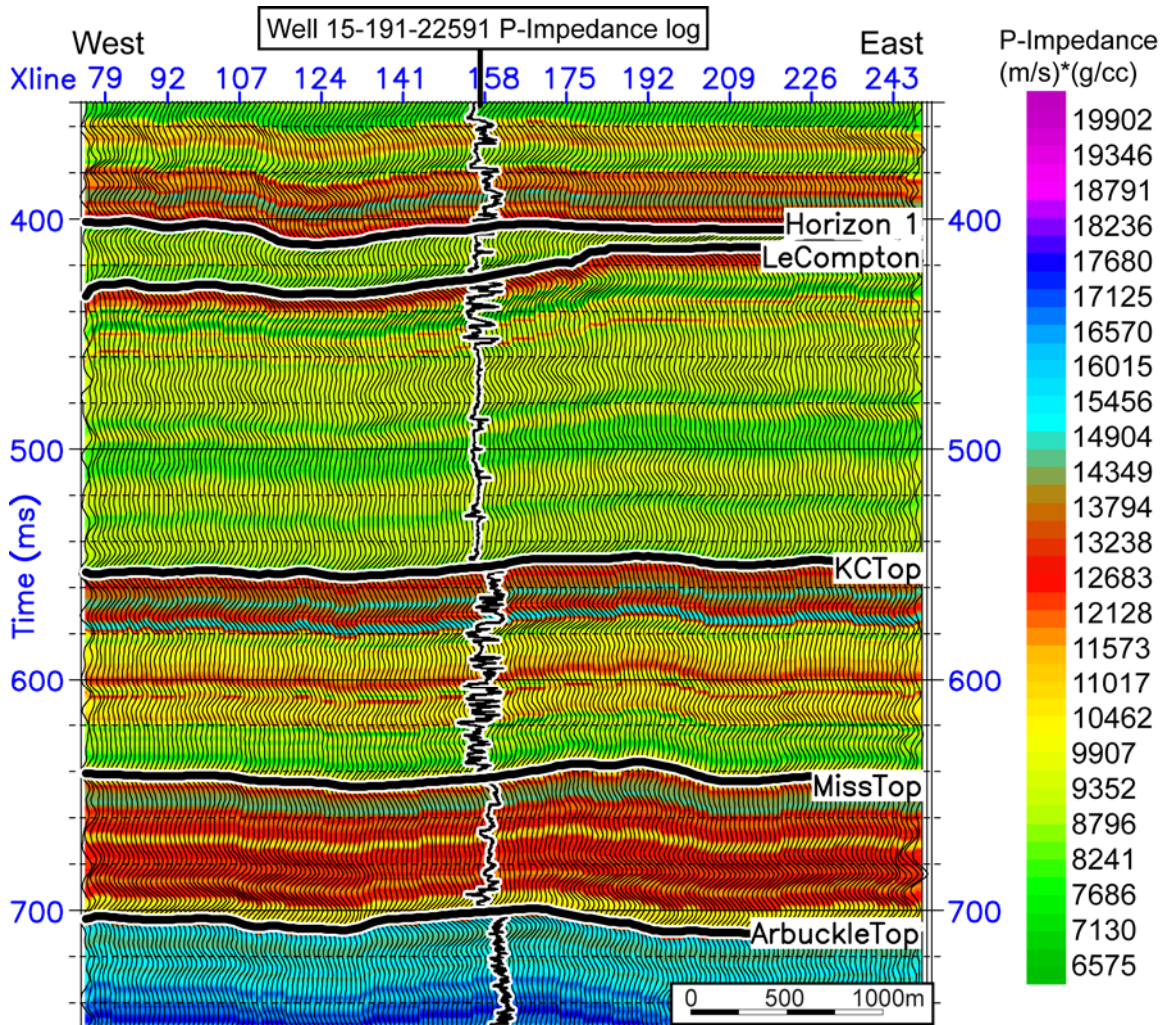


Figure 4.26. High-frequency impedance model along inline #152 built by the extrapolation of the computed impedance log at well #15-191-22591 using 5 interpreted seismic horizons. Traces represent the seismic data (SEG reversed polarity). Line location is shown in Figure 4.7.

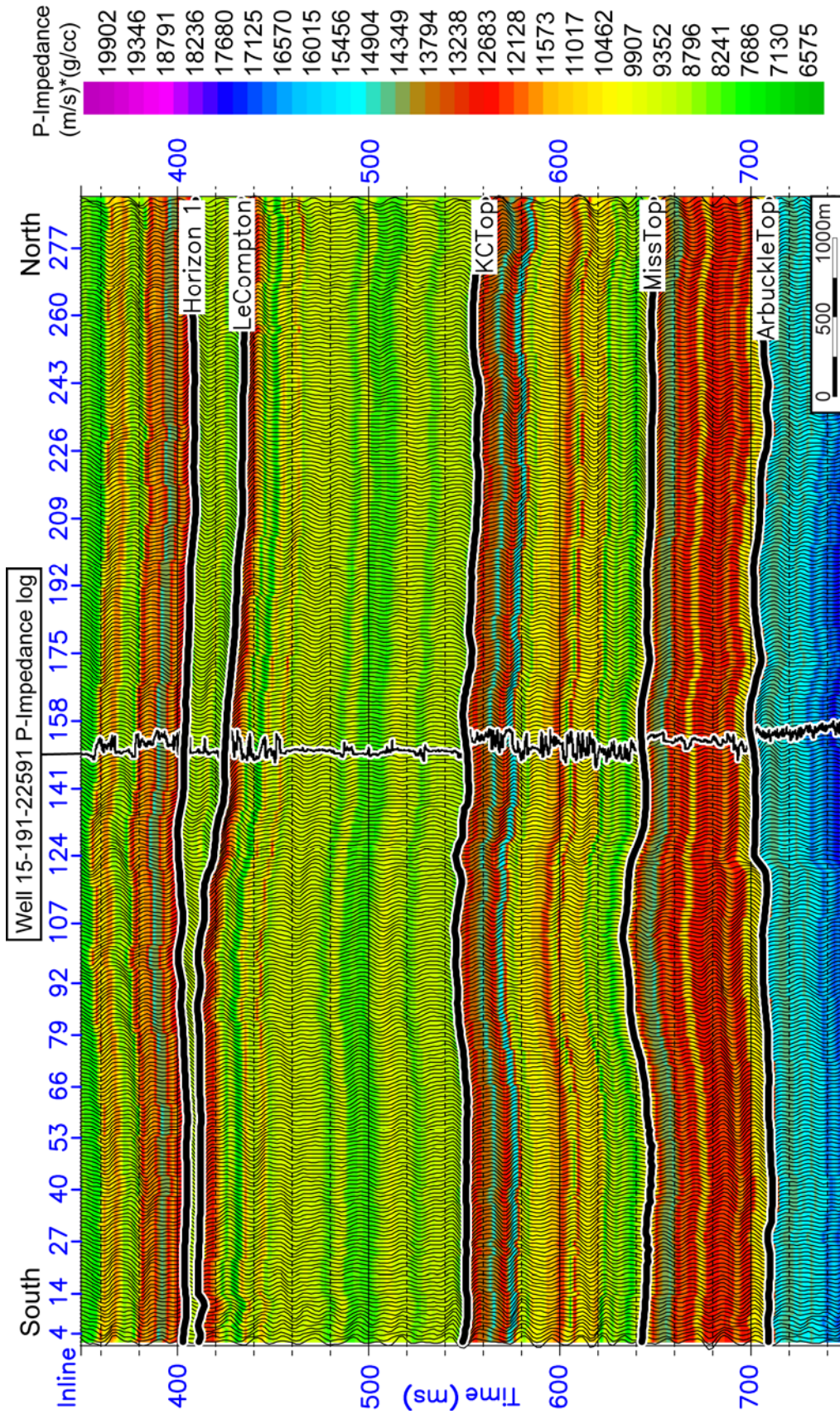


Figure 4.27. High-frequency impedance model along crossline #158 built by the extrapolation of the computed impedance log at well #15-191-22591 using 5 interpreted seismic horizons. Traces represent the seismic data (SEG reversed polarity). Line location is shown in Figure 4.7.

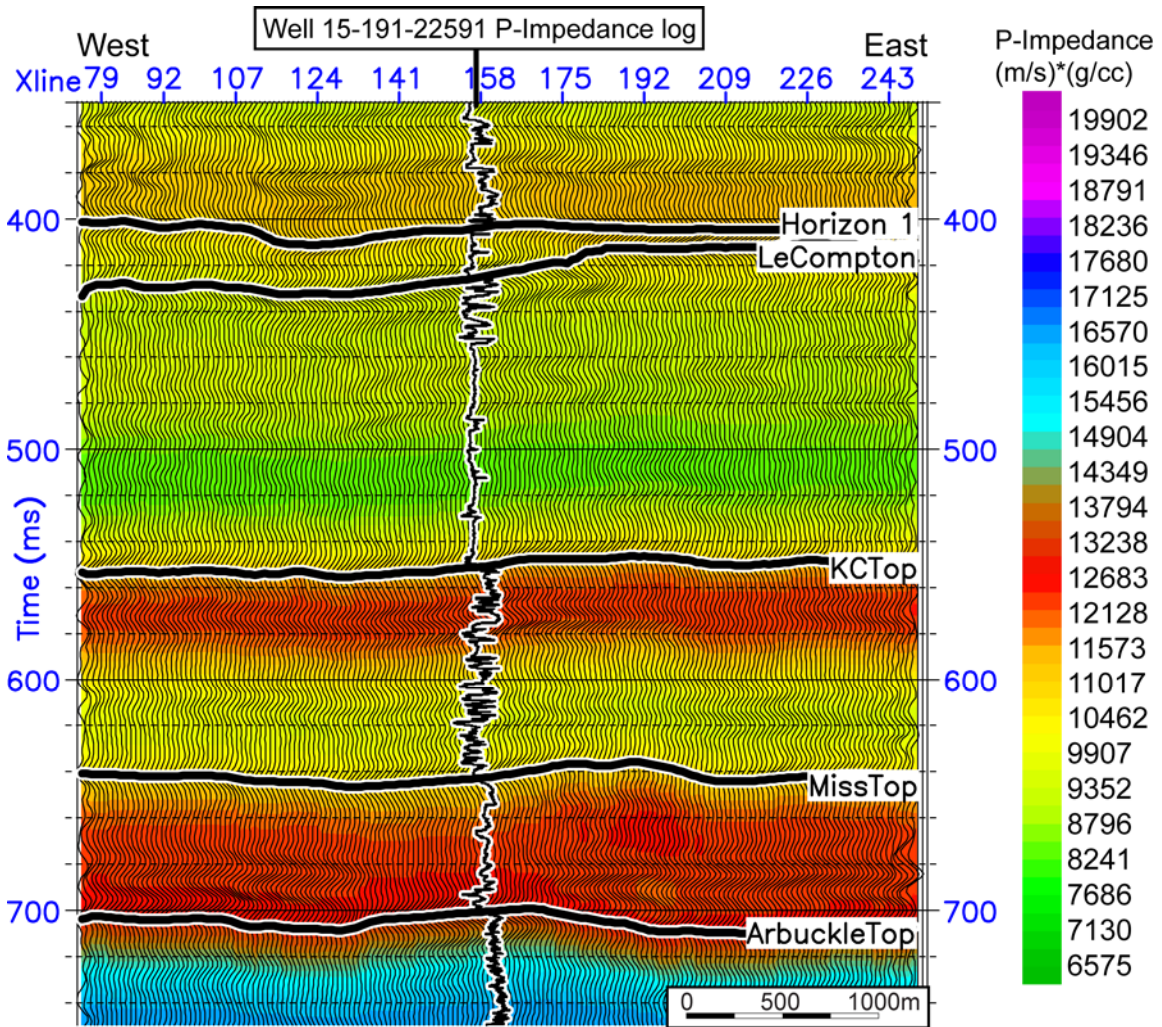


Figure 4.28. Low-frequency impedance model along inline #152 calculated by low-pass filtering of the model shown in Figure 4.26. Traces represent the seismic data (SEG reversed polarity). Line location is shown in Figure 4.7.

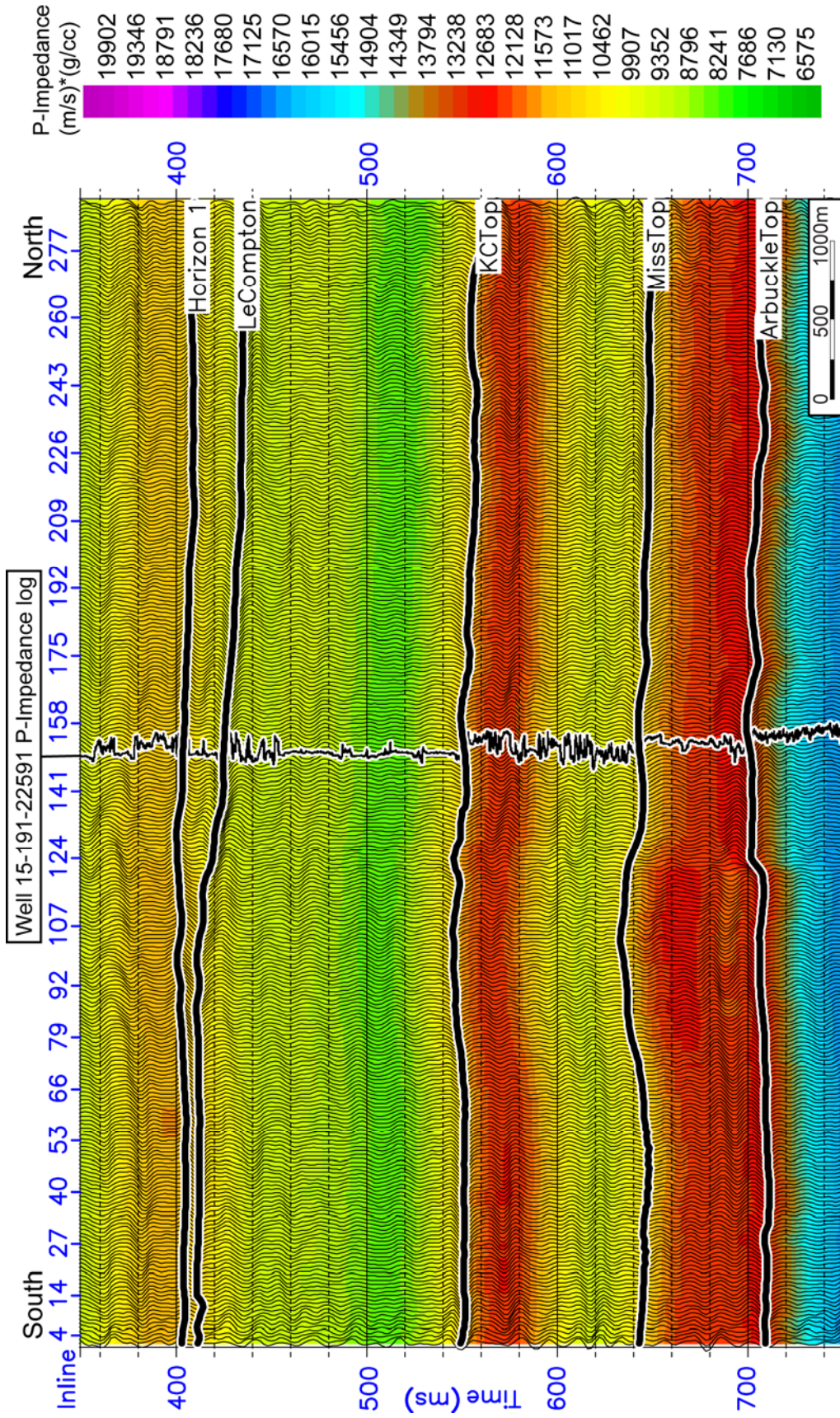


Figure 4.29. Low-frequency impedance model along crossline #158 calculated by low-pass filtering of the model shown in Figure 4.27. Traces represent the seismic data (SEG reversed polarity). Line location is shown in Figure 4.7.

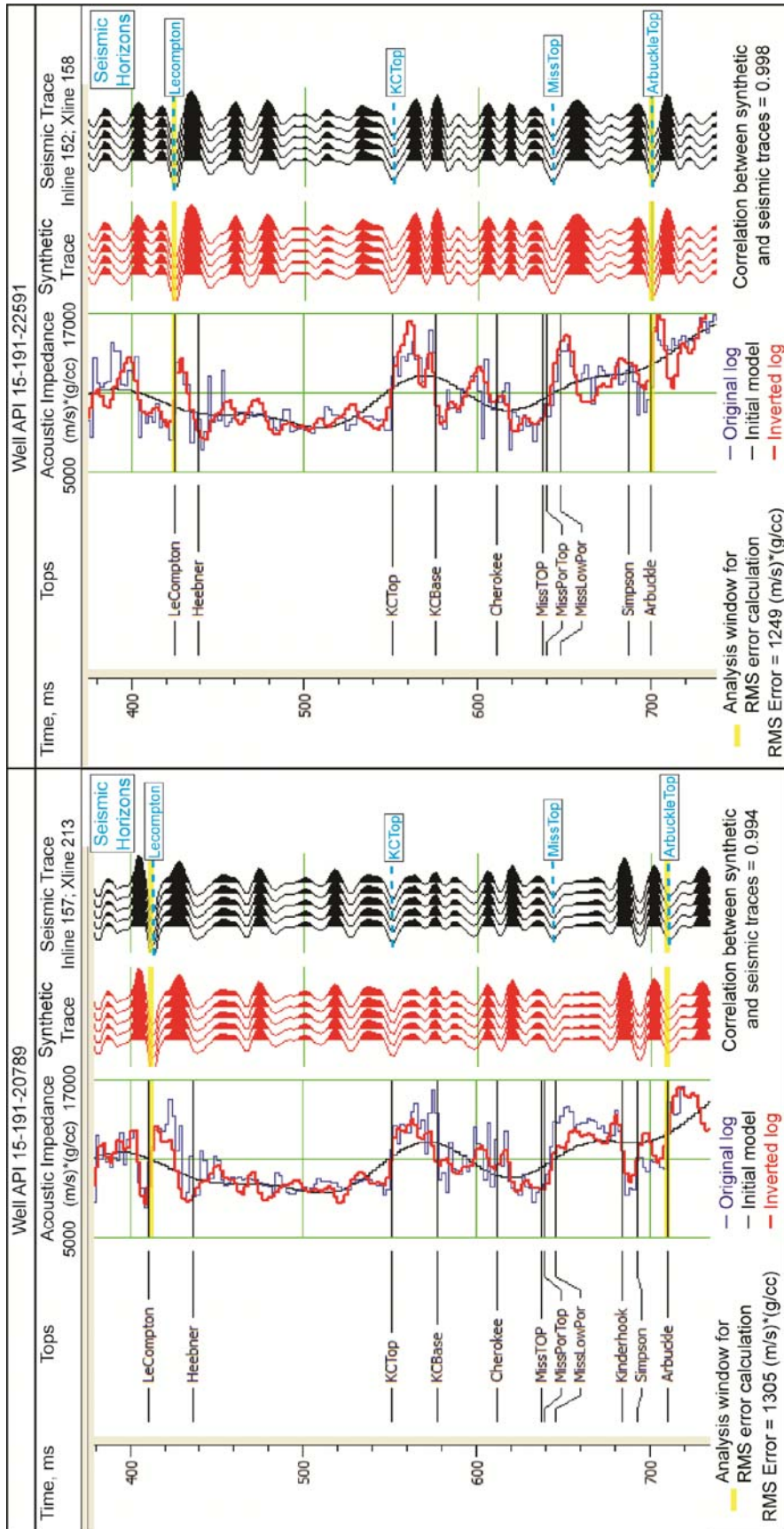


Figure 4.30. Analysis of model-based inversion at two well locations, #15-191-20789 (left) and 15-191-22591 (right). The inverted impedance traces (red) show a good match with the original impedance logs (blue) with the total RMS error of 1286 (m/s)*(g/cc) within the analysis window (yellow horizontal lines). Synthetic seismic traces built by the convolution of the seismic wavelet shown in Figure 4.10 with the inverted impedance traces (red; repeated 5 times) show high correlation (greater than 0.90) with the actual seismic traces (black) at the well locations. Synthetic and seismic traces are displayed in SEG reversed polarity.

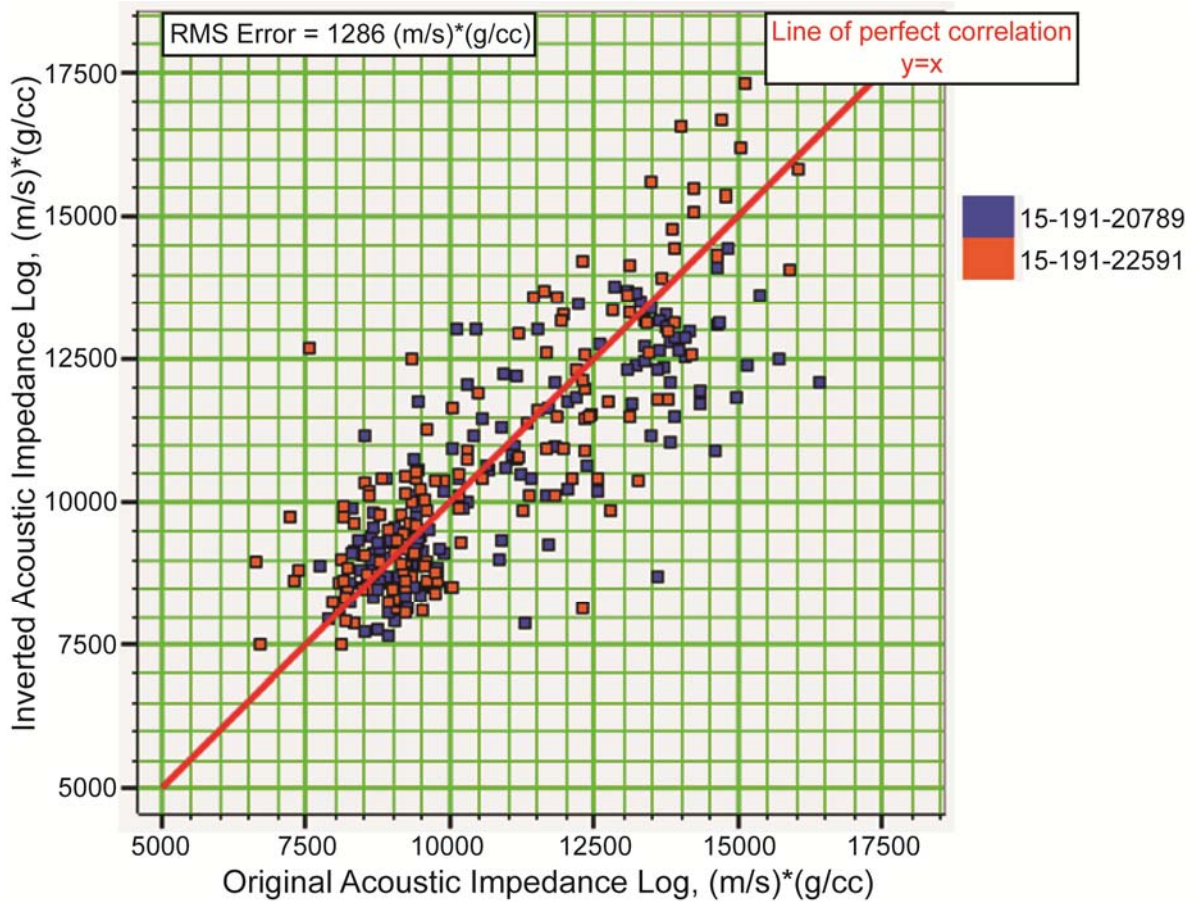


Figure 4.31. Crossplot of the inverted impedance versus the original impedance logs within the interval between the tops of the Lecompton Limestone and the Arbuckle Group (the analysis window shown with yellow horizontal lines in Figure 4.30) at two well locations, #15-191-20789 and 15-191-22591. The red line shows the line of perfect correlation between inverted and original impedance values. The total RMS error for two wells is 1286 (m/s)*(g/cc).

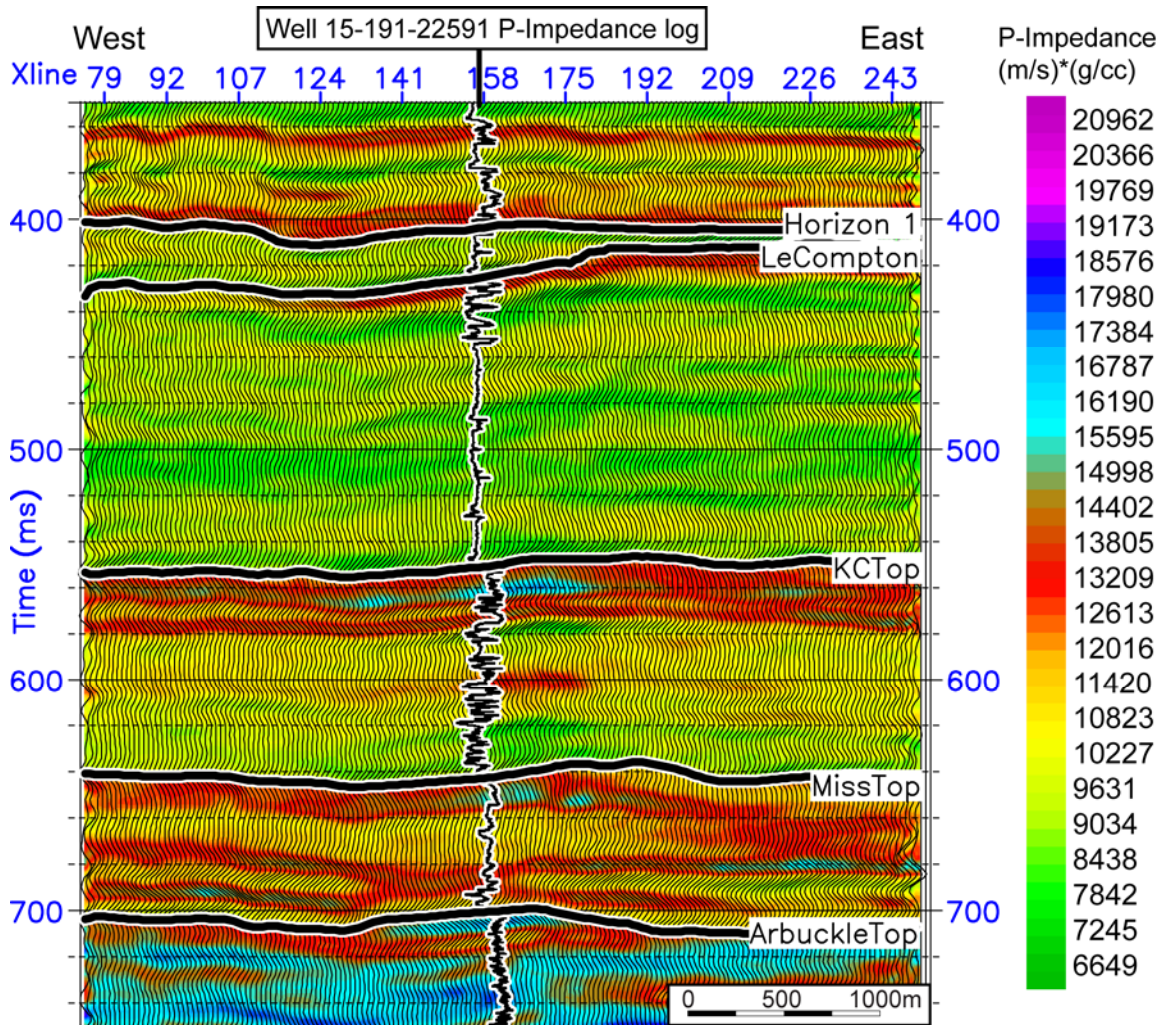


Figure 4.32. Model-based inverted impedance section along inline #152. Traces represent the seismic data (SEG reversed polarity). Line location is shown in Figure 4.7.

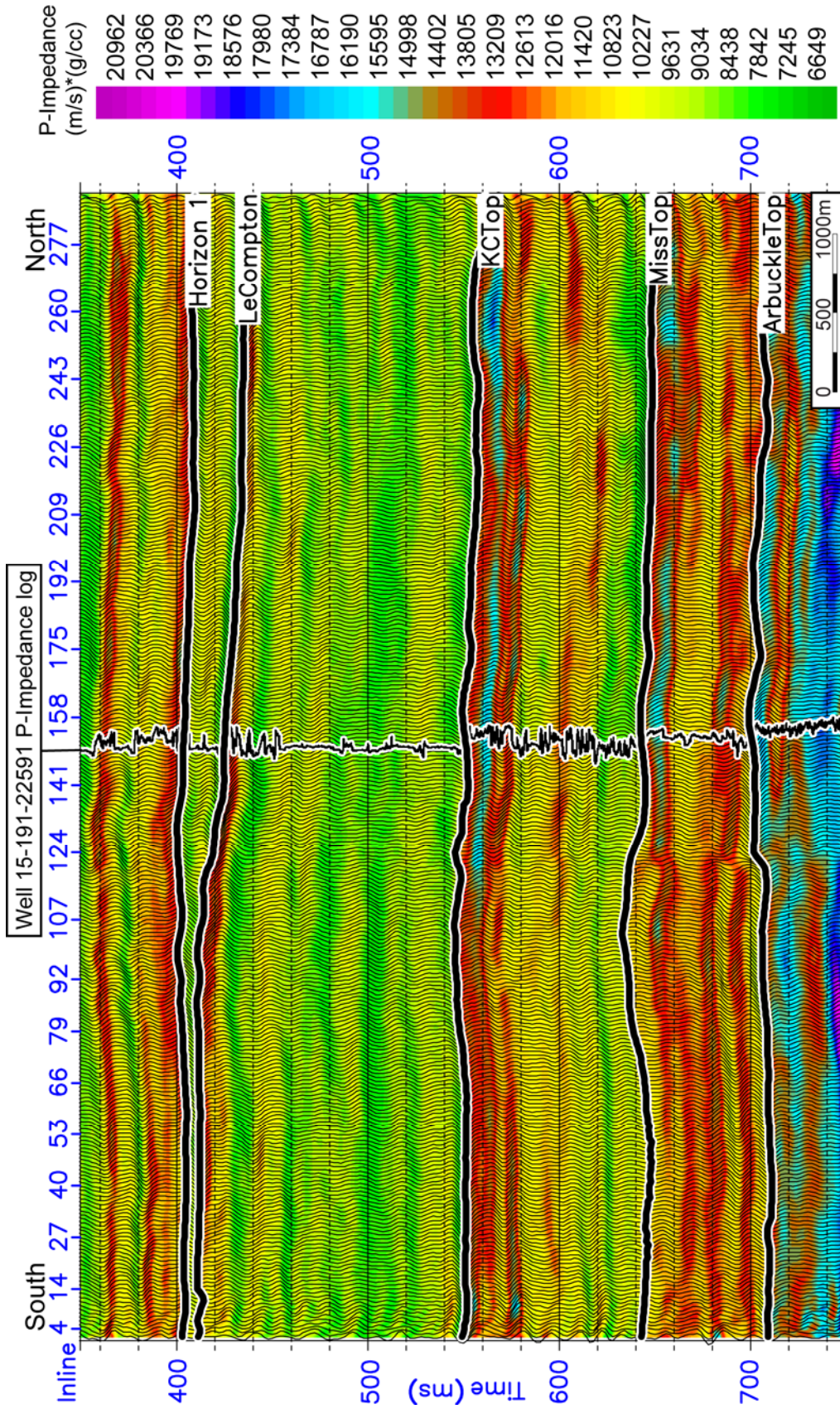


Figure 4.33. Model-based inverted impedance section along crossline #158. Traces represent the seismic data (SEG reversed polarity). Line location is shown in Figure 4.7.

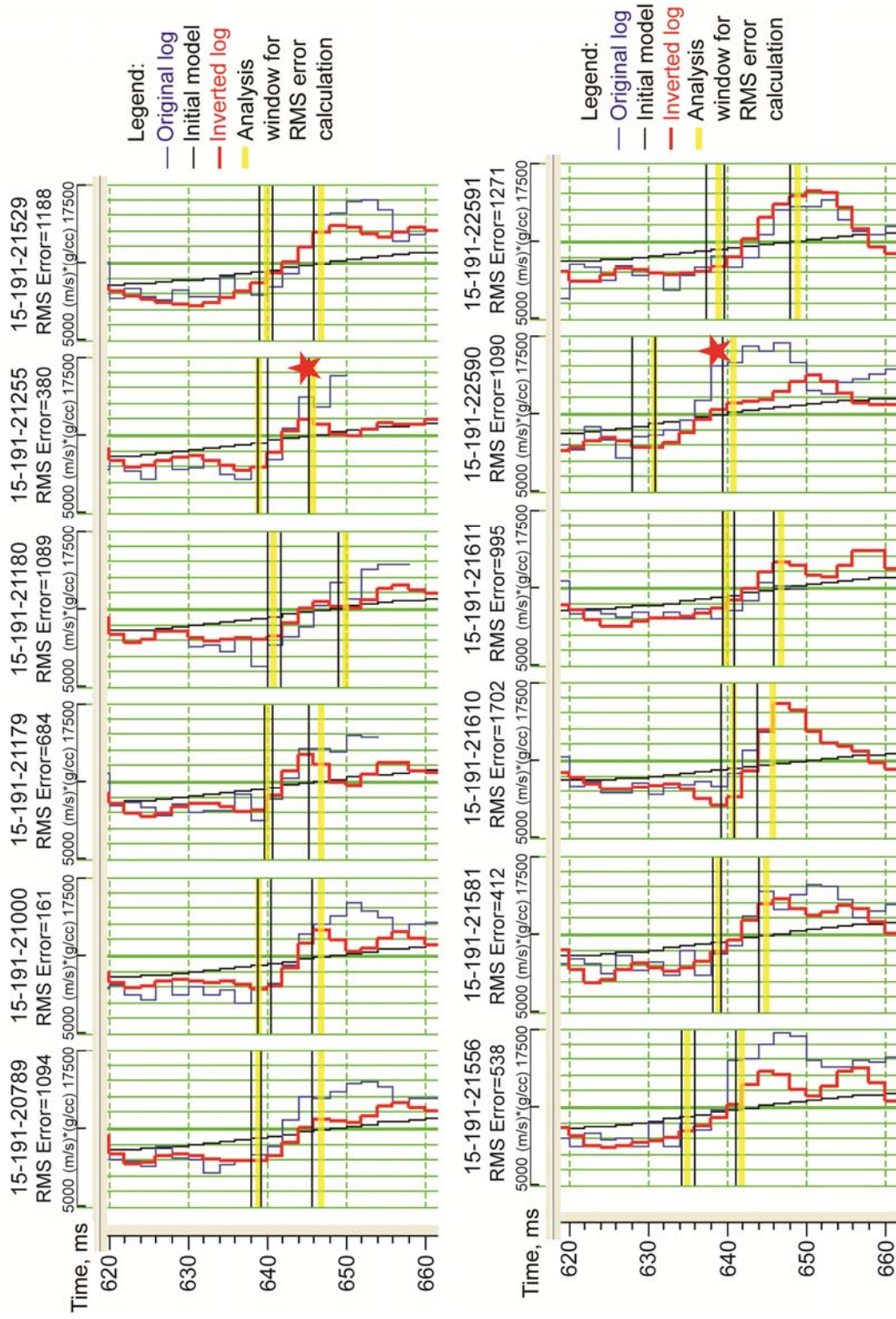


Figure 4.34. Analysis of the model-based inversion result within the Mississippian chert reservoir (shown by the yellow horizontal lines of the analysis window) at 12 well locations. The inverted impedance traces (red) show a good agreement with the original impedance logs (blue). The total RMS error for all wells is 982 (m/s)*(g/cc). Red stars show the underestimation of high impedances near the reservoir base as discussed in section 5.4.1 and shown in Figure 4.35.

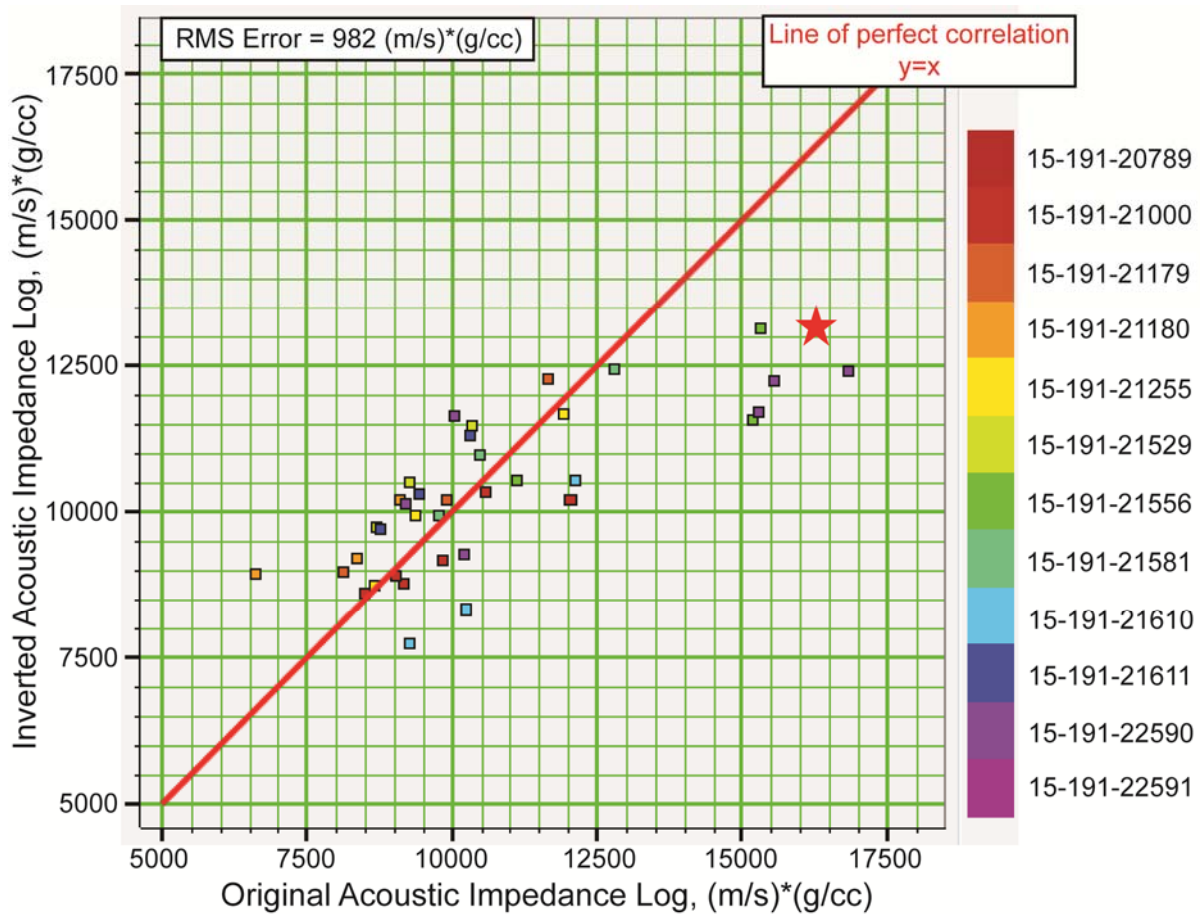


Figure 4.35. Crossplot of the inverted impedance versus the original impedance logs within the Mississippian chert reservoir (the analysis window shown with yellow horizontal lines in Figure 4.34) at twelve well locations. The red line shows the line of perfect correlation between inverted and original impedance values. The total RMS error for twelve wells is 982 (m/s)*(g/cc). Red star shows the underestimation of high impedances near the reservoir base as discussed in section 5.4.1 and shown in Figure 4.34.

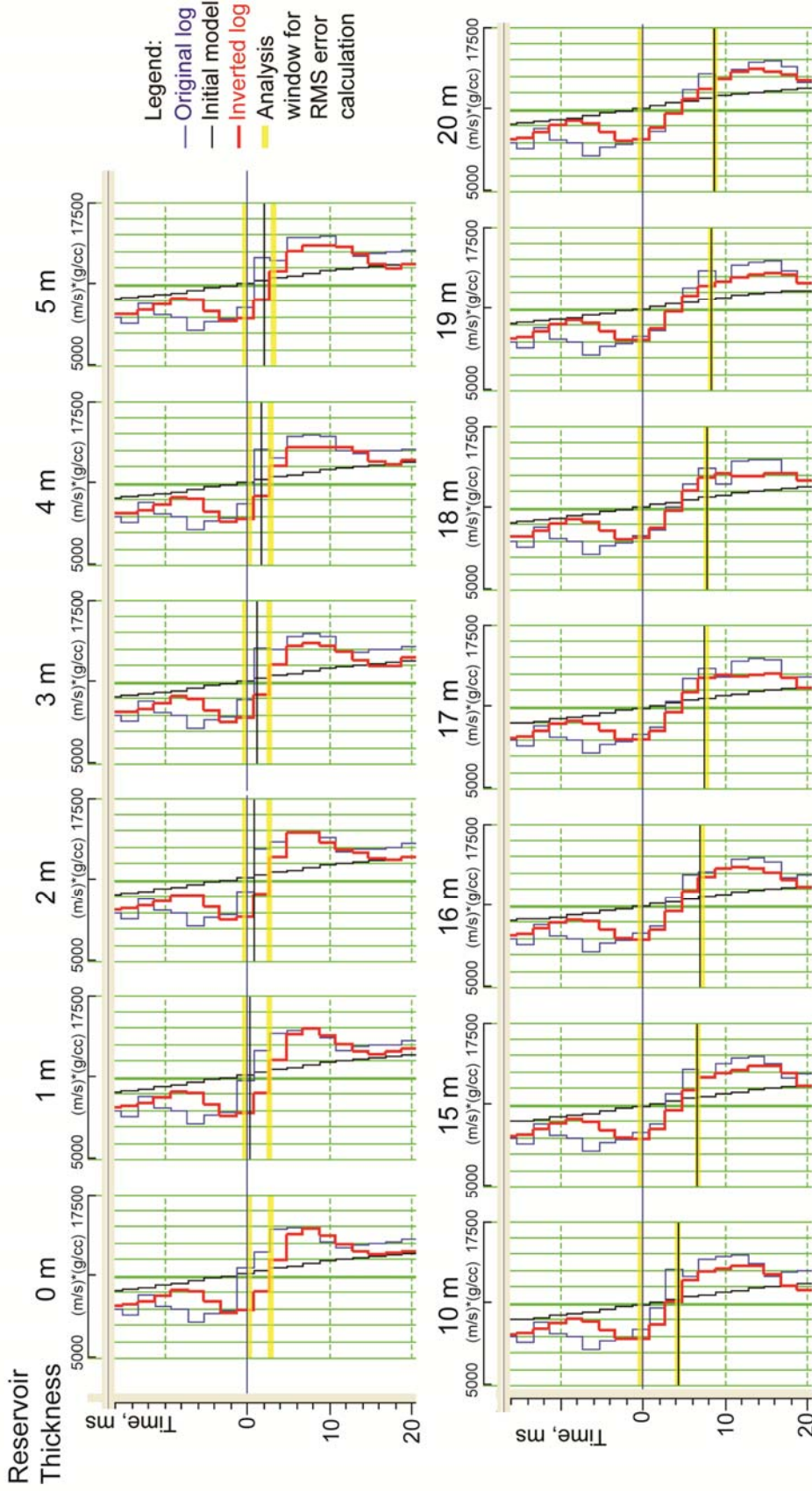


Figure 4.36. Analysis of the model-based inversion result of the synthetic wedge model (shown in Figure 4.17) within the reservoir interval for the wedge thickness ranges 0-5, 10 and 15-20 m. Initial low-frequency model, inverted impedance traces and original impedance logs are shown as black, red and blue curves respectively.

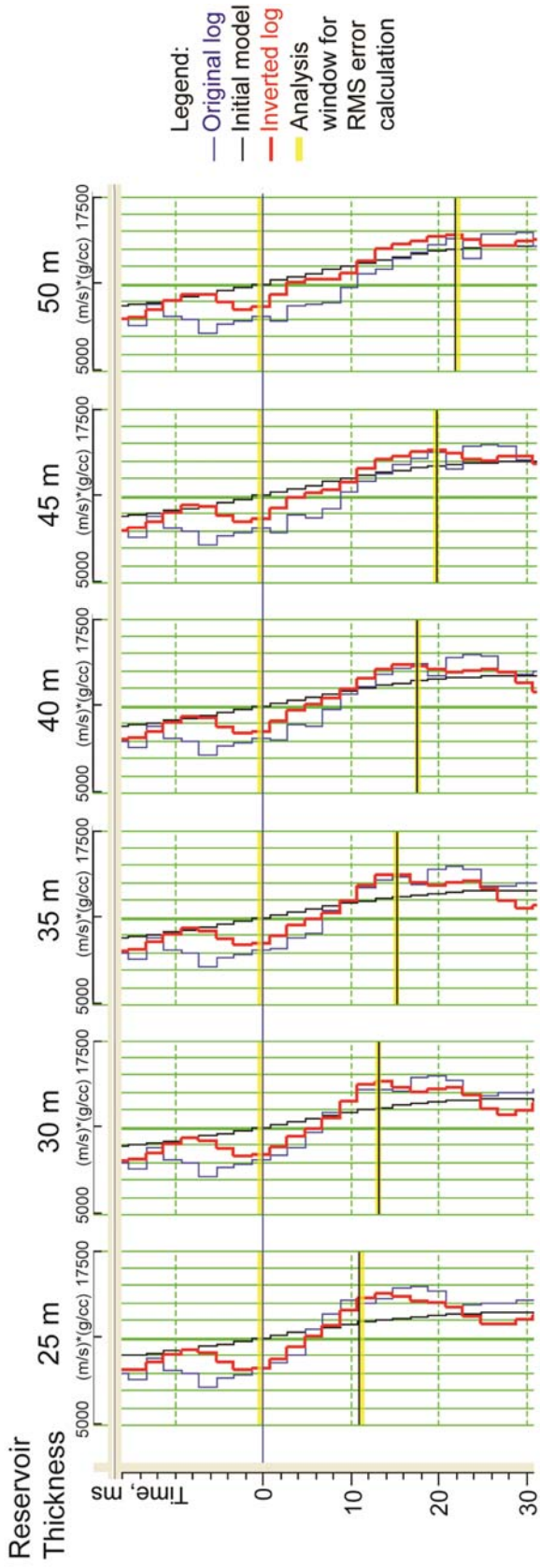


Figure 4.37. Analysis of the model-based inversion result of the synthetic wedge model (shown in Figure 4.17) within the reservoir interval for the wedge thickness range 25-50 m with 5 m step. Initial low-frequency model, inverted impedance traces and original impedance logs are shown as black, red and blue curves respectively.

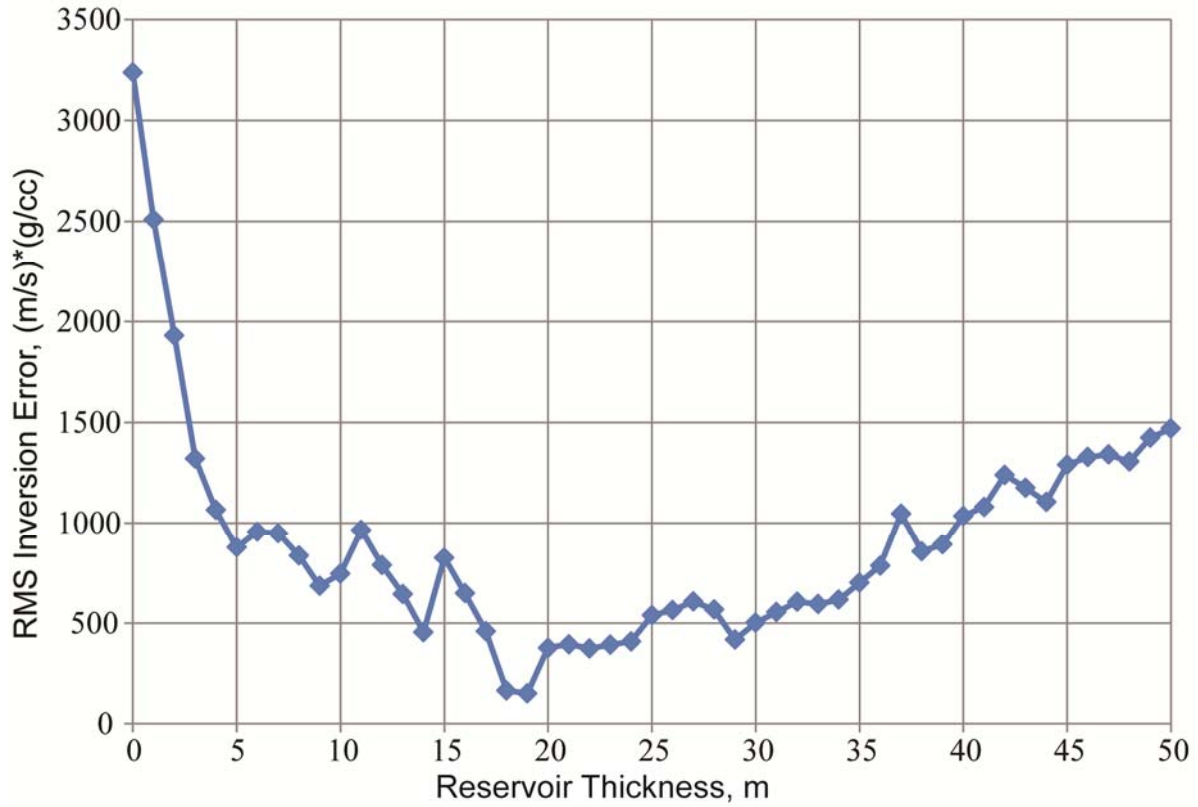


Figure 4.38. Crossplot of the RMS error of the model-based inversion of the synthetic wedge model (shown in Figure 4.17) versus the wedge thickness. The RMS prediction errors were calculated within the analysis window shown with yellow horizontal lines in Figures 4.36 and 4.37.

4.5: Multiattribute porosity prediction

In order to predict porosity in the Mississippian chert reservoir, I examined which seismic attributes statistically relate to the formation porosity measurements at the well locations using multilinear regression analysis available in the Hampson-Russell EMERGE software (Hampson et al., 2001). The established relationship was used to predict porosity throughout the seismic volume in the two-way travel time domain.

4.5.1: Multilinear regression analysis

Formation porosity logs were available at twelve wells tied to the seismic data. The seismic attributes used in the analysis included acoustic impedance, estimated as described in section 4.4, and sample-based seismic attributes internally calculated within the Hampson-Russell EMERGE software (Table 4.3). Composite traces of all seismic attributes were extracted as the average of 9 traces around each well location. The analysis was done within the Mississippian chert reservoir interval, delineated by the MissPorTop and MissLowPor markers (Figure 4.2) using time domain seismic PSTM data with the sampling interval of 2 ms.

First, the linear relationships between formation porosity and single seismic attributes were derived by solving the equation for a single-attribute transform:

$$\phi(t) = w_0 + w_1 \cdot A_1(t),$$

where $\phi(t)$ – formation porosity measurements known at the well locations,

$A_1(t)$ – seismic attribute values,

w_0 and w_1 – unknown weights.

Instantaneous attributes:	Amplitude envelope
	Amplitude weighted cosine phase
	Amplitude weighted frequency
	Amplitude weighted phase
	Apparent polarity
	Cosine instantaneous phase
	Instantaneous frequency
	Instantaneous phase
Windowed frequency attributes	Average frequency
	Dominant frequency
Filter slice attributes	Filter 5/10 – 15/20 Hz
	Filter 15/20 – 25/30 Hz
	Filter 25/30 – 35/40 Hz
	Filter 35/40 – 45/50 Hz
	Filter 45/50 – 55/60 Hz
	Filter 55/60 – 65/70 Hz
Derivative attributes	Derivative
	Derivative instantaneous amplitude
	Second derivative
	Second derivative instantaneous amplitude
Integrate attributes	Integrate
	Integrate absolute amplitude

Table 4.3. Seismic attributes used in the multilinear regression analysis.

Weights w_0 and w_l were estimated for each attribute by the least-squares minimization approach (Hampson et al., 2001). The best single seismic attribute $A^l_1(t)$ providing the lowest average RMS prediction error for all wells was selected as the first attribute in the multilinear transform.

During the second step a pair of seismic attributes that provide the lowest average RMS prediction error for all wells was selected by solving the equation for two-attribute transform with the first attribute being fixed as selected after the first step ($A^1_1(t)$):

$$\phi(t) = w_0 + w_1 \cdot A^1_1(t) + w_2 \cdot A_2(t),$$

where $\phi(t)$ – formation porosity measurements known at the well locations,

$A^1_1(t)$ – the best single attribute for porosity prediction,

$A_2(t)$ – seismic attribute values,

w_0, w_1 and w_2 – unknown weights.

This equation was also solved using least-squares minimization approach. As a result, the best pair of seismic attributes ($A^1_1(t)$ and $A^2_2(t)$) and weights w_0, w_1 and w_2 were determined.

This process, known as step-wise regression, continued further to find the transform of the suite of N seismic attributes that provide the lowest average RMS error for all wells:

$$\phi(t) = w_0 + w_1 \cdot A^1_1(t) + \dots + w_N \cdot A^N_N(t)$$

For computational efficiency, I set the maximum number of attributes to be found for the multilinear transform to 8. Simple mathematical transforms of porosity and seismic attribute values, such as square, square root, natural logarithm, exponent and inverse, were also considered.

I also tested if any improvement can be achieved by using the convolutional operator, a parameter that determines the length of the window (number of samples) in which weighted average of a seismic attribute corresponded to each well-log measurement. I examined operator lengths ranging from 1 to 8 samples.

In order to determine the optimum number of seismic attributes, test their validity, and choose the optimum operator length, I used a cross-validation technique which imitated drilling

new wells to test prediction results (Figure 4.39). This technique was used because the step-wise regression algorithm always leads to a lower RMS prediction error with increasing number of attributes, and could result in data overfitting and the use of spurious relationships (Figure 4.40). The cross-validation process consequently removed each well from the analysis and treated it as a blind well, derived the multiattribute transform as described above, but using 11 wells only (excluding a blind well), applied the derived transform to the blind well and computed a RMS prediction error, called a validation error (Hampson et al., 2001). The average RMS validation errors for all wells were calculated for each number of attributes used in the transform and each operator length. The shape of validation error curves plotted against the number of attributes had one or several local minima (Figure 4.39). Increases of validation error indicated the data overfitting (Hampson et al., 2001). The optimum number of seismic attributes for each operator length was chosen within the first local minimum at the point after which no significant decrease of validation error was observed (Figure 4.39). The analysis showed no significant decrease of validation error with varying operator length, and a one-point operator was chosen and examined further. For the one-point operator the validation error slightly decreased from 3.7% for the single attribute transform to 3.4% for the two-attribute transform, the addition of the 3rd attribute brought a minor improvement, and starting with the 4th attribute the validation error increased indicating data overfitting (Figure 4.39-4.40, Table 4.4). So, the multiattribute transform using one-point operator and two attributes, acoustic impedance and integrate, provided the lowest validation error. However, the integrate attribute, as a simple analogue of acoustic inversion (Hart and Chen, 2004) exhibited high correlation with inverted impedance (Figure 4.41). Therefore, its use in the multiattribute transform along with acoustic impedance was deemed to be redundant.

As a result of the multilinear regression analysis, the only one attribute, acoustic impedance, was chosen for porosity prediction. Even though simple mathematical transforms of acoustic impedance, like square and inverse, showed slightly lower prediction error than acoustic impedance itself, I chose a linear transform with acoustic impedance for porosity prediction as being meaningful in rock physics.

4.5.2: Porosity prediction

Following the multilinear regression analysis described earlier, I derived a linear relationship between formation porosity ($\phi(t)$) and a single seismic attribute, acoustic impedance ($AI(t)$), for the Mississippian chert reservoir (Figure 4.42):

$$\phi(t)=0.5478-3.68 \cdot 10^{-5} \cdot AI(t).$$

The quality of porosity prediction was analyzed at the well locations by visual comparison of original and predicted formation porosity logs and calculation of RMS prediction errors for all wells (Figure 4.43). The predicted formation porosity logs (red curves) show a good agreement with original formation porosity logs within the Mississippian reservoir (analysis window is shown with blue horizontal lines). However, formation porosity values are not valid outside the reservoir because the transform was derived within the reservoir interval. The average prediction error for all wells used in the multilinear regression analysis of 3.5% was considered satisfactory, and the derived transform was applied to the inverted impedance volume in order to predict porosity distribution within the Mississippian reservoir (Figure 4.44-4.45). Figures 4.44 and 4.45 show the predicted porosity sections with the overlain formation porosity log at well #15-191-22591. The reservoir top and base, MissPorTop and MissLowPor, are shown with red horizontal lines on the log curve at the well location. Predicted porosity exhibit good agreement with the formation porosity log within the reservoir interval at the well location and

show the porosity distribution along the porosity sections. However, the predicted porosity values are valid within the reservoir interval only (along the MissTop seismic horizon) and are not valid outside the reservoir.

Number of attributes	Seismic attribute	Prediction error porosity fraction	Validation error, porosity fraction	Derived multiattribute transform
1	Inverted acoustic impedance (AI)	0.035035	0.037383	$\sqrt{(\phi) = 0.65 - 2.12 \cdot 10^{-10} \cdot (AI)^2}$
2	Integrate (INT)	0.032532	0.034778	$\sqrt{(\phi) = 0.84 - 3.76 \cdot 10^{-10} \cdot (AI)^2 - 0.023 \cdot INT}$
3	Dominant frequency (DF)	0.031769	0.034662	$\sqrt{(\phi) = 0.87 - 3.3 \cdot 10^{-10} \cdot (AI)^2 - 0.014 \cdot INT - 0.0016 \cdot DF}$
4	Second derivative (SD)	0.030315	0.034743	$\sqrt{(\phi) = 0.87 - 2.86 \cdot 10^{-10} \cdot (AI)^2 - 0.0033 \cdot INT - 0.0027 \cdot DF + 0.035 \cdot SD}$
5	Filter 35/40 - 45/50 Hz (FILT_1)	0.029941	0.036532	$\sqrt{(\phi) = 0.9 - 3.14 \cdot 10^{-10} \cdot (AI)^2 - 0.0098 \cdot INT - 0.0025 \cdot DF + 0.034 \cdot SD + 0.033 \cdot FILT_1}$
6	Filter 15/20 - 25/30 Hz (FILT_2)	0.029037	0.036785	$\sqrt{(\phi) = 1.08 - 3.75 \cdot 10^{-10} \cdot (AI)^2 - 0.018 \cdot INT - 0.0033 \cdot DF + 0.026 \cdot SD + 0.074 \cdot FILT_1 + 0.12 \cdot FILT_2}$
7	Average frequency (AF)	0.028520	0.045259	$\sqrt{(\phi) = 1.53 - 3.78 \cdot 10^{-10} \cdot (AI)^2 - 0.017 \cdot INT - 0.0028 \cdot DF + 0.031 \cdot SD + 0.08 \cdot FILT_1 + 0.14 \cdot FILT_2 - 0.0086 \cdot AF}$
8	Average weighted frequency (AWF)	0.028102	0.047333	$\sqrt{(\phi) = 1.68 - 4.14 \cdot 10^{-10} \cdot (AI)^2 - 0.019 \cdot INT - 0.003 \cdot DF + 0.04 \cdot SD + 0.087 \cdot FILT_1 + 0.18 \cdot FILT_2 - 0.0097 \cdot AF - 0.00022 \cdot AWF}$

Table 4.4. Result of the multilinear regression analysis using one-point convolutional operator. Note that prediction error decreased with increasing number of attributes. Validation error was used to determine the optimum number of seismic attributes: 3 attributes provided the lowest error, but the 3rd attribute brought insignificant improvement, therefore two-attribute transform was selected. However, the second attribute, integrate, was also disregarded being analogous to acoustic impedance (Figure 4.25).

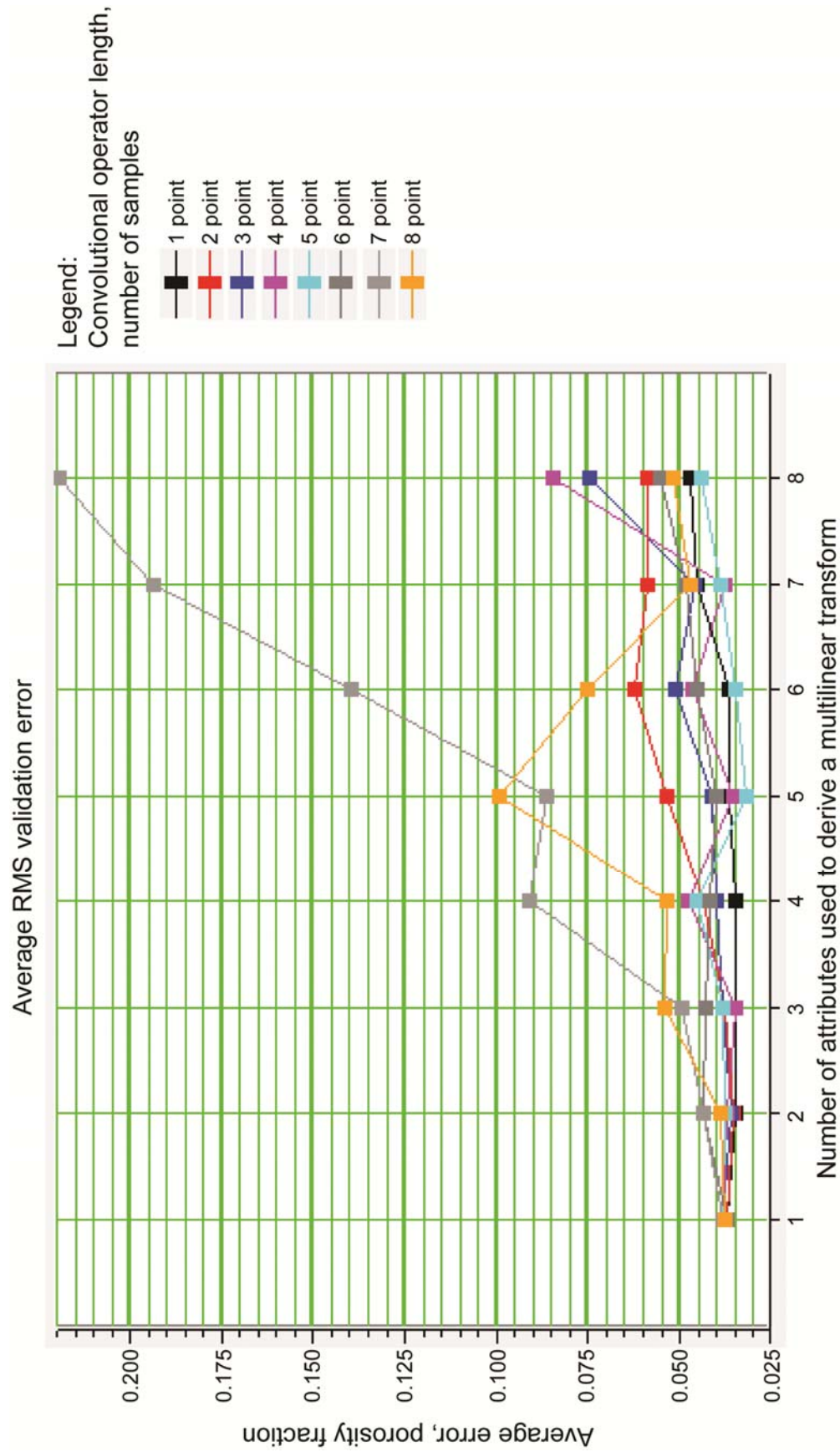


Figure 4.39. Average RMS validation error versus the number of seismic attributes used in the multilinear porosity prediction for the lengths of the convolutional operator from 1 to 8.

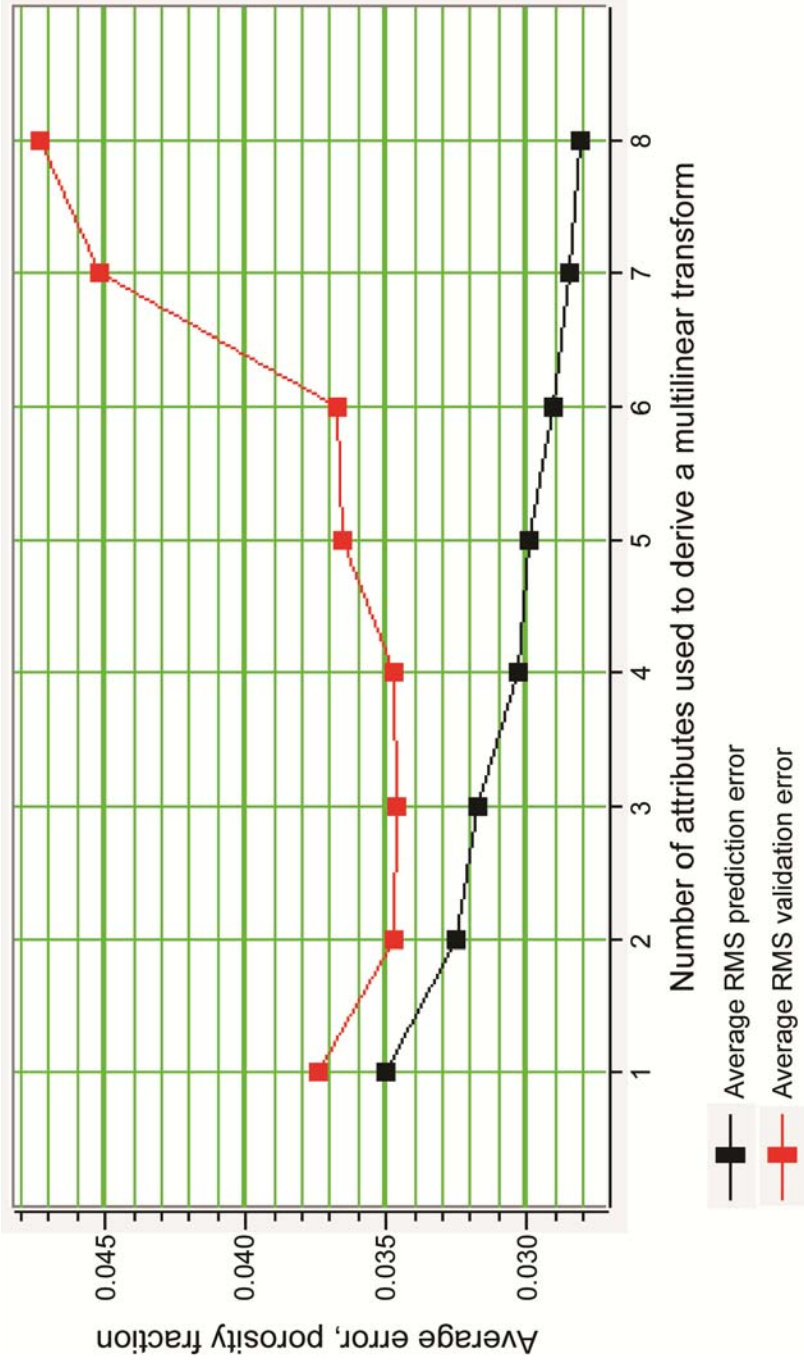


Figure 4.40. Average RMS prediction and validation errors versus the number of seismic attributes used in the multilinear porosity prediction. The length of the convolutional operator equals 1.

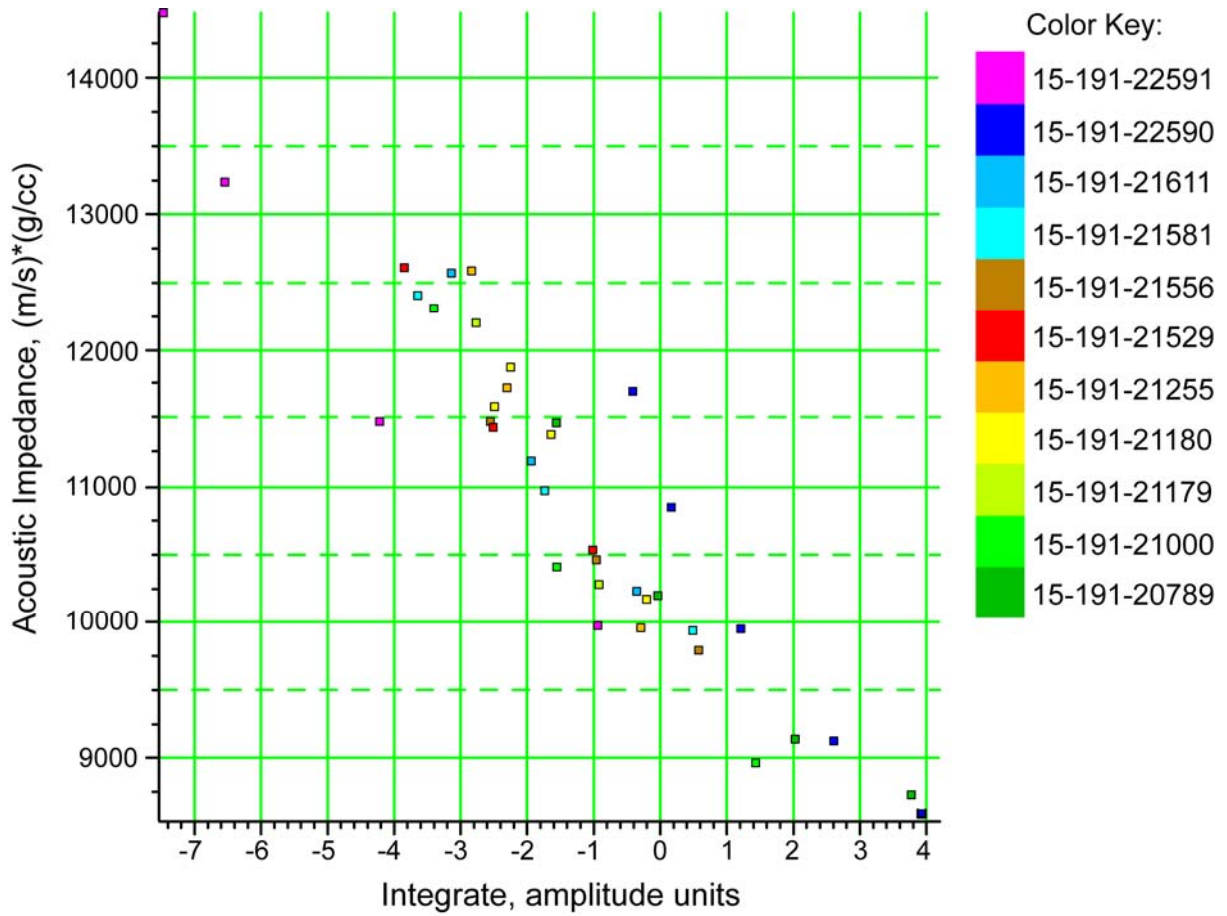


Figure 4.41. Crossplot of inverted acoustic impedance versus integrate attribute within the Mississippian chert reservoir at twelve well locations. A linear correlation between acoustic impedance and integrate attribute with correlation coefficient of -0.95 was observed. Integrate attribute was disregarded from the transform being an analogous to acoustic impedance.

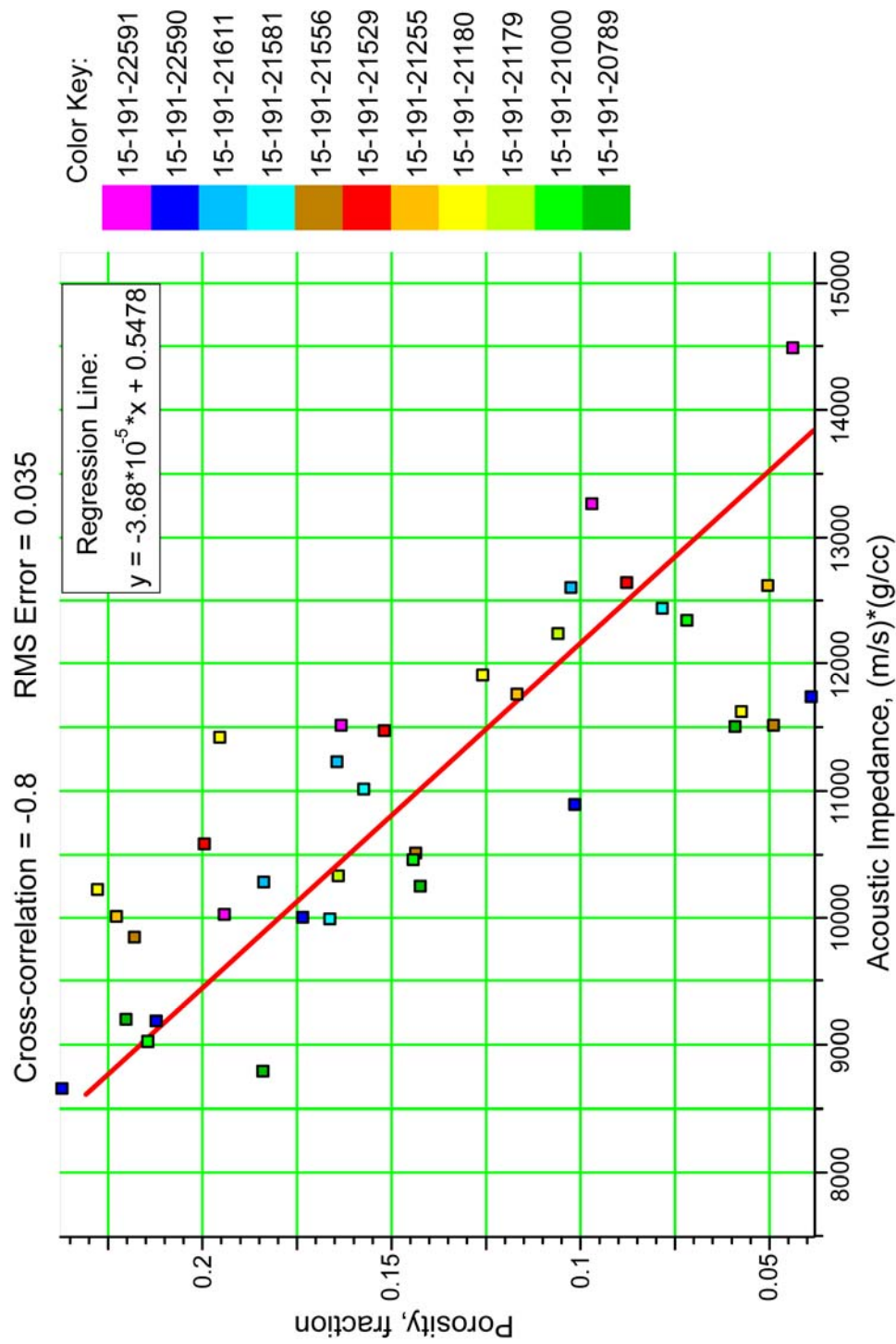


Figure 4.42. Crossplot of inverted acoustic impedance versus formation porosity logs within the Mississippian chert reservoir at twelve well locations. The crossplot shows a high linear correlation between porosity and acoustic impedance with the average RMS prediction error of 3.5%.

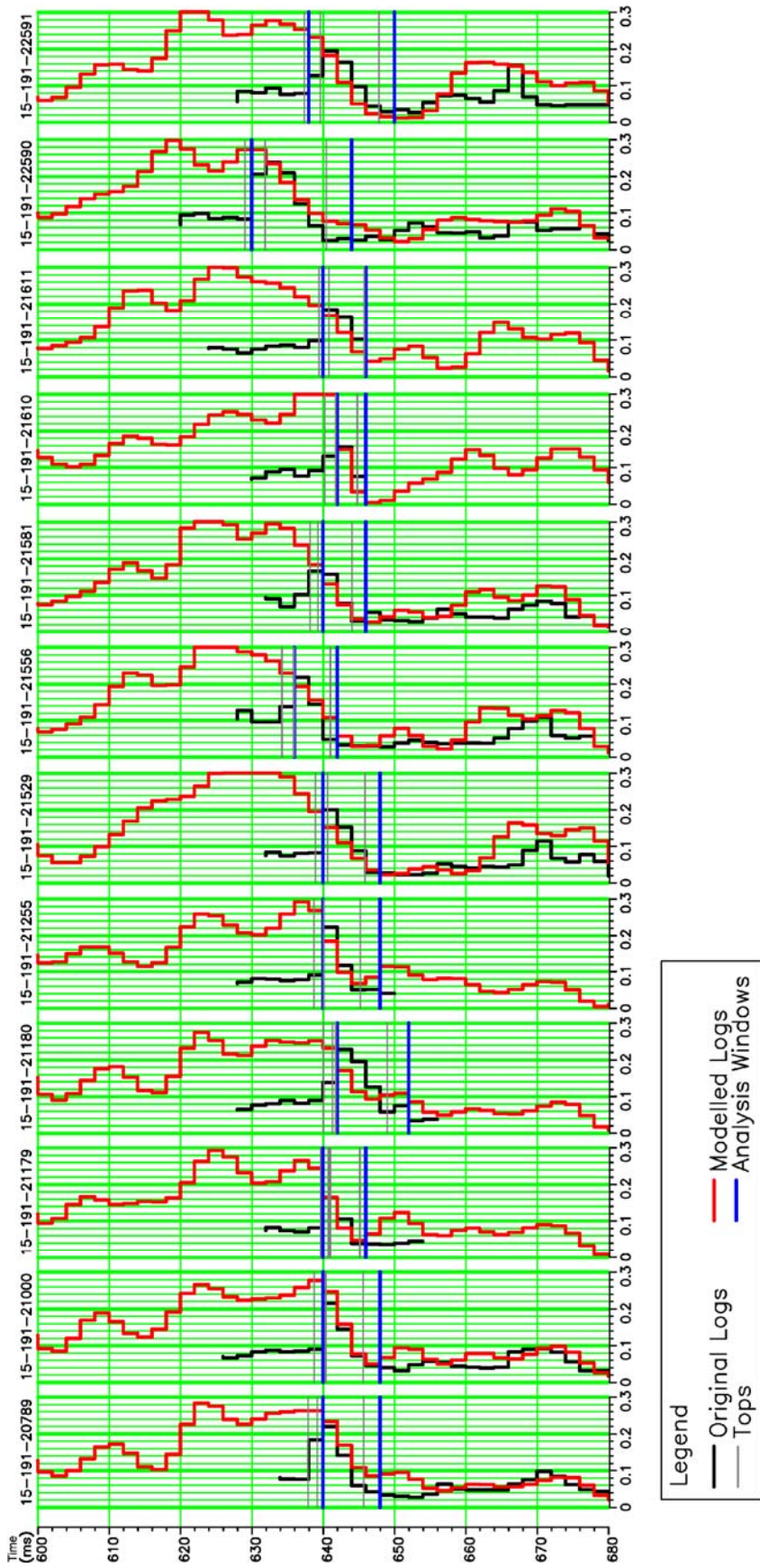


Figure 4.43. Analysis of the porosity predictions from the acoustic impedance within the Mississippiian reservoir (shown by the blue horizontal lines of the analysis window) at 12 well locations. The predicted formation porosity traces (red) show good agreement with the original formation porosity logs (black). The average RMS prediction error for all wells is 3.5%.

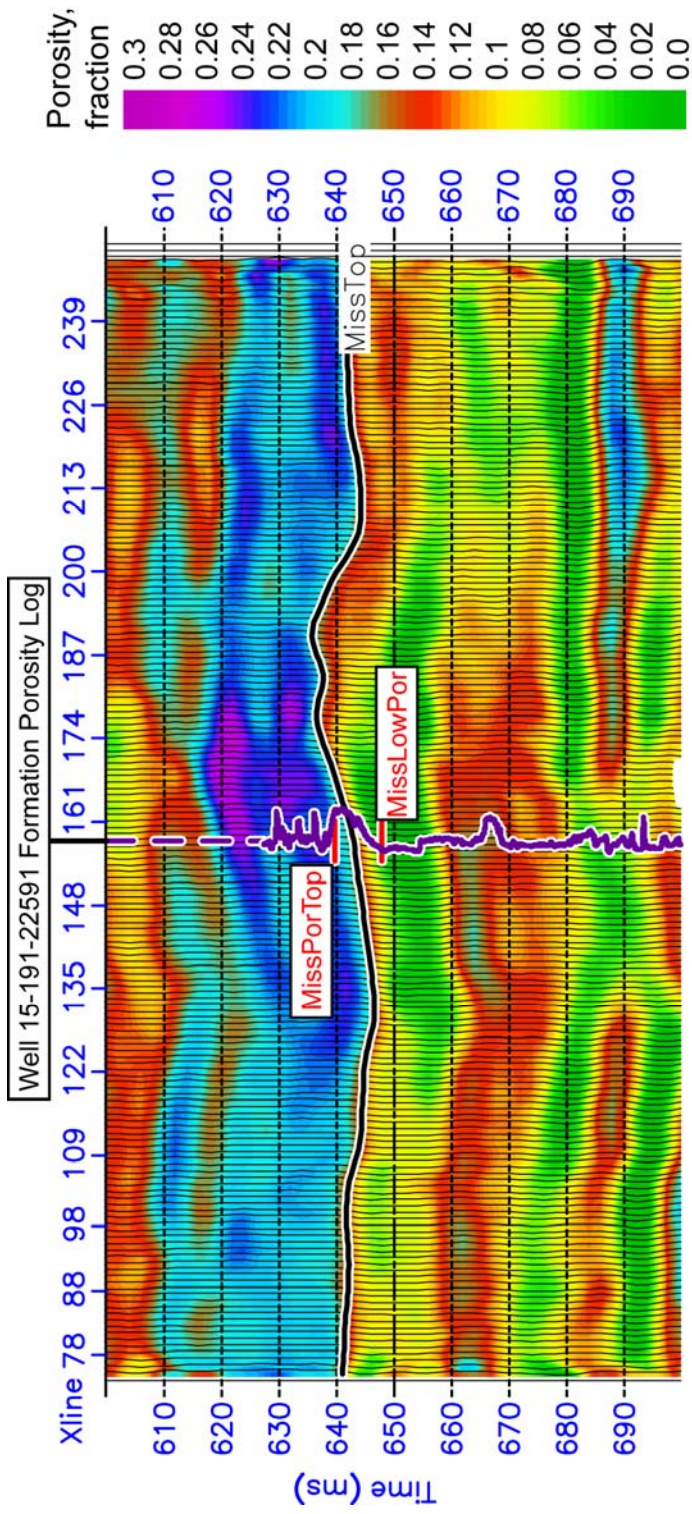


Figure 4.44. Result of the formation porosity prediction from the inverted impedance volume across the inline #152 with overlain original formation porosity log at well #15-191-22591.

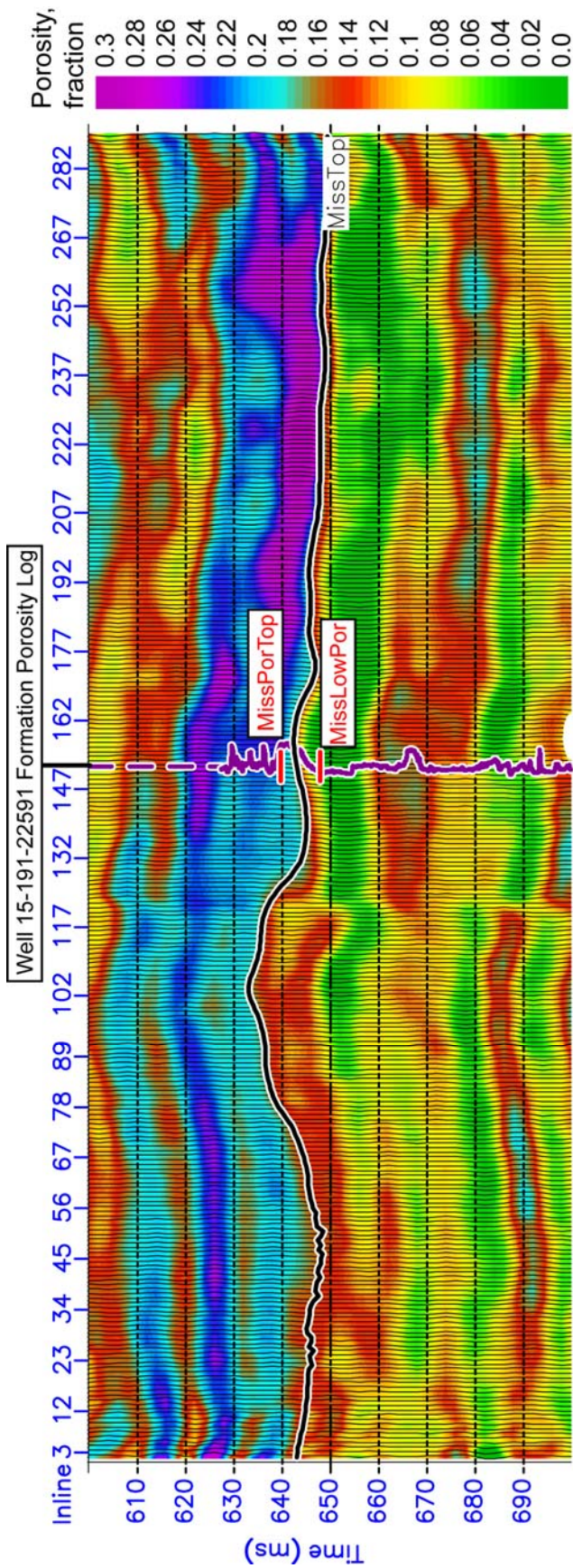


Figure 4.45. Result of the formation porosity prediction from the inverted impedance volume across the crossline #158 with overlain original formation porosity log at well #15-191-22591.

CHAPTER 5: RESULTS AND DISCUSSION

5.1: Well Log Interpretation

The depth map of the top of the Mississippian System, constructed based on well top data downloaded from the KGS website and edited using well logs, shows the structural control of the Mississippian chert reservoir at the Wellington Field (Figure 4.1). The Wellington Field is producing in the areas with shown well locations (Figure 4.1; KGS, 2012). Production in the middle part of the field relates to the structure. However, production in the southern part of the field corresponds to a structurally lower area. Therefore, the Mississippian chert reservoir is characterized by a combined effect of structural control and depositional and diagenetic histories. The Mississippian reservoir was delineated using formation porosity logs at thirteen wells, density porosity logs at seven wells and both density and neutron porosity logs at four wells (Figures 5.1-5.2). Two wells with formation porosity logs, #15-191-21610 and 15-191-21611, did not penetrate the base of the Mississippian reservoir and were used only in the multiattribute porosity prediction described in section 4.5. The reservoir top and base was picked at all the other 22 wells with different types of porosity logs in order to investigate the seismic response of the Mississippian reservoir characterized by a gradational downward porosity decrease with varying thickness. The reservoir exhibits high heterogeneity with thickness varying from 6 to 20 meters at the analyzed wells. I divided these 22 wells into two groups based on the porosity distribution as well as the seismic response discussed later in section 5.3.

Group #1

Porosity logs at 11 well locations show a downward porosity decrease from 24-30% at the reservoir top to 4-6% at the reservoir base (Figure 5.1). Thickness at these wells varies in the range 6-20 m. This group of wells exhibits a characteristic downward porosity decrease within

the Mississippian chert reservoir. As shown in Figures 2.4 and 4.3 and discussed in section 2.3, this gradational downward porosity decrease causes the corresponding increase in velocity within the reservoir interval, or a ramp-transition velocity function. Modeling of the seismic response of a ramp-transition velocity function using synthetic and original sonic logs at the Wellington Field (chapter 3 and section 4.3.4) showed that seismic amplitude and frequency can be potentially used for reservoir thickness prediction. Therefore, I used this group of wells to investigate if seismic amplitude and frequency can be used to predict the reservoir thickness at the Wellington Field in section 5.3.2. In addition, a slightly porous thin interval with porosities 6-9%, ≈ 4 m thick, is present below the reservoir bottom, around 20 m deep from the reservoir top, at these wells. This interval was mentioned in section 4.3.4 as its seismic reflection potentially interfering with the reflection from the reservoir base in the synthetic seismic section built at well #15-191-20789. It is further discussed in section 5.3 as one of the factors causing the locally developed double reflector at the Mississippian top mentioned in section 4.3.2.

Group #2

Well logs at the other 11 wells, shown in Figure 5.2, reveal more heterogeneous porosity distribution within the reservoir interval. Three of these wells, #15-191-21534, 15-191-21626 and 15-191-22591, also demonstrate a gradational downward porosity decrease. However, their seismic response, discussed later in section 5.3, differ from the wells of the group #1. The porous chert at well #15-191-21921 is 17 m thick and shows relatively constant porosity of 18-20%. All the wells in group #2, except #15-191-21921 and 15-191-22591, are located close to each other within the Wellington West Field (Figure 4.1). These wells encounter the reservoir 7-9 m thick with highly heterogeneous porosity distribution. Well #15-191-21563 is characterized by the reservoir with relatively constant porosity of 20%, while well log at well #15-191-21534 shows

porosity gradationally decreasing downward from 20 to 5%. Porosity logs at all the other wells at the Wellington West Field show vertical porosity profiles that vary from a gradational downward porosity decrease to relatively uniform porosity distribution. In general, porosities at the Wellington West Field are less than 15%. The slightly porous interval below the Mississippian reservoir observed at the wells of the group #1 shown in Figure 5.1 is not present at the wells of the group #2 shown in Figure 5.2.

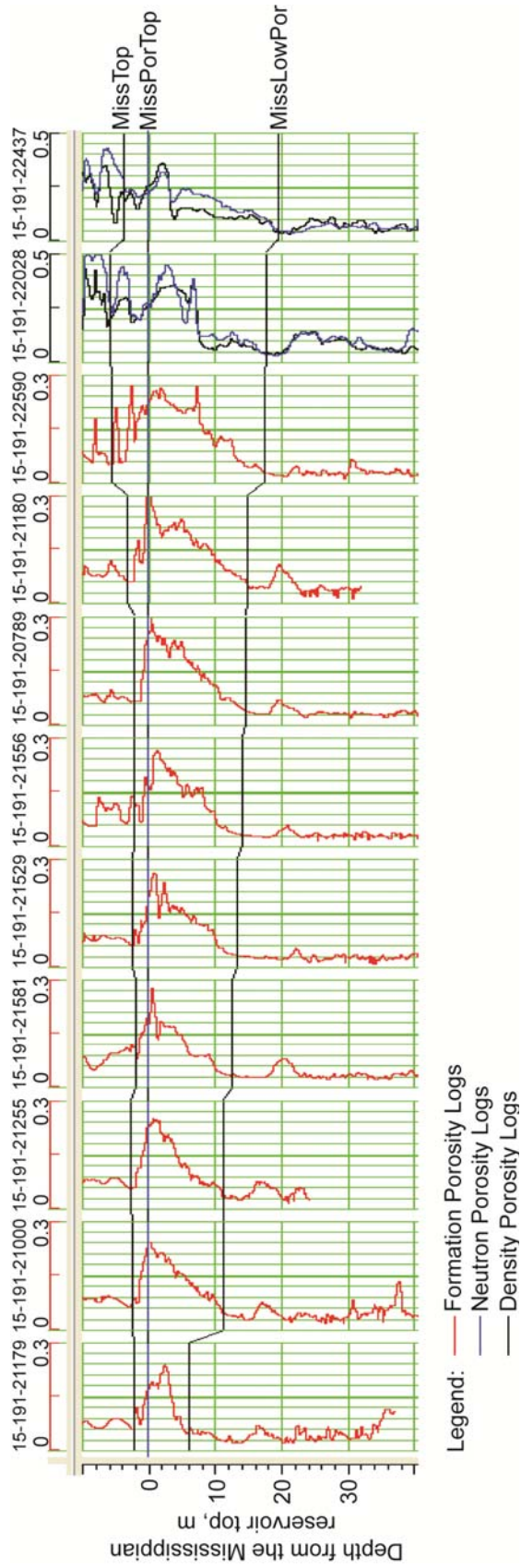


Figure 5.1. Mississippian chert reservoir delineated on porosity logs of the wells of the group #1. MissTop corresponds to the top of the reworked Mississippian chert, MissPorTop and MissLowPor correspond to the top and the base of the reservoir respectively.

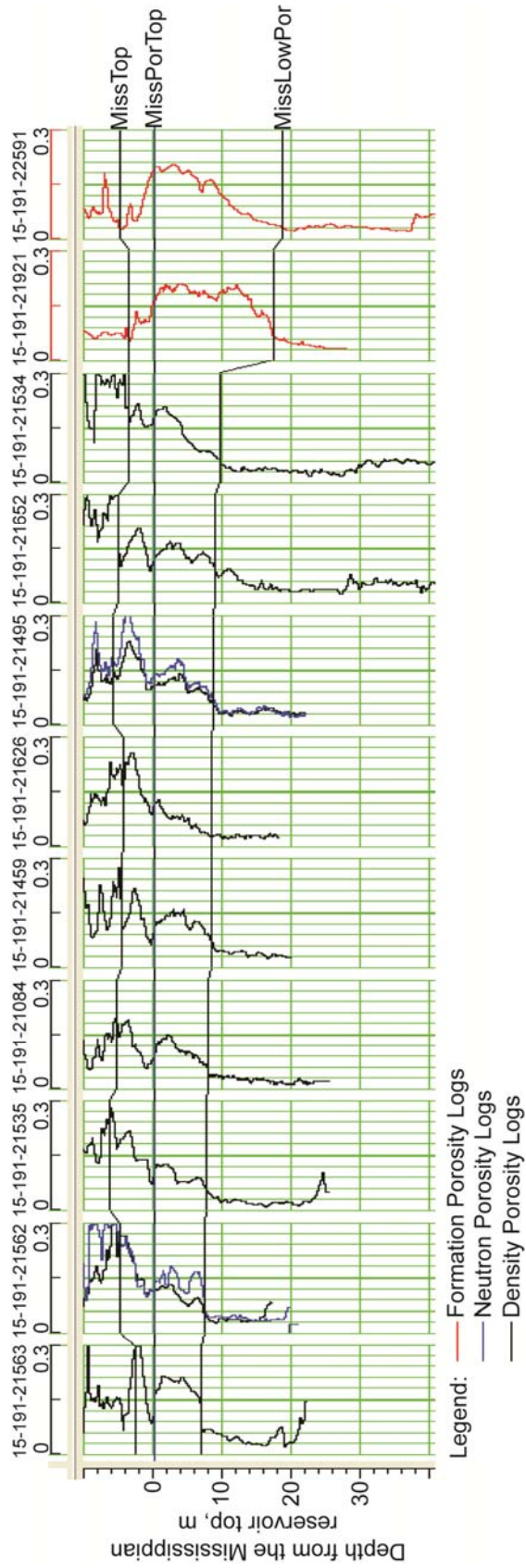


Figure 5.2. Mississippian chert reservoir delineated on porosity logs of the wells of the group #2. MissTop corresponds to the top of the reworked Mississippian chert, MissPorTop and MissLowPor correspond to the top and the base of the reservoir respectively.

5.2: Pseudo-sonic Well Logs

The pseudo-sonic logs generated at the two test wells, #15-191-20789 and 15-191-22591, show a good agreement with the original sonic logs throughout the geological section at these wells (Figure 4.6). The ramp-transition velocity function within the Mississippian reservoir (below the MissTop marker) is also preserved on the pseudo-sonic logs. The pseudo-sonic well logs generated at the eleven wells with formation porosity logs allowed tying these wells to the seismic data and, therefore, the use of formation porosity logs in multiattribute porosity prediction described in section 4.5.

5.3: Seismic Data Interpretation

Conventional interpretation of the seismic data at the Wellington Field provided the main structural framework for the detailed study of the Mississippian reservoir including analysis of instantaneous seismic attributes (section 5.3.1), post-stack model-based inversion (section 5.4) and multiattribute porosity prediction (section 5.5).

5.3.1: Conventional Seismic Interpretation and Analysis of Instantaneous Seismic Attributes

The polarity of the PSTM seismic data received for interpretation is reversed according to the SEG polarity convention as determined during the wavelet extraction and well-to-seismic tie processes in section 4.3.2 (Figures 4.8-4.10). However, I use mostly SEG normal polarity for display purposes, and the polarity used for data display is always specified in the figure captions.

High-quality well-to-seismic tie performed at three wells, #15-191-20789, 15-191-22591 and 15-191-30147, allowed the correlation of seismic horizons to main stratigraphic markers (Table 4.2, Figure 4.8). Such stratigraphic surfaces as tops of the Lecompton Limestone (LeCompton), the Kansas-City Group (KCTop) and the Arbuckle Group (Arbuckle) are characterized by positive high-impedance contrasts (Figure 4.8). The character of the sonic log at

these boundaries is a step velocity function. Associated reflections on the zero-phase reversed polarity seismic data represent high-amplitude troughs, and the well tops correspond to the trough minima. A transitional boundary is observed below the top of the Mississippian System (MissTop), within the reservoir interval. The character of the sonic log within the reservoir interval (below MissTop) is a ramp-transition velocity function. The associated seismic reflection also represents a trough on the zero-phase reversed polarity seismic data, but the MissTop marker is shifted from the trough minimum towards the preceding zero-crossing, while the trough minimum corresponds to the middle of the transitional layer (which is the Mississippian chert reservoir) (Figure 4.8). This example of the synthetic seismogram supports the hypothesis that the seismic reflection from the Mississippian chert reservoir represents a seismic response of a ramp-transitional velocity function.

The correlation of four seismic horizons provided the structural framework for the post-stack seismic inversion described in section 4.4. Horizons labeled as LeCompton and KCTop are prominent and consistent throughout the Wellington Field seismic survey (Figures 4.11-4.12). The horizon labeled as Arbuckle is structurally more complicated due to the vertical Precambrian faults. Fault #1 is seen on the seismic data as a discontinuity which starts deep below the Arbuckle horizon and is evident up to the MissTop horizon: between 158 and 175 traces of the inline #152 (Figure 4.11), and around trace 124 of the crossline #158 (Figure 4.12). Another less developed discontinuity, fault #2, is located between 124 and 141 traces of the inline #152 (Figure 4.11). Determining the extent of these faults through the geological section and their mapping across the Wellington Field is a difficult task using the PSTM seismic data due to their inconsistent character. Their influence on the oil production at the Wellington Field is under current investigation (W. L. Watney, 2012, personal communication). I did not map these faults,

but I showed their approximate locations on seismic sections and maps and discussed the seismic response of the Mississippian reservoir regarding the location relative to fault #1. The MissTop reflection associated with the Mississippian chert reservoir demonstrates highly inconsistent and variable character across the seismic survey (Figures 4.11-4.12). Smoothed seismic horizons were used to build the initial impedance model for model-based inversion.

Following the horizon interpretation, I conducted detailed analysis of the seismic reflection character associated with the Mississippian reservoir. The seismic response of the Mississippian reservoir highly varies across the Wellington Field. The most sudden changes of the seismic response occur across fault #1. Overall lower amplitudes and frequencies are observed to the east of fault #1 along inline #152, and to the south of this fault along crossline #158 (Figures 4.11-4.12). These changes across fault #1 and the spatial orientation of fault #1 are more evident on the attribute maps of the MissTop reflection (Figures 4.15-4.16). Fault #1 divides the Wellington Field seismic survey diagonally from the south-western corner to the north-eastern corner. The north-western part of the seismic survey is characterized by higher amplitudes (3-6 amplitude envelope range) and higher frequencies (40-60 Hz instantaneous frequency range). Lower amplitudes, 0-3, and frequencies, 20-50 Hz, with locally developed high-frequency areas, 50-70 Hz, dominate in the south-eastern part. In addition, a double reflection associated with the Mississippian reservoir is observed locally: 175-209 traces of the inline #152 (Figure 4.11) and 79-124 traces of the crossline #158 (Figure 4.12). The MissTop horizon corresponds to the upper reflection. Another horizon, MBase, tracks the MissTop in the areas where a single reflection is observed from the reservoir and honors the lower reflection in areas of the double reflector (Figure 4.13). The two-way travel time separation (isochron map) between the MissTop and MBase reflections delineates the areas of the double reflector (Figure

5.3). The double reflector is developed on the south-eastern flank of the fault #1 and is absent to the north-west across this fault (Figures 4.13 and 5.3). Sections 4.3.4 and 5.1 identified the thin slightly porous interval right below the reservoir base which is characterized by lower velocities than surrounding strata (Figures 4.13, 4.17 and 5.1). This thin layer is present only on the side of fault #1 where the double reflector is developed as seen in sonic and pseudo-sonic well logs overlain on the arbitrary line in Figure 4.13. These differences in the seismic response of the Mississippian reservoir and character of the porosity distribution within the reservoir on porosity logs were the basis for grouping the wells by their location relative to fault #1 as already mentioned in section 5.1.

Group #1

Group #1 contains wells located on the south-eastern part of the Wellington Field. Porosity logs of this group of wells exhibit a characteristic downward porosity decrease within the Mississippian chert reservoir, and the thin slightly porous layer is present below the reservoir base (section 5.1, Figure 5.1). The seismic response of the Mississippian reservoir is characterized by the locally developed double reflector and the overall lower amplitude and frequency content in this part of the field as noted earlier in this section (Figures 4.15-4.16 and 5.3).

Amplitude and frequency values show a linear correlation with the reservoir thickness at the wells of group #1 (Figures 5.4-5.8). Figures 5.4-5.8 show the crossplots of raw seismic amplitude, amplitude envelope and instantaneous frequency of the MissTop reflection versus the reservoir thickness at the well locations. Linear relationships between seismic attributes and the reservoir thickness were derived by linear regression analysis and are shown in the right top corners of the crossplots. Raw seismic amplitudes and amplitude envelope values taken at the

peak of the MissTop reflection are almost identical (Figures 5.4-5.5). Both raw amplitude and amplitude envelope linearly decrease from ≈ 2.8 -3 to 0.6 ($\approx 80\%$) as the reservoir thickness increases from 6 to 20 m. The straight line fit correlation coefficients are 0.84 for the raw amplitude and 0.85 for the amplitude envelope versus reservoir thickness crossplots. The instantaneous frequency exhibits an overall decrease from ≈ 60 to 40-45 Hz (25-33%) as the reservoir thickness increases from 6 to 20 m, but a large scatter is observed in this crossplot with low correlation coefficient 0.4 (Figure 5.6). I calculated RMS errors of reservoir thickness predictions using these relationships. RMS errors of reservoir thickness prediction using raw amplitude and amplitude envelope are 2.26 m and 2.195 m respectively. Reservoir thickness prediction using instantaneous frequency shows a high RMS error of 8.16 m. Also, I tested the averaging of amplitude envelope and instantaneous frequency values within 3 by 3 trace squares around well locations. Both averaged amplitude envelope and averaged instantaneous frequency showed almost identical values as the amplitude envelope and instantaneous frequency values taken from the traces closest to well locations with slightly lower correlation coefficients, 0.84 and 0.35 respectively, and higher RMS prediction errors, 2.27 m and 9.55 m respectively (Figures 5.7-5.8). The observed decrease in seismic amplitude ($\approx 80\%$) and frequency (25-33%) as the reservoir thickness increases from 6 to 20 m demonstrates a good agreement with the amplitude (74%) and frequency (17%) decrease expected from modeling of the ramp-transition velocity function as described in chapter 3. This agreement supports the hypothesis that the variations of the seismic amplitude and frequency across the south-eastern part of the Wellington Field are mainly caused by the ramp-transition velocity function within the Mississippian reservoir. As already reported in section 2.3, the ramp-transition velocity function is caused by the gradational downward porosity decrease within the Mississippian reservoir at the Wellington

Field. Therefore, amplitude and frequency of the MissTop reflection can be used to predict the thickness of the chert reservoir characterized by a gradational downward porosity decrease at the Wellington Field.

Modeling of the seismic response of a ramp-transition velocity function described in chapter 3 assumed a linear velocity increase within the reservoir from the constant velocity of the overlying layer to the constant velocity of the underlying layer and varied the reservoir thickness only. However, this scenario can be barely met in real geological settings due to the lateral variations above and below the reservoir as well as variations within the reservoir. I calculated the gradient of porosity decrease within the Mississippian reservoir at the well locations of the group #1 and plotted it against the amplitude envelope and instantaneous frequency (Figures 5.9-5.10). The crossplot of the average amplitude envelope versus the gradient of porosity decrease demonstrates a higher correlation coefficient of 0.89 and very low prediction error of 0.12%/m (Figure 5.9). The outlier shown as a green diamond corresponds to well #15-191-21179 with the 6 m thick reservoir and was not considered in the regression analysis in this case. This outlier also is evident in Figures 5.4, 5.5 and 5.9 with approximate amplitude value of 2.7 which is slightly lower than the amplitude values of 2.8-3.1 at the reservoir thickness of 11 m at wells #15-191-21000 and 15-191-21255. This outlier actually agrees very well with the modeling described in chapter 3 (Figures 3.2 and 3.4). As the ramp-transition velocity function approaches zero thickness, the amplitude increase rate becomes lower 0-10 m thickness range and slowly approaches the amplitude of a step velocity function. Instantaneous frequency shows a low correlation coefficient of 0.14 when plotted against the gradient of porosity decrease (Figure 5.10). Overall, frequency is a less reliable attribute for prediction of the thickness of the Mississippian reservoir at the Wellington Field.

Finally, I used the relationship derived for the amplitude envelope showed in Figure 5.5 to predict the thickness of the Mississippian reservoir characterized by a gradational downward porosity decrease in the south-eastern part of the Wellington Field. The amplitude envelope was chosen because it shows a higher correlation coefficient of 0.85 and provides the least RMS prediction error of 2.195 m. However, either raw seismic amplitude or the averaged amplitude envelope can be used for the reservoir thickness prediction as these attributes are almost identical. The resultant thickness map is shown in Figure 5.11. This map has reliable values only in the south-eastern half of the field (south-eastern relative to the fault #1) because the relationship between amplitude envelope and the reservoir thickness was derived using the wells of the group #1 only. The Mississippian reservoir in this part of the field is characterized by a gradational downward porosity decrease which causes the ramp-transitional velocity function within the reservoir interval. This characteristic reservoir architecture allowed the use of the seismic amplitude response of the ramp-transitional velocity function as a reliable attribute for reservoir estimation.

Group #2

Group #2 contains wells located in the north-western part of the Wellington Field. Porosity logs of this group of wells show more variability in porosity distribution within the reservoir as described in section 5.1 and shown in Figure 5.2. The seismic response of the chert reservoir is expressed by a single reflection and higher amplitude and frequency content in this part of the field as discussed earlier in this section (Figures 4.15-4.16 and 5.3). However, I was not able to establish a relationship between neither seismic amplitude and the reservoir thickness or seismic frequency and the reservoir thickness in this part of the Wellington Field. Figures 5.12 and 5.13 show large scatter, $\approx 3.2-6$, of both raw amplitude and amplitude envelope at wells

located close to each other within the Wellington West Field (Figure 4.1) and exhibiting approximately the same reservoir thickness of 7-10 m (Figure 5.2). Figure 5.14 shows that these wells are characterized by approximately the same values of instantaneous frequency, around 50 Hz. Wells #15-191-21921 and 15-191-22591, shown as red diamonds demonstrate lower amplitudes, 1.9 and 3.3 respectively, lower frequencies, 33 and 42 Hz respectively, and twice the reservoir thickness than wells in the same group. Formation porosity log at well #15-191-22591 exhibit a characteristic downward porosity decrease within the Mississippian reservoir as discussed in section 5.1, but the seismic response at this well location differs from those wells of the group #1 by higher amplitudes. The reasoning behind this issue is discussed further in section 5.4.

5.3.2: Seismic Wedge Modeling Using Original Sonic Logs

Wedge modeling using original sonic logs was presented in chapter 4, in addition to the modeling of the seismic response of the ramp-transition velocity function described in chapter 3. I intended to test using original sonic logs if the seismic response of the ramp-transition velocity function can be used as the seismic signature of the Mississippian reservoir characterized by a downward porosity decrease. Another goal of this modeling was to investigate the nature of the double reflector and the role of the slightly porous thin layer below the reservoir present in the south-eastern half of the field. Finally, these synthetic seismic sections were used to assess the resolving power of the post-stack model-based inversion algorithm available in Hampson-Russell STRATA software in case of the transitional impedance contrast as described in section 4.4.3 and discussed in section 5.4.2.

Synthetic seismic sections and crossplots of seismic attributes calculated at wells #15-191-20789 and 15-191-22591 show the seismic response of the Mississippian reservoir with

varying thickness (Figures 4.17-4.24). The Mississippian reservoir at these well locations is characterized by a gradational vertical decrease in porosity and corresponding increase in acoustic velocity according to the well-log interpretation (Figures 2.4, 5.1).

The synthetic seismic section built at well #15-191-20789 shows a single reflection, Reflection_1, for the reservoir thickness ranging from 0 to 17 m (Figures 4.17, 4.23). Two reflections, from the reservoir top and bottom – Reflection_1 and Reflection_2_peak, are observed for reservoir thickness greater than 17 m. The base reflection on the synthetic seismic section at well #15-191-20789 displays a trough-peak-trough sequence which is attributed to the interference of a peak-trough reservoir base reflection and trough-peak reflection from the porous low-velocity thin layer right below the reservoir base (mentioned in section 5.1; Figure 4.17). The amplitude envelope attribute taken at the peak of Reflection_1 linearly decreases from 0.4 to 0.15 (62.5%) within the thickness range 0-25 m, and from 0.14 to 0.075 (46%) as the reservoir thickness increases from 25 to 50 m (Figure 4.19). The instantaneous frequency attribute taken within a 5 ms window centered at Reflection_1 shows an overall decrease from 55 to 37 Hz (33%) over the range 0-25 m, but exhibits a larger scatter (Figure 4.20). Lower decrease rate of the instantaneous frequency values is observed for the thickness range 25-50 m. The reflection from the reservoir base, Reflection_2_peak, appears when the reservoir thickness exceeds 17 m (Figures 4.17, 4.23). The separation of the reflections from the top and the base of the reservoir linearly increases from 10 to 25 ms as the reservoir thickness increases from 17 to 50 m (Figure 4.23).

The synthetic seismic section built at well #15-191-22591 shows a single reflection, Reflection_1, for the reservoir thickness ranging from 0 to 20 m (Figures 4.18, 4.24). Two reflections, from the reservoir top and bottom – Reflection_1 and Reflection_2, are observed for

the reservoir thickness greater than 20 m. The amplitude envelope attribute taken at the peak of the Reflection_1 linearly decreases from 0.38 to 0.1 (74%) within the thickness range 0-25 m, and slightly increases from 0.16 to 0.2 as the reservoir thickness increases from 26 to 50 m (Figure 4.21). The instantaneous frequency attribute taken within a 5 ms window centered at Reflection_1 shows a decrease from 55 to 30 Hz (45%) over the range 0-21 m (Figure 4.22). For the reservoir thickness more than 21 m, instantaneous frequency increases from 55 to 70 Hz within the thickness range 21-34 m, and then remains stable at around 70 Hz for the thickness range 34-50 m. The reflection from the reservoir base, Reflection_2, appears for thicknesses more than 20 m (Figures 4.18, 4.24). The separation of the reflections from the top and the base of the reservoir linearly increases from 5 to 17 ms as the reservoir thickness increases from 21 to 50 m (Figure 4.24).

Overall, both synthetic seismic sections demonstrate linear decrease in signal amplitude and frequency within the thickness range of 0-25 m. However, differences occur for the thickness range 25-50 m. These differences are caused by variable velocities within the reworked chert overlying the Mississippian reservoir. An impedance contrast is observed between Pennsylvanian shales and reworked Mississippian chert (3-4 m) at well #15-191-22591, while no impedance contrast between two is present at well #15-191-20789 as seen on sonic logs in Figures 4.17-4.18. At well #15-191-22591 the reflection from this thin reworked Mississippian chert interferes with the reservoir reflection and results in higher frequencies and amplitudes comparing to well #15-191-20789.

Seismic modeling using original sonic logs shows a good agreement with the results presented in section 5.3.1 and the modeling described in chapter 3 for the reservoir thickness range from 0 to 25 m. Signal amplitude decreases as much as 62.5% in the model built at well

15-191-20789 and 74% in the model built at well 15-191-22591 within the thickness range of 0-25 m. The results of the seismic data attribute analysis showed 80% amplitude decrease over the thickness range 6-20 m. The modeling results in chapter 3 reported 74% decrease in amplitude over the thickness range 5-30 m. Instantaneous frequency decreases as much as 33% in the model built at well 15-191-20789 and 45% in the model built at well 15-191-22591 within the thickness range of 0-25 m. The corresponding results of the seismic data attribute analysis (section 5.3.1) showed 25-33% decrease over the range 6-20 m, and modeling of the seismic response of a ramp-transitional velocity function (chapter 3) reported 17% decrease over the 10-20 m.

Regarding the cause of the double reflector from the Mississippian reservoir, the results of the seismic interpretation show its presence in the south-eastern part of the Wellington Field only (Figure 5.3). The arbitrary line shown in Figure 4.13 crosses the area where the double reflector is present. Sonic and pseudo-sonic well logs are overlain on the seismic section at well locations. Wells #15-191-22590 and 15-191-22591 have approximately the same reservoir thickness of 17.5 and 20 m respectively. Even though, the reservoir is thicker at well #15-191-22591, the double reflector is developed at well #15-191-22590 and it is not present at well #15-191-22591. The seismic modeling at well #15-191-22591 shows that the double reflection is developed for the thicknesses greater than 21 m (Figures 4.18, 4.24). The seismic modeling at well #15-191-20789 shows the double reflector at smaller thickness of 17-18 m (Figures 4.17-4.25). The presence of the double reflector at smaller thicknesses in the model built at well 15-191-20789 can be explained by the interference with the thin porous layer right below the reservoir. This thin layer was already mentioned in section 5.1 and 5.3.1. There is strong evidence that this thin layer is present only in the south-eastern part of the Wellington Field

(Figure 5.1) and disappears across the fault #1 in the north-western half of the field (Figure5.2). The arbitrary line shown in Figure 4.13 with overlain sonic and pseudo-sonic well logs supports this conclusion. Moreover, the reservoir thickness greater than 20 m is not observed at the Wellington Field. So, the lower reflection of the double reflector is a composite reflection from the base of the Mississippian reservoir and the thin layer below it.

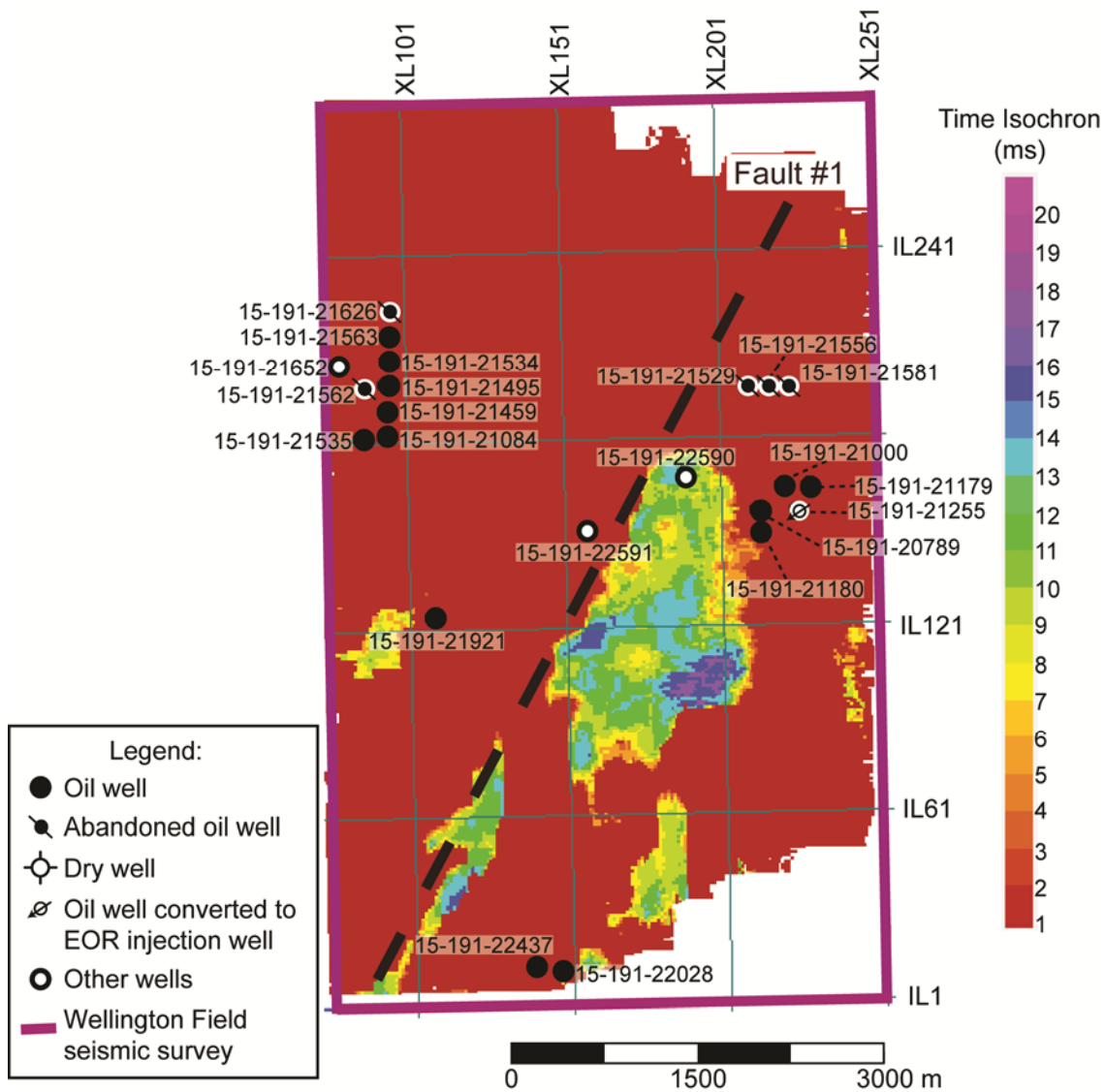


Figure 5.3. Two-way travel time thickness between MissTop and Mbase reflections shown in Figure 4.13. This map shows the areas of the double reflector developed at the top of the Mississippian System.

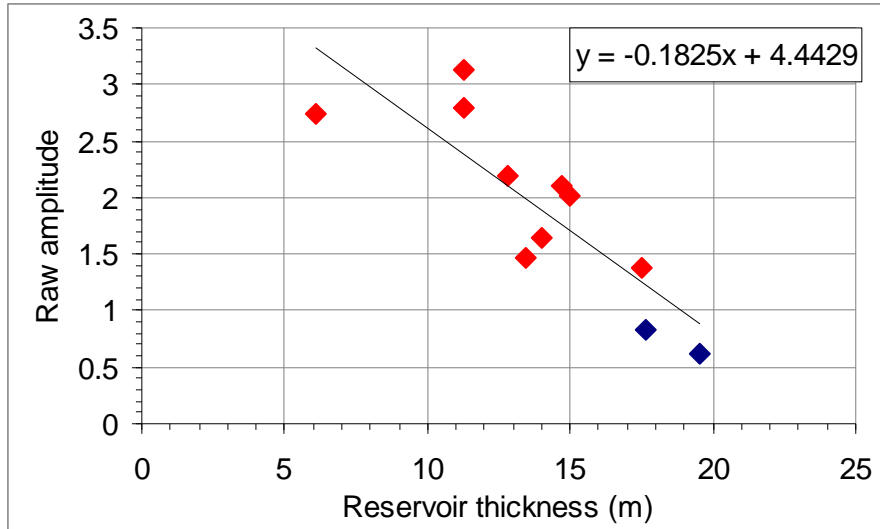


Figure 5.4. Crossplot of raw seismic amplitude of the MissTop horizon versus the reservoir thickness at the wells of group #1. Black line represents a linear regression line with equation shown in the upper right corner. Correlation coefficient $R=0.84$; RMS error of thickness prediction = 2.26 m. Wells with formation porosity logs are shown as red diamonds, wells with both density and neutron porosity logs – as dark blue diamonds.

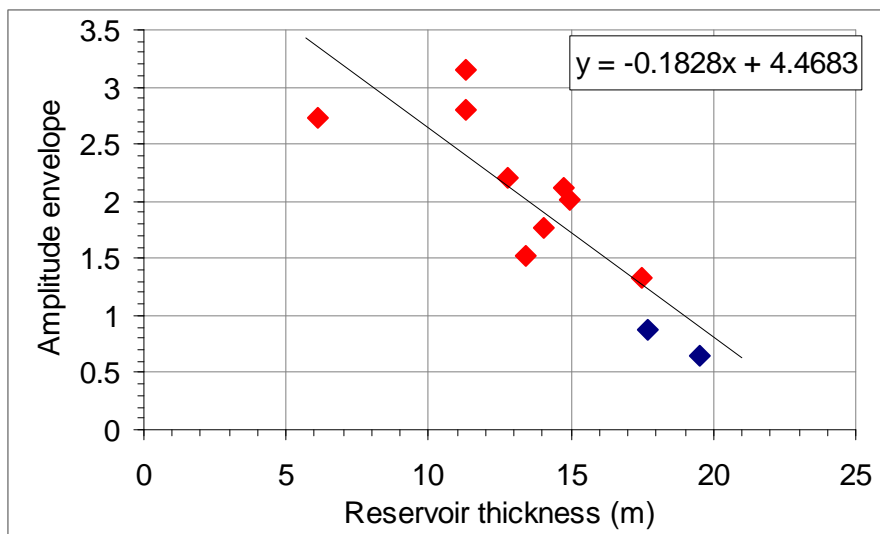


Figure 5.5. Crossplot of amplitude envelope of the MissTop horizon versus the Mississippian reservoir thickness at the wells of group #1. Black line represents a linear regression line with equation shown in the upper right corner. Correlation coefficient $R=0.85$; RMS error of thickness prediction = 2.195 m. Wells with formation porosity logs are shown as red diamonds, wells with both density and neutron porosity logs – as dark blue diamonds.

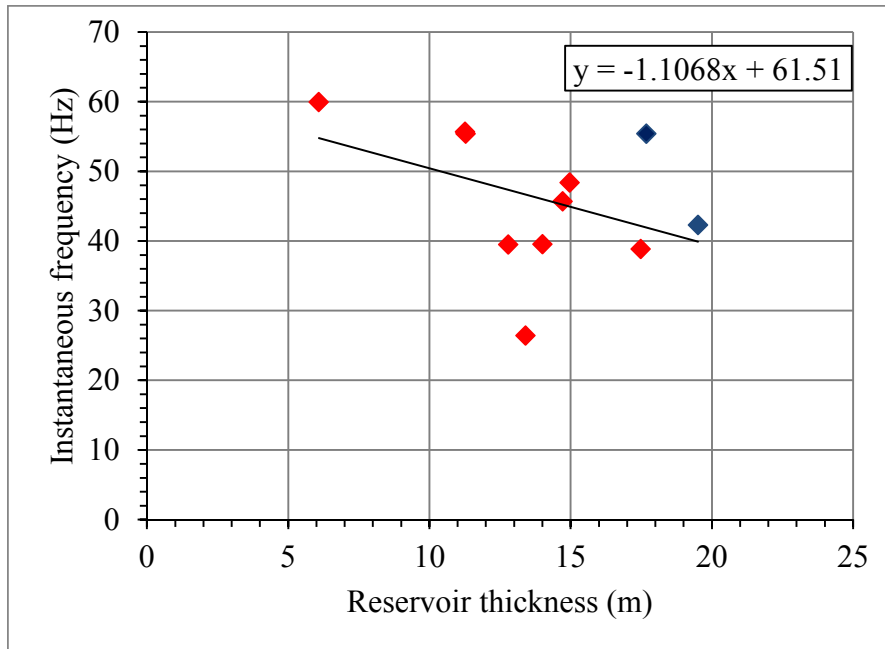


Figure 5.6. Crossplot of RMS average instantaneous frequency within 5 ms window centered at MissTop horizon versus the Mississippian reservoir thickness at the wells of group #1. Black line represents a linear regression line with equation shown in the upper right corner. Correlation coefficient $R=0.41$; RMS error of thickness prediction = 7.87 m. Wells with formation porosity logs are shown as red diamonds, wells with both density and neutron porosity logs – as dark blue diamonds.

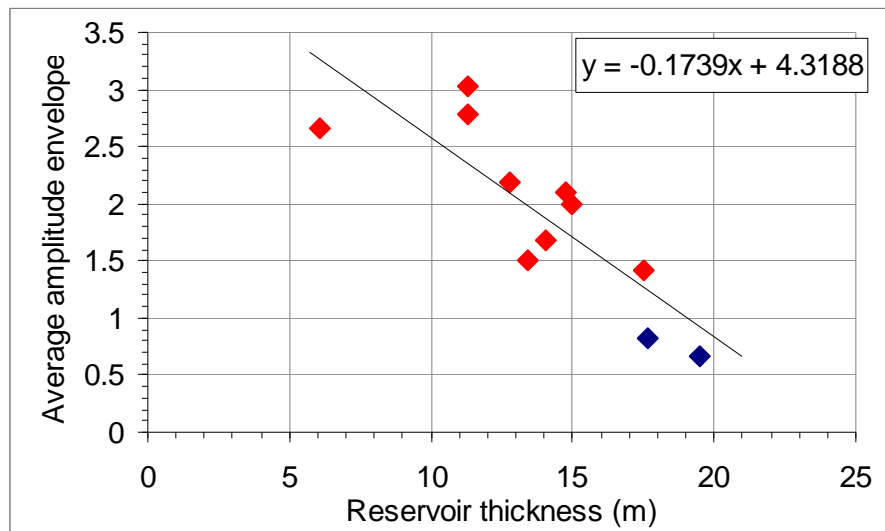


Figure 5.7. Crossplot of amplitude envelope of the MissTop horizon averaged around well locations within 9 closest traces versus the Mississippian reservoir thickness at the wells of group #1. Black line represents a linear regression line with equation shown in the upper right corner. Correlation coefficient $R=0.84$; RMS error of thickness prediction = 2.27 m. Wells with formation porosity logs are shown as red diamonds, wells with both density and neutron porosity logs – as dark blue diamonds.

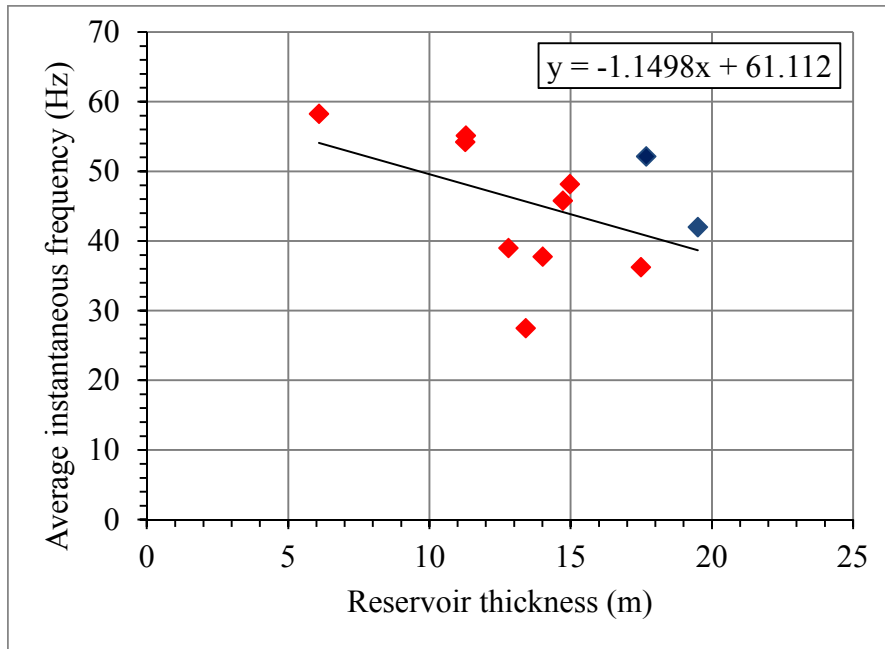


Figure 5.8. Crossplot of instantaneous frequency of the MissTop horizon averaged around well locations within 9 closest traces versus the Mississippian reservoir thickness at the wells of group #1. Black line represents a linear regression line with equation shown in the upper right corner. Correlation coefficient $R=0.45$; RMS error of thickness prediction = 7.07 m. Wells with formation porosity logs are shown as red diamonds, wells with both density and neutron porosity logs – as dark blue diamonds.

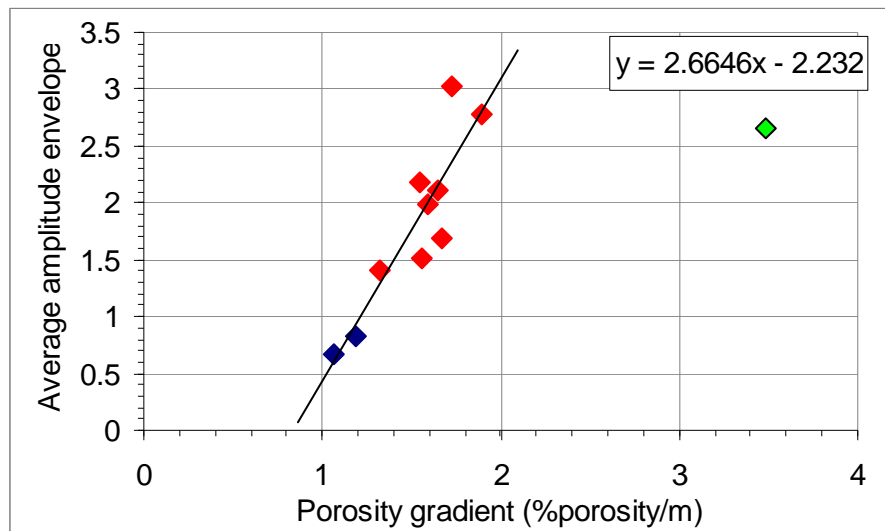


Figure 5.9. Crossplot of amplitude envelope of the MissTop horizon averaged around well locations within 9 closest traces versus the downward porosity gradient (%porosity/m) within the Mississippian reservoir at the wells of group #1. Black line represents a linear regression line with equation shown in the upper right corner. Wells with formation porosity logs are shown as red diamonds, wells with both density and neutron porosity logs – as dark blue diamonds. An outlier is shown as light green diamond and corresponds to well #15-191-21179 with formation porosity log. Correlation coefficient $R=0.89$; RMS prediction error=0.12%/m.

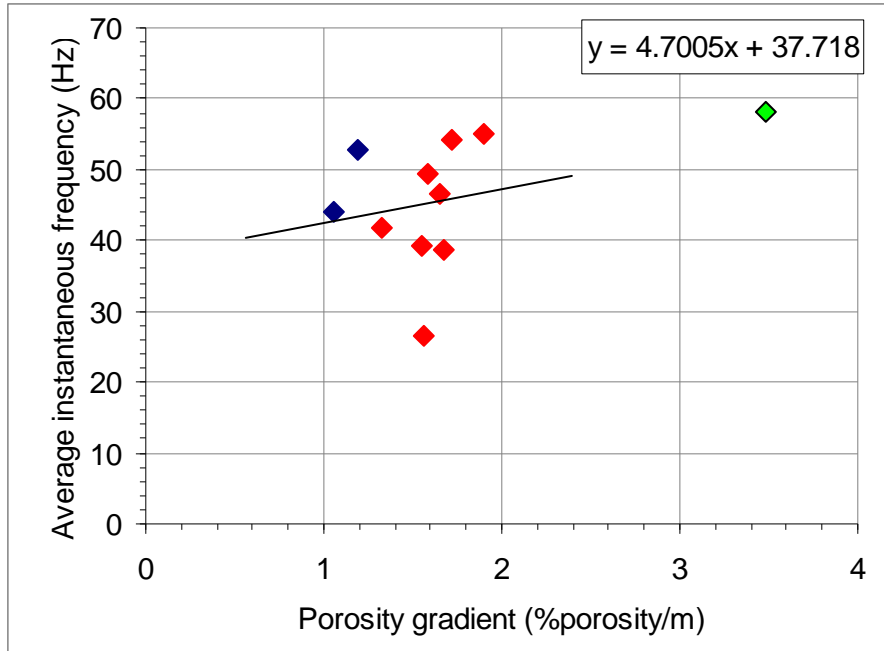


Figure 5.10. Crossplot of instantaneous frequency of the MissTop horizon averaged around well locations within 9 closest traces versus the downward porosity gradient (%porosity/m) within the Mississippian reservoir at the wells of group #1. Black line represents a linear regression line with equation shown in the upper right corner. Wells with formation porosity logs are shown as red diamonds, wells with both density and neutron porosity logs – as dark blue diamonds. An outlier is shown as light green diamond and corresponds to well #15-191-21179 with formation porosity log. Correlation coefficient $R=0.14$.

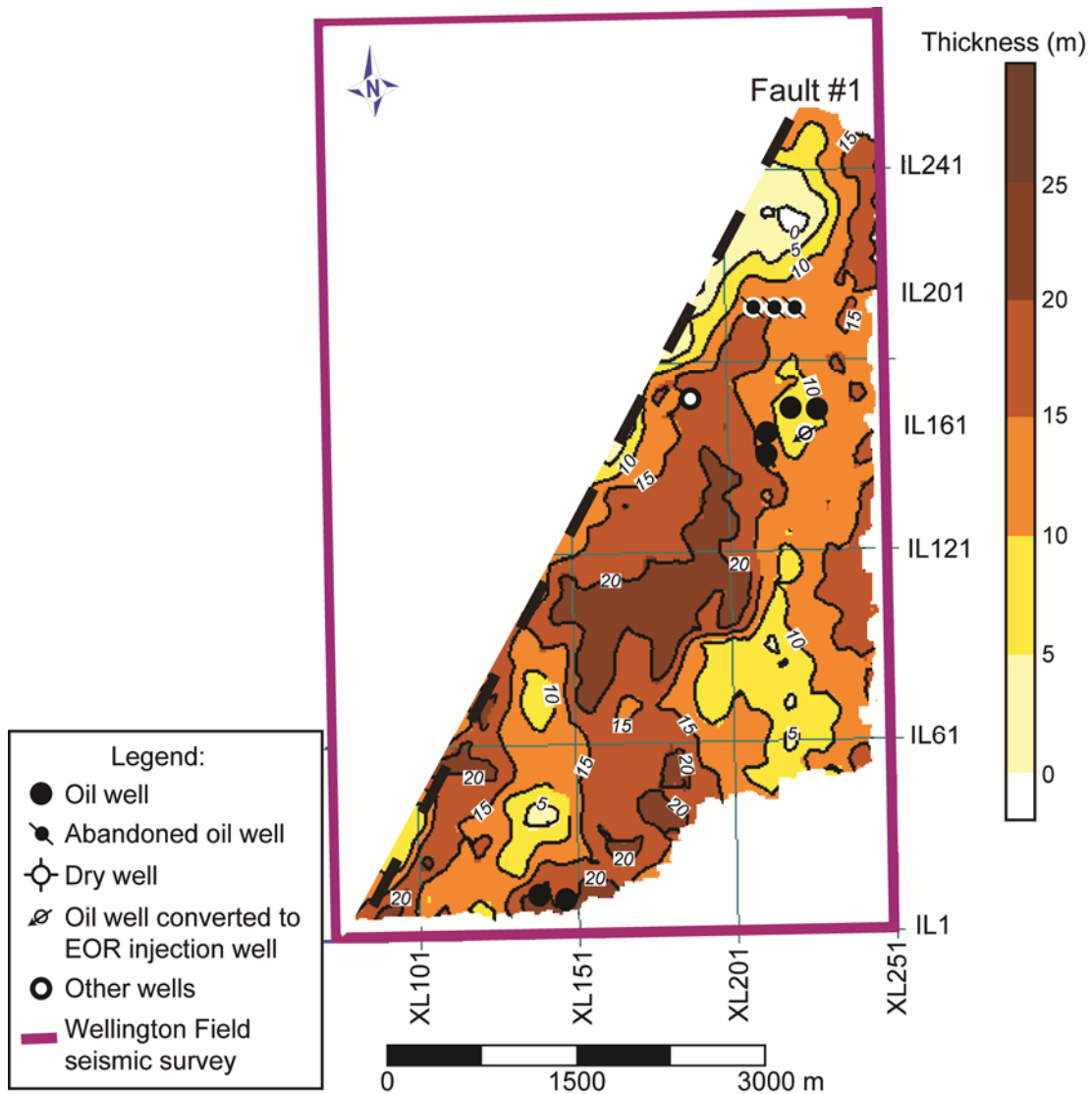


Figure 5.11. Map of the thickness of the Mississippian reservoir at the Wellington Field predicted from the amplitude envelope. Note, that the thickness values are valid only for the south-eastern part of the Wellington Field because the relationship between amplitude envelope and reservoir thickness was derived using the wells of the group #1 (locations of these wells are shown in this map).

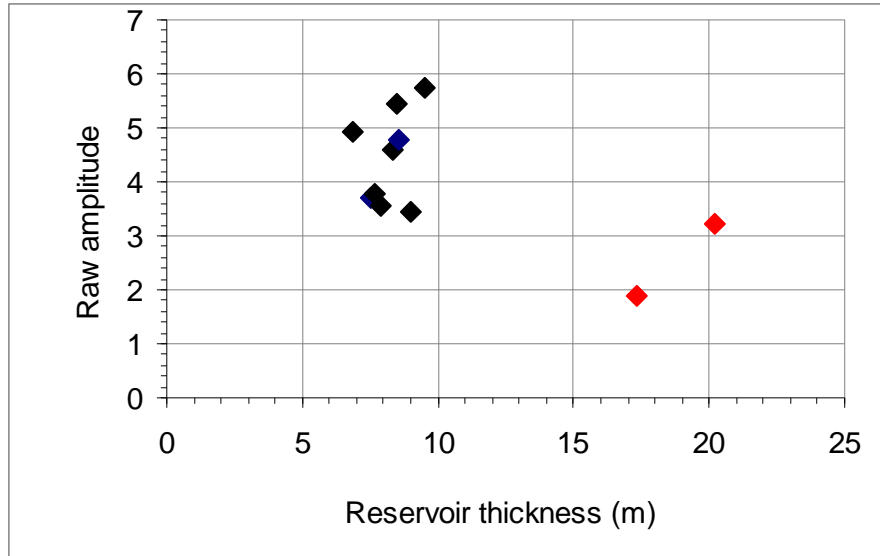


Figure 5.12. Crossplot of raw seismic amplitude of the MissTop horizon versus the reservoir thickness at the wells of group #2. Wells with formation porosity logs are shown as red diamonds, wells with both density and neutron porosity logs – as dark blue diamonds, wells with density logs only – as black diamonds.

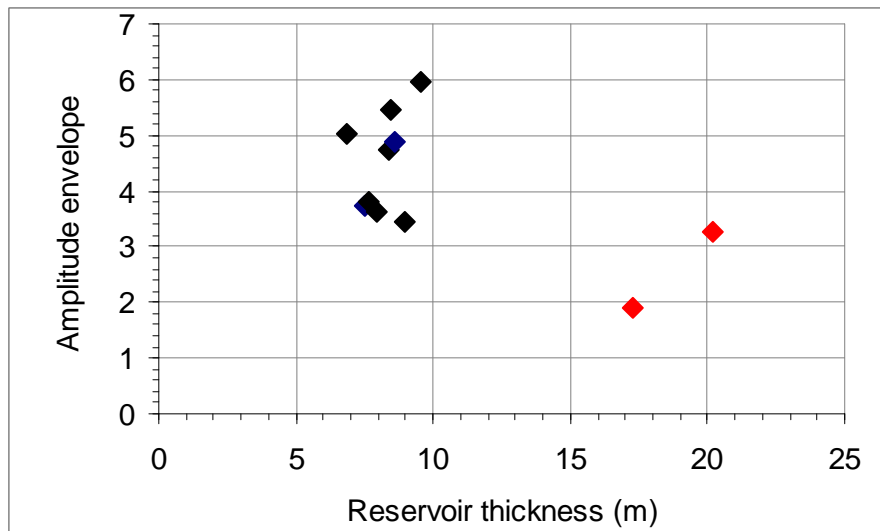


Figure 5.13. Crossplot of amplitude envelope of the MissTop horizon versus the reservoir thickness at the wells of group #2. Wells with formation porosity logs are shown as red diamonds, wells with both density and neutron porosity logs – as dark blue diamonds, wells with density logs only – as black diamonds.

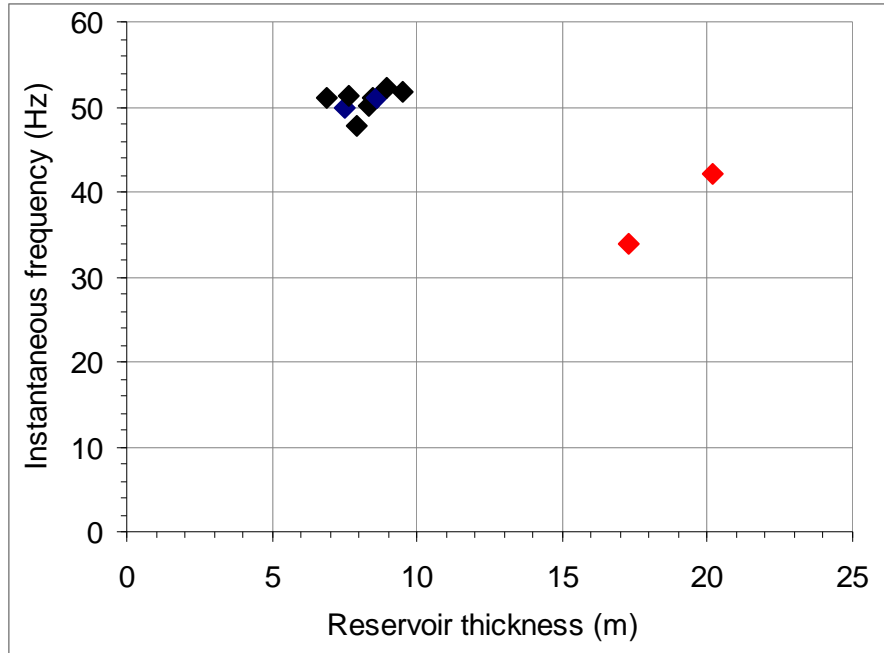


Figure 5.14. Crossplot of instantaneous frequency of the MissTop horizon versus the reservoir thickness at the wells of group #2. Wells with formation porosity logs are shown as red diamonds, wells with both density and neutron porosity logs – as dark blue diamonds, wells with density logs only – as black diamonds.

5.4: Post-stack Model-based Inversion

Model-based acoustic impedance inversion of the PSTM seismic data was conducted in order to derive the acoustic impedance model of the subsurface at the Wellington Field as described in section 4.4. The result of the model-based inversion was analyzed for the entire geological section as well as the Mississippian reservoir at well locations. Additionally, model-based inversion of the synthetic wedge model built at well #15-19-20789 was performed in order to estimate the resolving power of this inversion approach in case of the transitional acoustic impedance boundary.

5.4.1: Model-based Inversion of PSTM Seismic Data

Model-based inversion of the PSTM seismic data provided the acoustic impedance model of the subsurface at the Wellington Field. The inversion results are evaluated by comparing actual and estimated impedances as well as actual and modeled seismic traces at well locations.

The inversion result was evaluated at two well locations, #15-191-20789 and 15-191-22591, within the interval between the tops of the Lecompton Limestone and the Arbuckle Group (Figures 4.30). The inverted impedance curves (red) show a good agreement with the original impedance log curves (blue) within the analysis window identified with yellow horizontal lines. The synthetic seismic traces (red) generated by the convolution of the inverted impedance with the seismic wavelet show high correlation (greater than 0.90) with the actual seismic traces (black) at the well locations. The crossplot of inverted and actual impedance values at both wells supports the good agreement visually observed in Figure 4.30 (Figure 4.31). All the points on the crossplot align along the line of perfect correlation with a scatter characterized by low RMS error of 1286 (m/s)*(g/cc). Supported by the good agreement between inverted and actual impedance data at the two well locations, the model-based inversion was

applied to the seismic data in order to calculate the acoustic impedance model of the subsurface (Figures 4.32-4.33). The inverted impedance depicts the main geologic units, such as pinching out of the Lecompton Limestone, low-impedance Pennsylvanian shales (above the MissTop horizon) and high-impedance carbonates of Kansas-City Group, Mississippian System and Arbuckle Group. Moreover, the inverted impedance sections provide the information on lateral variability of acoustic impedance within the stratigraphic units. This lateral and vertical variability in acoustic impedance values might relate to stratigraphic changes and porosity distribution.

As reported in section 2.3 and shown in Figure 2.4, a gradational downward porosity decrease within the Mississippian reservoir causes the corresponding increase in acoustic impedance. Therefore, the Mississippian reservoir corresponds to the transitional impedance boundary. The inversion result was analyzed within the Mississippian reservoir at twelve well locations to assess if the impedance values were recovered within the transitional boundary by the model-based inversion approach available in Hampson-Russell software. Wells used in the analysis are shown in Figure 4.1: two of these wells, #15-191-20789 and 15-191-22591, have original sonic logs, and the other ten wells have pseudo-sonic logs calculated as described in section 4.2. All wells have original density logs. In general, the inverted impedance curves (red) show a good agreement with the original impedance logs (blue) for the Mississippian reservoir within the analysis window shown with yellow horizontal lines (Figure 4.34). The good agreement is supported by the crossplot of the inverted and actual impedance values at these well locations (Figure 4.35). However, Figure 4.35 reveals several points shifted from the line of perfect correlation in the upper right part of the crossplot. These outliers represent underestimation of high impedances near the reservoir base as visually evident for wells #15-

191-21556 and 15-191-22590 in Figure 4.34. Overall, the impedance inversion result demonstrates a good agreement with the original impedance logs at the well locations. However, two shortcomings can be pointed out for the use of the inverted impedance for porosity prediction within the Mississippian reservoir characterized by a gradational downward porosity reduction and corresponding increase in acoustic impedance. First, the Pennsylvanian shales overlying the Mississippian reservoir are characterized by impedance values generally equal to the impedances at the top of the Mississippian reservoir. The inverted impedance within the Pennsylvanian shales is valid and conformable with well log information, but the absence of an impedance contrast at the reservoir top results in the difficulty of defining the reservoir top using inverted impedance data. Second, the inverted impedance result failed to recover some of the high impedance values near the reservoir base. Therefore, the difficulty of picking the reservoir base may also occur using the inverted impedance data. These shortcomings of impedance inversion and their influence on the porosity prediction result are further discussed in section 5.5.

5.4.2: Model-based Inversion of the Synthetic Wedge Models

The ability of the model-based inversion available in the Hampson-Russell STRATA software to recover impedance values within the Mississippian reservoir characterized by a transitional impedance boundary was tested using the synthetic wedge models built at wells #15-191-20789 and 15-191-22591. The inversion result was analyzed at each trace location of the synthetic seismic section. Figures 4.36 and 4.37 demonstrate the comparison of the inverted impedance traces (red) and the original impedance logs (blue) for the wedge thicknesses of 0-5, 10, 15-20, 25, 30, 35, 40, 45 and 50 m for the inverted impedance section built at the well #15-191-20789. Wedge thickness of 0 m represents a step-velocity function and a sharp acoustic impedance boundary. Visual comparison of the inverted and original impedance curves for the

wedge thickness of 0 m shows that model-based inversion provides a transitional impedance boundary in case of the sharp impedance contrast (Figure 4.36). As the wedge thickness increases, a sharp impedance boundary changes to the transitional impedance boundary. However, the impedance boundary remains sharp in time domain at the seismic sampling interval of 2 ms within the thickness range 0-5 m as seen from the original impedance curves (blue). The model-based inversion result shows a transitional impedance boundary within that range and, therefore, fails to recover sharp impedance boundaries and provides their smoothed versions instead. Analysis at the reservoir thicknesses of 10, 15-20, 25 and 30 m demonstrates that the agreement between the inverted and original impedance curves improves as the reservoir thickness increases (Figures 4.36-4.37). Further increase of the wedge thickness results in the increasing overestimation of impedance values by model-based inversion as evident by comparison of the inverted and original impedance curves for the thicknesses of 30, 35, 40 and 50 m (Figure 4.37). Figure 4.38 shows the crossplot of the RMS inversion error calculated within the reservoir interval versus the wedge thickness at the well #15-191-20789. This crossplot supports the visual comparison of the inverted and original impedance curves in Figures 4.36 and 4.37. The RMS error is high when the model-based inversion fails to recover the sharp impedance contrast and provides its smoothed version within the thickness range 0-5 m. As the wedge thickness increases, the RMS inversion error decreases within the thickness range 0-33 m and then increases within the thickness range 34-50 m. The RMS inversion curve exhibits a broad minimum within the approximate thickness range of 10-35 m ($1/8\lambda$ - $7/16\lambda$).

Figures 5.15 and 5.16 show inverted impedance sections of the wedge models built at the wells #15-191-20789 and 15-191-22591 respectively. Both inverted impedance sections show that the model-based inversion approach fails to recover a step-velocity function and ramp

thicknesses less than 10 m. Inverted acoustic impedance traces exhibit a good agreement with the acoustic impedance logs within the thickness range of 10-35 m ($1/8\lambda$ - $7/16\lambda$). Further increase in ramp thickness results in overestimation of impedance values by model-based inversion.

The test of the model-based inversion using the synthetic wedge model built at wells #15-191-20789 and 15-191-22591 demonstrates that this inversion approach provides reliable impedance information within the transitional impedance boundary for the approximate thickness range 10-35 m.

5.5: Porosity prediction

The multiattribute regression analysis for porosity prediction using inverted impedance and the attributes listed in Table 4.3 showed that inverted impedance alone provides the best porosity estimate (section 4.5.1). The transform for porosity prediction from inverted impedance was derived using the linear regression analysis within the Mississippian reservoir and was applied to the inverted impedance data. Since the transform was derived using the data within the Mississippian chert reservoir, porosity values in the predicted porosity model are valid within the reservoir only and do not provide any meaningful information outside the reservoir.

The quality of porosity prediction was analyzed at the well locations by visual comparison of original and predicted formation porosity logs shown in Figure 4.43 and calculation of RMS prediction and validation errors at all wells. The predicted formation porosity logs (red curves) show a good agreement with the original formation porosity logs within the Mississippian reservoir (analysis window is shown with blue horizontal lines). The RMS prediction and validation errors are shown in Figure 5.17 for each well. The cross-validation technique imitated the process of drilling a new well, and the RMS validation errors represent the corresponding errors at each well. The average RMS validation for all wells is 3.8% with the

maximum RMS validation error of 5.6% at well #15-191-21180. The average RMS prediction error is 3.5% with the maximum RMS prediction error of 5.4% at well #15-191-21180. The resultant porosity model provides reliable information of porosity distribution within the Mississippian reservoir as supported by the good agreement between predicted porosity and formation porosity logs at the well locations with low RMS validation and prediction errors. However, the shortcomings of the model-based inversion described in section 5.4.1 result in the difficulties of picking the reservoir top and base in the resultant porosity model. The Pennsylvanian shales overlying the Mississippian reservoir are characterized by low impedance values, and the linear transform of impedance values to porosity result in high porosities, 20-30%, within the Pennsylvanian shales. These high porosities within the Pennsylvanian shales in the resultant porosity model are erroneous because the applied transform was derived using the data within the Mississippian reservoir only. However, the high porosities in the Pennsylvanian shales complicate picking the reservoir top in the porosity model. Another shortcoming of the model-based inversion, the underestimation of the impedance values near the reservoir top, complicates the picking of the reservoir base in the resultant porosity model. This shortcoming is evident at several well locations, #15-191-20789, 15-191-21556 and 15-191-22590, in Figure 4.43.

Figures 4.44 and 4.45 show the predicted porosity sections with the overlain formation porosity log at well #15-191-22591. The reservoir top and base, MissPorTop and MissLowPor, are shown with red horizontal lines on the log curve at the well location. Predicted porosity exhibit good agreement with the formation porosity log within the reservoir interval at the well location and show the porosity distribution within the Mississippian reservoir along the MissTop horizon. Predicted porosities are valid within the reservoir interval only (along the MissTop seismic horizon) and do not contain any valid information elsewhere. Delineating the

Mississippian reservoir in the resultant porosity model throughout the Wellington Field present a difficult task due to the shortcomings of the approach discussed earlier in the section.

Several observations can be pointed out by the visual inspection of the predicted porosity sections in Figures 4.44 and 4.45:

1. The resultant porosity model shows high porosities in the Pennsylvanian shales overlying the Mississippian reservoir which do not bear any meaningful information. However, locally these values are within the range 25-30%, as around well #15-191-22591, while porosities at the top of the Mississippian reservoir are generally 25%. Therefore, picking the reservoir top in these areas may be feasible.
2. It is possible to pick the reservoir base where the resultant porosity model clearly shows porosities of 4-6% below the Mississippian reservoir. Such areas are approximately located between 135 and 187 traces of the inline #152 and between 117 and 282 traces of crossline #158.
3. The thin layer present below the Mississippian reservoir in the south-eastern part of the Wellington Field and being one of the factors causing the locally developed double reflector (discussed in sections 5.1, 5.3.1 and 5.3.2) is possibly the factor responsible for one of the shortcomings described above. A double reflection associated with the Mississippian reservoir is observed in the following areas: 175-209 traces of the inline #152 (Figure 4.11) and 79-124 traces of the crossline #158 (Figure 4.12). The difficulty with picking the reservoir base in the resultant porosity model is evident in these areas also. Moreover, this difficulty is evident further to the east along the inline #152 and to the south along the inline #158 even though the double reflection merges in these areas into a single one. I think that the thin layer below the reservoir is present throughout the south-eastern part of the Wellington Field, and it becomes evident on seismic data when the reservoir thickens to 17-20 m producing a double reflector. The model-

based inversion was not able to recover this thin layer, ≈ 4 m thick, while this layer influenced the inversion result, and, therefore, affected the resultant porosity model.

4. The north part of the crossline #158 (207-282 trace range, Figure 4.45) is characterized by faster downward porosity decrease within the reservoir interval. This observation indicates the thinning of the transitional impedance boundary to the north. As described in section 5.4.2, the sharp impedance boundary is smoothed to the transitional boundary for the reservoir thickness below 5 m. Therefore, the observed thinning of the transitional boundary in the north part of the crossline #158 might, in fact, indicate the reservoir absence.

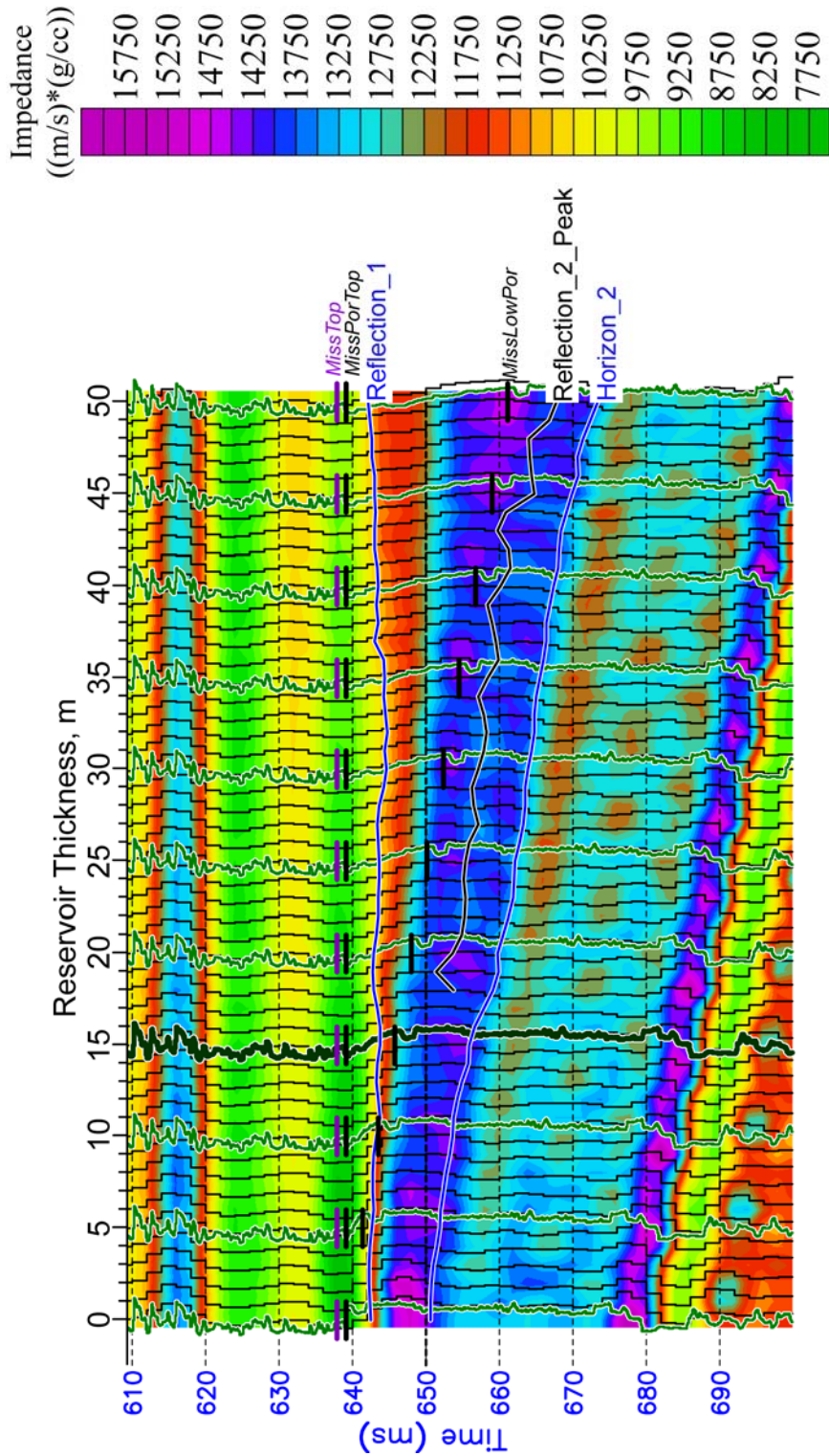


Figure 5.15. Model-based inverted impedance section of the synthetic seismic section built at well #15-191-20789 (shown in Figure 4.17). Black traces represent inverted acoustic impedance curves; acoustic impedance logs are shown for every 5th trace as light green curves; original acoustic impedance log at well #15-191-20789 is shown as dark green curve.

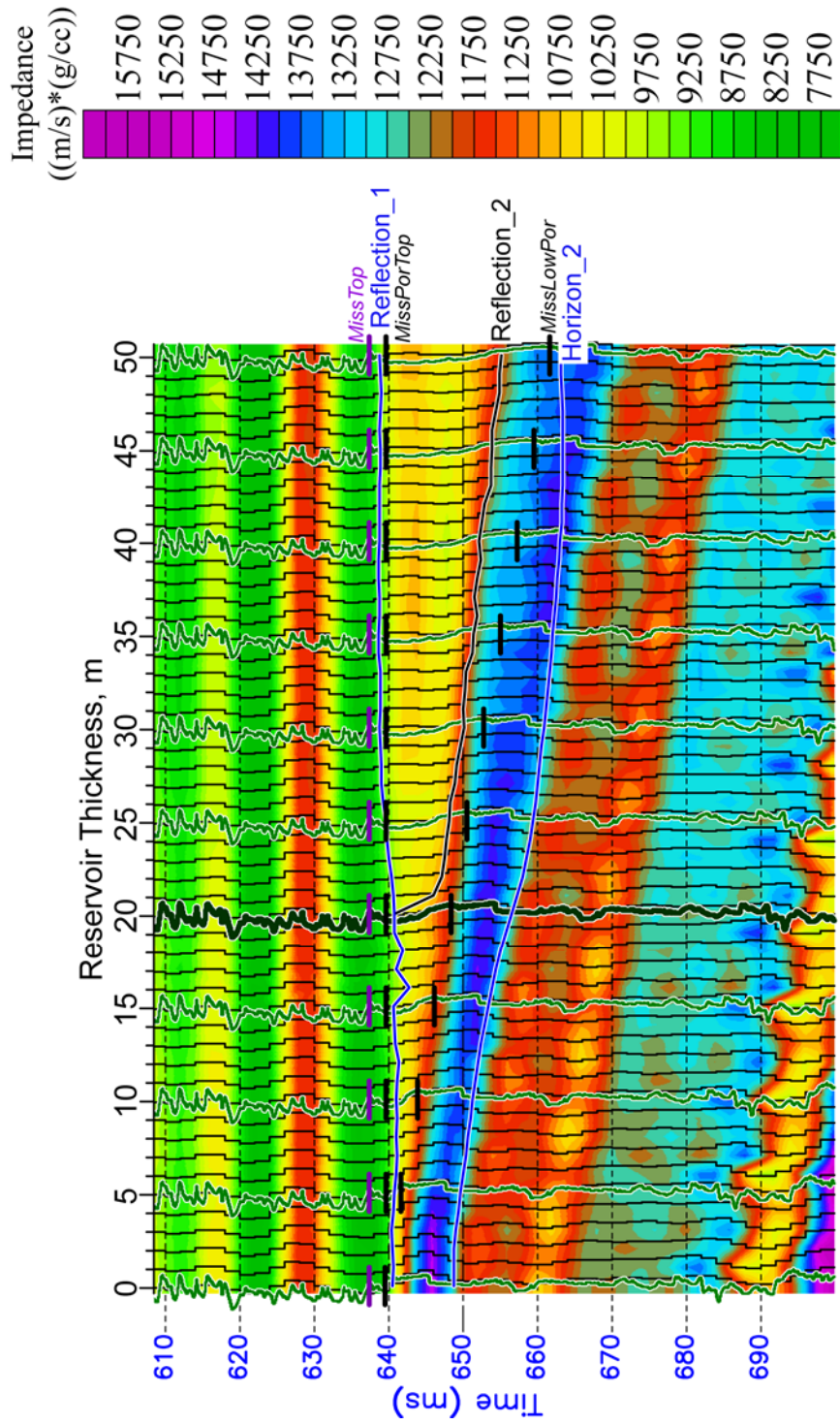


Figure 5.16. Model-based inverted impedance section of the synthetic seismic section built at well #15-191-22591 (shown in Figure 4.18). Black traces represent inverted acoustic impedance curves; acoustic impedance logs are shown for every 5th trace as light green curves; original acoustic impedance log at well #15-191-22591 is shown as dark green curve.

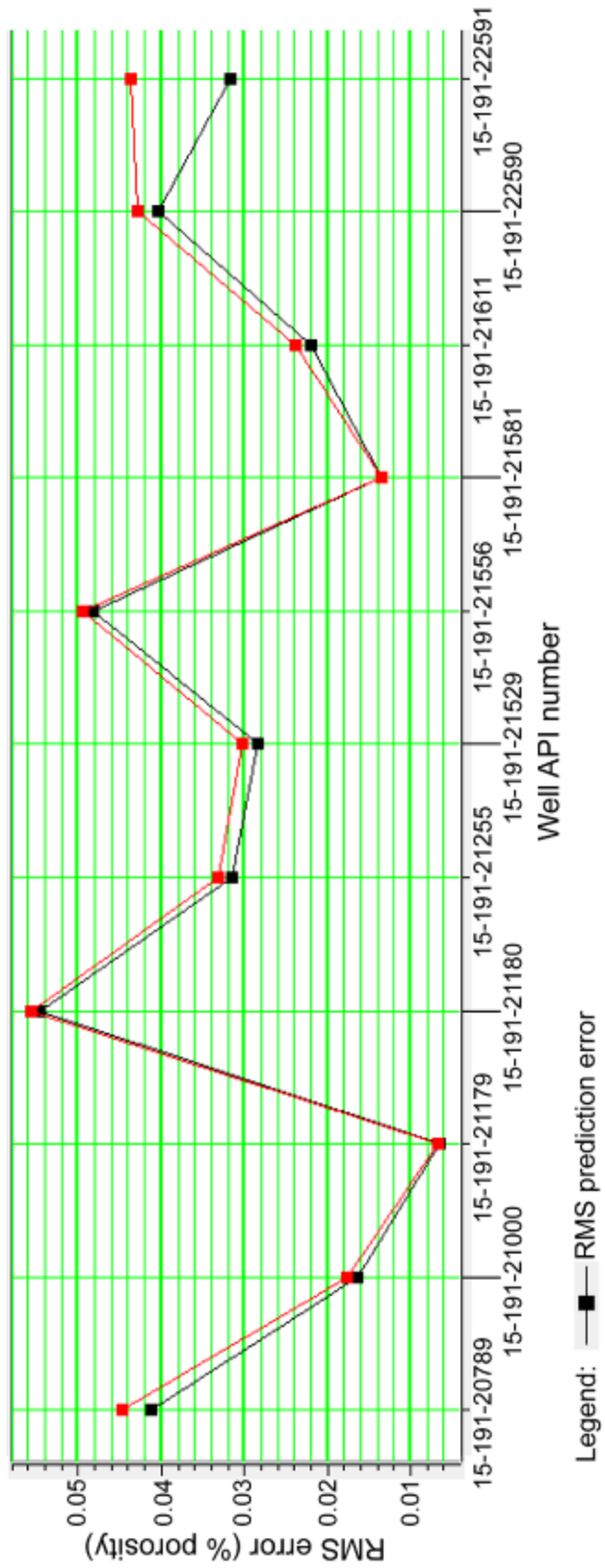


Figure 5.17. Average RMS prediction and validation errors versus well API number for the porosity prediction from the acoustic impedance described in section 4.5.2.

CHAPTER 6: CONCLUSIONS

In this study I employed well logs and 3D PSTM seismic data to characterize the Mississippian chert reservoirs at the Wellington Field. The following conclusions can be drawn from the results presented in the thesis:

1. The Mississippian chert reservoir exhibits high variability in porosity distribution throughout the Wellington Field. The variability is observed on both well-log and seismic data. Fault #1 divides the field diagonally into two parts from the southwestern corner to the northeastern corner of the field.
2. The Mississippian reservoir in the southeastern part of the field is characterized by a gradational downward porosity decrease according to the porosity logs of group #1. This downward porosity reduction within the reservoir interval causes the corresponding increase in P-wave velocity, a ramp-transition velocity function. Seismic response of the Mississippian reservoir exhibits lower amplitude and frequency content in this part of the field with a locally developed double reflection.
3. Raw seismic amplitude and amplitude envelope attributes taken at the peak of the Mississippian reflection can be used to predict the thickness of the reservoirs characterized by a gradational downward porosity decrease. The thickness of the Mississippian reservoir was predicted in the southeastern part of the Wellington Field with low RMS prediction error (≈ 2.2 m).
4. Seismic wedge modeling using both synthetic and original sonic logs is a useful tool aiding seismic interpretation. The modeling of the Mississippian reservoir using synthetic velocity model helped to understand the seismic response of a ramp-transition velocity function in an ideal case. The modeling of the reservoir using original sonic logs at the Wellington Field

demonstrated a site-specific seismic response of the reservoir characterized by a gradational downward porosity decrease. Seismic modeling showed that the amplitude attributes provide reliable prediction result within the thickness range 5-25 m, underestimate thicknesses exceeding 25 m and do not recover thicknesses below 5 m. This 5-25 m thickness range corresponds to $1/16\lambda$ - $5/16\lambda$ range in terms of wavelength.

5. The site-specific seismic modeling also revealed that the locally developed double reflection from the Mississippian reservoir is caused by a thin slightly porous layer, few meters below the reservoir base, which is present in the southeastern part of the field and disappears across the fault #1. A double reflector in the southeastern part of the Wellington Field is an indicator of a thicker reservoir. However, in the northwestern part of the field the absence of a double reflector does not imply that the reservoir is thin as the cause of this double reflector is a thin layer below the reservoir absent in this part of the field.

6. Instantaneous frequency is a less reliable attribute for prediction of the reservoir thickness in the southeastern part of the Wellington Field. However, frequency attributes should be considered for similar reservoirs characterized by a gradational downward porosity reduction.

7. The Mississippian chert reservoir in the northwestern part of the Wellington Field is characterized by high variability of porosity distribution according to the porosity logs of the group #2 and generally thin reservoir (6-8 m). Some wells in this part of the field show relatively uniform vertical porosity distribution, in other wells downward porosity reduction is present. Overall the seismic response of the Mississippian reservoir in the northwestern part of the Wellington seismic survey demonstrates higher amplitude and frequency content than the southeastern part. However, neither amplitude nor frequency can be used for prediction of the reservoir thickness in this part of the field.

8. Model-based inversion of the synthetic seismic section built at well #15-191-20789 allowed the assessment of the resolution provided by the inversion approach available in Hampson-Russell STRATA software in case of the gradational impedance increase within the Mississippian reservoir. The model-based inversion approach recovers reliable impedance information within the reservoir thickness range 10-35 m, which corresponds to $1/8\lambda$ - $7/16\lambda$ in terms of wavelength.

9. The inverted impedance is shown to be the best seismic attribute for porosity prediction in the Mississippian chert reservoir at the Wellington Field. The resultant porosity model is valid within the Mississippian reservoir only. The porosity model has the same resolution as the acoustic impedance inversion. Therefore, it provides reliable porosity values for the reservoir thicknesses 10-35 m, or $1/8\lambda$ - $7/16\lambda$ in terms of wavelength.

10. The resultant porosity model provides reliable porosity information within the Mississippian reservoir at the Wellington Field. However, the reservoir top and base are difficult to pick in some areas. The difficulties of picking the reservoir base occur mostly in the southeastern part of the field where the thin layer below the reservoir is present and produces the double reflection. In this part of the field the thickness map predicted from the amplitude envelope can be used to assist the reservoir delineation in the porosity model.

11. The resultant porosity model shows the thinning of the interval with gradational downward porosity decrease in the north-western part of the Wellington Field. This possibly indicates thinning of the reservoir below the resolution of the model-based inversion (10 m or $1/8\lambda$).

In this study I evaluated the seismic response of a ramp-transition velocity function as a reservoir characterization tool using stacked seismic data. Particularly, I demonstrate the characteristic seismic amplitude decrease with increasing thickness of the Mississippian chert

reservoir characterized by a ramp-transition velocity function using the PSTM seismic data at the Wellington Field. This phenomenon is well established in theory and has been recognized in exploration geophysics for more than 50 years. However, it has been poorly investigated using real seismic data. The approximate applicability of the method for the reservoir thickness prediction is within the thickness range of $1/16\lambda$ - $5/16\lambda$. When the reservoir thickness is below $1/16\lambda$, the reflection amplitude approaches the amplitude corresponding to a step velocity function, and the reservoir thickness is not resolvable from the amplitude data. As the reservoir thickness exceeds the $5/16\lambda$ thickness the slope of the amplitude decline decreases. The resolution of the model-based inversion, also poorly defined in the literature and commonly referred as enhancing the resolution of seismic data, was evaluated in case of the gradational impedance increase within the reservoir interval. The seismic wedge modeling using the original sonic log at well #15-191-20789 quantified the resolution limits of the model-based impedance inversion as $1/8\lambda$ - $7/16\lambda$ in this case. Below the $1/8\lambda$ thickness the model-based approach provides approximately the same result and fails to recover a sharp impedance contrast providing its smoothed version.

In addition to reservoir property prediction, the seismic response of a ramp-transitional velocity function related to downward porosity reduction might be useful in understanding depositional and diagenetic histories of such reservoirs. For example, the resultant porosity model demonstrates thinning or the interval characterized by a gradational porosity decrease in the north-western part of the Wellington Field. This might indicate changes in the depositional and/or diagenetic history.

I believe that this research will benefit the characterization of reservoirs with similar reservoir architecture. The results of this study are applicable not only to the chert reservoirs, but

also to clastic and carbonate reservoirs as downward porosity reduction might be also found in these reservoirs. Few examples of the reservoirs characterized by a downward porosity reduction are the burrowed chert reservoir at the Dollarhide Field, west Texas (Montgomery, 1998; Saller et al., 2001) and carbonate reservoir in the Sirt Basin, Libya (Swei and Tucker, 2012).

As only a limited number of post-stack seismic attribute was analyzed, the addition of other post- or pre-stack seismic attributes might improve the thickness and porosity predictions. Further investigation of the seismic response of a ramp-transition velocity function within the Mississippian reservoir at the Wellington Field can be done using the AVO, or AVA, analysis, similar to studies done by Gomez and Ravazzoli (2012) and Sloan et al. (2007). Spectral decomposition of seismic data is potentially another useful characterization tool in case of the reservoir with a ramp-transitional velocity function as shown by Liner and Bondman (2010).

REFERENCES

- Berryman, L. H., P. L. Goupillaud, and K. H. Waters, 1958, Reflections from multiple transition layers. Part I — Theoretical results: *Geophysics*, v. 23, no. 2, p. 223-243.
- Cansler, J. R., 2000, Paleogeomorphology of the sub-Pennsylvanian unconformity on the Arbuckle Group (Cambrian–Lower Ordovician): Master’s thesis, University of Kansas, Lawrence, 123 p.
- Cooke, D. A., and W. A. Schneider, 1983, Generalized linear inversion of reflection seismic data: *Geophysics*, v. 48, no. 6, p. 665-676.
- Costain, J. K., and C. Çoruh, 2004, Basic theory of exploration seismology [Handbook of geophysical exploration. Seismic Exploration. Volume 1]: Amsterdam, Elsevier, 571p.
- Elebiju, O. O., S. Matson, G. R., Keller, and K. J. Marfurt, 2011, Integrated geophysical studies of the basement structures, the Mississippi chert, and the Arbuckle Group of Osage County region, Oklahoma: *AAPG Bulletin*, v. 95, no. 3, p. 371-393.
- Franseen, E. K. 2006, Mississippian (Osagean) Shallow-water, mid-latitude siliceous sponge spicule and heterozoan carbonate facies: An example from Kansas with implications for regional controls and distribution of potential reservoir facies: *Current Research in Earth Sciences Bulletin* 252, part 1.
- Fu, D. T., E. C. Sullivan, and K. J. Marfurt, 2006, Rock-property and seismic-attribute analysis of a chert reservoir in the Devonian Thirty-one Formation, west Texas, U.S.A: *Geophysics*, v. 71, no. 5, p. B151-B158.
- Gupta, R. N., 1966, Reflection of plane elastic waves from transition layers with arbitrary variation of velocity and density: *Bulletin of the Seismological Society of America*, v. 56, no. 3, p. 633–642.
- Gomez, J. L., and C. L. Ravazzoli, 2012, Reflection characteristics of linear carbon dioxide transition layers: *Geophysics*, v. 77, no. 3, p. D75-D83.
- Hampson, D., and M. Galbraith, 1981, Wavelet extraction by sonic log correlation: *Canadian Journal of Exploration Geophysics*, v. 17, no. 1, p. 24-42.
- Hampson, D. P., J. S. Schuelke, and J. A. Quirein, 2001, Use of multiattribute transforms to predict log properties from seismic data: *Geophysics*, v. 66, no. 1, p. 220-236.
- Hart, B., and M.-A. Chen, 2004, Understanding seismic attributes through forward modeling: *The Leading Edge*, v. 23, no. 9, p. 834-841.
- Kansas Geological Survey website, 2012, <<http://www.kgs.ku.edu>> Accessed October, 2012.
- Lancaster, S., and D. Whitcombe, 2000, Fast-track ‘coloured’ inversion: *Society of Exploration Geophysicists Expanded Abstracts*, v. 19, p. 1572-1575.

- Lindseth, R. O., 1979, Synthetic sonic logs – a process for stratigraphic interpretation: *Geophysics*, v. 44, no. 1, p. 3-26.
- Liner, C. L., and B. G. Bodmann, 2010, The Wolf ramp: reflection characteristics of a transition layer: *Geophysics*, v. 75, no. 5, p. A31-A35.
- Mazzullo, S. J., B. W. Wilhite, and I. W. Woolsey, 2009, Petroleum reservoirs within a spiculite-dominated depositional sequence: Cowley Formation (Mississippian: Lower Carboniferous), south-central Kansas: *AAPG Bulletin*, v. 93, no.12, p.1649-1689.
- Montgomery, S. L., 1998, Thirtyone formation, Permian Basin, Texas: structural and lithologic heterogeneity in a lower Devonian chert reservoir: *AAPG Bulletin*, v. 82, no. 1, p. 1-24.
- Montgomery, S. L., J. C. Mullarkey, M. W. Longman, W. M. Colleary, and J. P. Rogers, 1998, Mississippian —chatl reservoirs, south Kansas-Low-resistivity pay in a complex chert reservoir: *AAPG Bulletin*, v. 82, p. 187-205.
- Montgomery, S. L., E. K. Franseen, S. Bhattacharya, P. Gerlach, A. Byrnes, W. B. Guy, and T. R. Carr, 2000, Schaben Field, Kansas: improving performance in a Mississippian shallow-shelf carbonate: *AAPG Bulletin*, v. 84, no. 8, p. 1069-1086
- Nissen, S. E., T. R. Carr, K. J. Marfurt, and E. C. Sullivan, 2009, Using 3-D seismic volumetric curvature attributes to identify fracture trends in a depleted Mississippian carbonate reservoir: implications for assessing candidates for CO₂ sequestration, *in* M. Grobe, J. C. Pashin, and R. L. Dodge, eds., *Carbon dioxide sequestration in geological media—State of the science: AAPG Studies in Geology 59*, p. 297–319.
- Oldenburg, D. W., T. Scheuer, and S. Levy, 1983, Recovery of the acoustic impedance from reflection seismograms: *Geophysics*, v. 48, no. 10, p. 1318-1337.
- Padgett, M. J., and D. C. Nester, 1991, Fracture evaluation of block P-0315, Point Arguello Field, offshore California, using core, outcrop, seismic data and curved space analysis, *in* R. Sneider, W. Massell, R. Mathis, D. Loren, and P. Wichmann, eds., *The integration of geology, geophysics, petrophysics, and petroleum engineering in reservoir delineation, description, and management: AAPG Special Publication 26*, p. 242-268.
- Phan, S., and M. K. Sen, 2010, Porosity estimation from seismic data at Dickman Field, Kansas for carbon sequestration: *Society of Exploration Geophysicists Expanded Abstracts*, v. 29, p. 2299-2303.
- Reblin, M. T., G. C. Chapel, S. L. Roche, and C. Keller, 1991, A 3-D seismic survey over the Dollardhide field, Andrews County, Texas, *in* A. R. Brown, ed., *Interpretation of three-dimensional seismic data*, 3d ed.: *AAPG Memoir 42*, p. 263–270.
- Rogers, J. P., and M. W. Longman, 2001, An introduction to chert reservoirs of North America, 2001, *AAPG Bulletin*, v. 85, no.1, p. 1-5.

- Rogers, S. M., 2001, Deposition and diagenesis of Mississippian chert reservoirs, north-central Oklahoma, AAPG Bulletin, v. 85, no.1, p. 115-129.
- Ruppel, S. C., and S. D. Hovorka, 1995, Controls on reservoir development in Devonian chert: Permian Basin, Texas: AAPG Bulletin, v. 79, no.12, p. 1757-1785.
- Ruppel, S. C., and R. J. Barnaby, 2001, Contrasting styles of reservoir development in proximal and distal chert facies: Devonian Thirtyone Formation, Texas: AAPG Bulletin, v. 85, no.1, p. 7-33.
- Russell, B. H., 1988, Introduction to seismic inversion methods: Society of Exploration Geophysicists Course Note Series, no. 2, Tulsa, SEG, 90 p.
- Russell, B., and D. Hampson, 1991, Comparison of poststack seismic inversion methods: Society of Exploration Geophysicists Expanded Abstracts, v. 10, p. 876-878.
- Saller, A. H., D. V. Horn, J. A. Miller, and B. T. Guy, 1991, Reservoir Geology of Devonian carbonates and cherts – implications for tertiary recovery, Dollarhide Field, Andrews County, Texas: AAPG Bulletin, v. 75, no. 1, p. 86-107.
- Saller, A., B. Ball, S. Robertson, B. McPherson, C. Wene, R. Nims, and J. Gogas, 2001, Reservoir characteristics of Devonian cherts and their control on oil recovery: Dollarhide Field, west Texas: AAPG Bulletin, v. 85, no.1, p. 35-50.
- Sarg, J. F. R., and J. S. Schuelke, 2003, Integrated seismic analysis of carbonate reservoirs: from the framework to the volume attributes: The Leading Edge, v. 22, no. 7, p. 640-645.
- Schuelke, J. S., J. A. Quirein, J. F. Sag, D. A. Altany, and P. E. Hunt, 1997, Reservoir architecture and porosity distribution, Pegasus Field, West Texas – an integrated sequence stratigraphic-seismic attribute study using neural network: Society of Exploration Geophysicists Expanded Abstracts, v. 16, p. 668-671.
- Sengbush, R. L., P. L. Lawrence, and F. J. McDonal, 1961, Interpretation of synthetic seismograms: Geophysics, v. 26, no. 2, p. 138-157.
- Sherwood, J. W. C., 1962, The seismoline, an analog computer of theoretical seismograms: Geophysics, v. 27, no. 1, p. 19-34.
- Sloan, S. D., G. P. Tsoflias, and D. W. Steeples, 2007, Seismic AVO variations related to partial water saturation during a pumping test: Society of Exploration Geophysicists Expanded Abstracts, v. 26, p. 1212-1216.
- Swei, G. H., and M. E. Tucker, 2012, Impact of diagenesis on reservoir quality in ramp carbonates: Gialo formation (Middle Eocene), Sirt Basin, Libya: Journal of Petroleum Geology, v. 35, no. 1, p. 25-48.
- Taner, M. T., F. Koehler, and R. E. Sheriff, 1979, Complex seismic trace analysis: Geophysics, v.44, no. 6, p. 1041-1063.

- Thomasson, M. R., R. W. Kettle, R. M. Lloyd, R. K. McCormack, and J. P. Lindsey, 1989, Seismic detection and interpretation of porosity in Carboniferous age rocks of Kansas and Oklahoma: *Geophysics*, v. 54, no. 11, p. 1371-1383.
- Watney, W. L., W. J. Guy, and A. P. Byrnes, 2001, Characterization of the Mississippian chat in south-central Kansas: *AAPG Bulletin*, v. 85, no.1, p. 85-113.
- Wolf, A., 1937, The reflection of elastic waves from transition layers of variable velocity: *Geophysics*, v. 2, p. 357-363.
- Wuenschel, P. C., 1960, Seismogram synthesis including multiples and transmission coefficients: *Geophysics*, v. 25, no. 1, p. 106-129.
- Young, E. M., 2010, Controls on reservoir character in carbonate-chert strata, Mississippian (Osagean-Meramecian), southeast Kansas: Master's thesis, University of Kansas, Lawrence, 198 p.